ISBN 978-82-326-5226-6 (printed ver.)
ISBN 978-82-326-6771-0 (electronic ver.)
ISSN 1503-8181 (printed ver.)
ISSN 2703-8084 (electronic ver.)

NTNU
Norwegian University of
Science and Technology

Doctoral thesis

Jens Abraham

Doctoral theses at NTNU, 2022:91

NTNU
Norwegian University of
Science and Technology
Thesis for the degree of
Philosophiae Doctor
Faculty of Information Technology
and Electrical Engineering
Department of Electronic Systems

NTNU

Doctoral theses at NTNU, 2022:91

Jens Abraham

Methods for Finite Massive MIMO Analysis

NTNU
Norwegian University of
Science and Technology

Jens Abraham

Methods for Finite Massive MIMO Analysis

Thesis for the degree of Philosophiae Doctor

Trondheim, April 2022

Norwegian University of Science and Technology
Faculty of Information Technology
and Electrical Engineering
Department of Electronic Systems

NTNU
Norwegian University of
Science and Technology

NTNU
Norwegian University of Science and Technology

Thesis for the degree of Philosophiae Doctor

Faculty of Information Technology
and Electrical Engineering
Department of Electronic Systems

ISBN 978-82-326-5226-6 (printed ver.)
ISBN 978-82-326-6771-0 (electronic ver.)
ISSN 1503-8181 (printed ver.)
ISSN 2703-8084 (electronic ver.)

Doctoral theses at NTNU, 2022:91

PRINTED IN
NORWAY
NO - 1598

NORDIC SWAN ECOLABEL
Printed matter
2041 0731

Printed by Skipnes Kommunikasjon AS

Time is the most precious resource that we have at hand.

Summary

Massive MIMO is a core technology for 5G cellular networks, that matured from a concept to commercial implementations over the last decade. It uses large-scale antenna systems to provide unprecedented access to the spatial domain of the radio propagation environment. This allows to exchange information with multiple users in the same time-frequency resource.

The work, summarised in this thesis, focuses on the performance of base stations with finite size antenna arrays. Specifically the service for non-average users is considered. To that extend, complete statistical distributions of the precoded or combined channel are used to describe the full performance range. The provided methods describe how the remaining small-scale fading can be quantified and compensated for. Moreover, an analysis of the gain gap between broadcast of synchronisation information and user-oriented traffic is provided. Even correlation between antenna elements based on their position, orientation and propagation environment can be considered. The results of this thesis enable insightful performance trade-offs of massive MIMO base stations in real world deployments.

Preface

This thesis has been submitted to the Norwegian University of Science and Technology (NTNU) in partial fulfilment of the requirements for the degree of philosophiae doctor (PhD). The work was carried out at the Circuit and Radio Systems group at the Department of Electronic Systems, under supervision of Prof. Nils Torbjörn Ekman (main supervisor) and Prof. Kimmo Kansanen (co-supervisor).

Acknowledgements

The dynamics of life follow wave pattern, it goes up and down and the process repeats. There are times where the next peak waits and there are times with valleys ahead. Every valley has its lesson and every peak provides new perspectives. I am grateful that I could spend the last five years in Trondheim to work towards a PhD. My long distance hike through universities is coming to a closure, making space for new adventures. The trip through valleys and over peaks has been more enjoyable due to people far and near. I would not have come so far without you.

Torbjörn, we have met for the first time in autumn 2012. You were teaching *Radio Communications* and I learned to appreciate radio propagation from an academic perspective. Little did I know, that we would work together and that you would use some of our results in your teaching a few years later. You consider time to be a renewable resource, I still doubt that and want to thank you for all the hours spent in front of your white board discussing science, engineering and being human. Kimmo, thank you for your always open door. At times, I left your office with more questions than the ones I had in the beginning. You have provided insight into external research projects, extra calendar time and the simplest task of the whole PhD period. The extra source of coffee was happily enjoyed.

Egil, thank you for allowing me to teach exercises and practicals of the antenna engineering course. It was a much welcomed variation to regular duty work. Golsa, we worked the first years on ReRaNP and spent love, sweat and tears on it. You accelerated the start of my work by a lot and I know now what you meant by being ready to finish. Ingulf, Terje and the ElPro lab apprentices, you have gotten the whole testbed to the impressive physical state it is in now. I would have loved to use it for more measurements.

Amy, Margot and Johannes, thank you for spending your energy and master thesis work on topics related to my research. You provided valuable visualisations and

gave me the opportunity to refine my understanding of central concepts in massive MIMO. Sara and Gilles, it has been a pleasure to see your work and to discuss our science as well as experiences as PhD students. Additionally, the IRACON COST action has provided the opportunity to present our work in a friendly environment. The COST meetings have been a place for all kinds of questions and honest answers.

Roger, without your persistence I might not have returned to Trondheim completely. Thank you for guiding me through day -1 and letting me be a femtosatellite with an alternative payload orbiting the small sat project. Nina, thank you for always being welcoming at the administration office and the introduction to Trondhjems Turistforenings Fjellsportgruppa. To you, Silje and the old library lunch group, thank you for many enriching discussions throughout the first few years. I have been missing the old library as meeting place ever since.

Elizabeth and Alberto, thank you for hanging out and showing me how to handle steep slopes in winter. We have been sitting in the same boat work wise and I enjoyed seeing you travelling through PhD lands to your own destinations. Evelyn, since you have moved to the small sat lab I could take your old office desk. Thank you for the climbing sessions and reoccurring questions about progress. Moreover, I enjoyed the writing group that you had been organising for some time.

Ginny and Joe, thank you for your come as you are attitude, open ears and hearts as well as walks through the neighbourhood. Marie, thank you adding plants our office window sill and for dropping by whenever you are back in town.

Dwellers of #ark and #wwyc, thank you for tips and entertainment. It has been great to have a place for exchange beyond the limitations of physical proximity. Grip Klatring & Sjøbadet, thank you for providing space to detach from all the busy thoughts a PhD student might have.

Gara, thank you for sharing your office and PhD journey with me. You have been more than just an office mate, you have always been there. Simone and Andreas, thank you for exploring the cliffs and rock faces in Trøndelag and beyond. Our weekend trips have eased the valleys and amplified the peaks. Øyvind, thank you

for providing different perspectives and naughty comments along the way. It is soothing to have you around. Asgeir, my lunch break walks have not been what they used to be since you finished. Thank you for sharing time at work and beyond, for being a last minute reviewer and for hiking wide and far with me. Ragni, Asgeir and Øyvind, you have made my return to Trondheim a smooth experience. Thank you for shared dinners and laughs.

Vielen Dank an die Echochamber mit Delaydi und Saetchmo für die wöchentlich erscheinende basstherapeutische Maßnahme. Lars, vielen Dank dafür bei dir in Berlin Zwischenhalte einlegen zu können und gemeinsam über Chaos, Funk und Weltraum nachzudenken. Nele, vielen Dank das du immer Zeit findest egal wann ich wieder in der Heimat bin. Jahreswechsel werden so zu einem angenehmen Zeitpunkt um inne zu halten und über Vergangenheit, Gegenwart, Gesellschaft und Zukünfte nachzudenken. Paul, vielen Dank für die häufigen Besuche und unsere gemeinsamen Wanderungen durch die norwegischen Landschaften. Der regelmäßige Austausch und dein Zuhören haben mir geholfen einen guten Weg durch die Doktorandenzeit zu finden.

Jan, vielen Dank für deine Zeit die du parallel zu Familie, Haus und Arbeit findest um im Gespräch zu bleiben. Ann-Katrin und dir möchte ich danken, Lotta und Hannes trotz der Distanz beim entdecken der Welt begleiten zu können. Mama und Papa, dank euch habe ich die Möglichkeit und Freiheit erst in England und nun in Norwegen tätig zu sein. Seit meinem Auszug sind es mehr Jahre in Norwegen als in Deutschland geworden. Das es so weit kommt hätte ich damals in Hogganvik nicht gedacht. An euch und die restliche Familie, vielen Dank für eure Unterstützung.

Jens Abraham
Eberswalde
December 2021

List of Authors Publications

The following list contains the publication that I had the pleasure to contribute to. The citation keys have prefixes for included publications ([J*] for journal and [C*] for conference manuscripts), related publications ([R*] published and [I*] for temporary documents presented in COST Action CA15104, "Inclusive Radio Communication Networks for 5G and beyond" (IRACON)) and additional publications ([A*]). Throughout this thesis, this designation discloses where we are referring to our own work. The additional publications are results from work that was carried out before joining NTNU.

Included Publications

[J1] G. Ghiaasi, J. Abraham, E. Eide, and T. Ekman, "Effective Channel Hardening in an Indoor Multiband Scenario", *International Journal of Wireless Information Networks*, vol. 26, no. 4, Jul. 2019. DOI: `10.1007/s10776-019-00438-7`

[J2] J. Abraham, P. Ramírez-Espinosa, and T. Ekman, "Statistics of the Effective Massive MIMO Channel in Correlated Rician Fading", *IEEE Open Journal of Antennas and Propagation*, vol. 3, pp. 238–248, Jan. 2022. DOI: `10.1109/OJAP.2022.3147015`. arXiv: `2112.06692`

[C1] J. Abraham and T. Ekman, "Power Inversion of the Massive MIMO Channel", in *Proceedings of the 2019 Symposium on Information Theory and Signal Processing in the Benelux (SITB2019)*, arXiv:1905.07555, Gent, Belgium: Werkgemeenschap Informatie- en Communicatietheorie (WIC) & IEEE Benelux Signal Processing Chapter, May 2019, pp. 3–7

[C2] J. Abraham and T. Ekman, "Achievable Synchronisation Gain In Uncalibrated Large Scale Antenna Systems", in *2020 14th European Conference on Antennas and Propagation (EuCAP)*, Mar. 2020, pp. 1–5. DOI: `10.23919/EuCAP48036.2020.9136063`

[C3] J. Abraham and T. Ekman, "Fading Margins for Large-Scale Antenna Systems", in *ICC 2021 - IEEE International Conference on Communications*, Montreal, QC, Canada: IEEE, Jun. 2021, pp. 1–5. DOI: `10.1109/ICC42927.2021.9500328`. arXiv: `2102.09903`

[C4] J. Abraham and T. Ekman, "Local Diversity and Ultra-Reliable Antenna Arrays", in *2021 55th Asilomar Conference on Signals, Systems and Computers*, Nov. 2021. arXiv: `2108.00712`, submitted and presented

Related Publications

[R1] G. Ghiaasi, J. Abraham, E. Eide, and T. Ekman, "Measured Channel Hardening in an Indoor Multiband Scenario", in *2018 IEEE 29th Annual International Symposium on Personal, Indoor and Mobile Radio Communications (PIMRC)*, arXiv:1812.05463, Bologna, Italy, Sep. 2018, pp. 1–6. DOI: `10.1109/PIMRC.2018.8581026`

[I1] G. Ghiaasi, J. Abraham, E. Eide, and T. Ekman, "Measured Channel Hardening in an Indoor Multiband Scenario", TD(18)07023, 7th technical IRACON meeting, Cartagena, Spain, May 2018

[I2] J. Abraham, G. Ghiaasi, and T. Ekman, "Characterisation of Channel Hardening Using the Diversity Order of the Effective Channel", TD(19)09072, 9th technical IRACON meeting, Dublin, Ireland, Jan. 2019

[I3] J. Abraham and T. Ekman, "Achievable Synchronisation Gain in Uncalibrated Large Scale Antenna Systems", TD(20)12011, 12th technical IRACON meeting, Louvain-la-Neuve, Belgium, Jan. 2020

Additional Publications

[A1] H. Bui Van, J. Abraham, Q. Gueuning, E. de Lera Acedo, and C. Craeye, "Further validation of fast simulation method at the element and array pattern levels for SKA", in *2016 10th European Conference on Antennas and Propagation (EuCAP)*, Apr. 2016, pp. 1–4. DOI: `10.1109/EuCAP.2016.7481791`

[A2] J. Abraham, E. Colin-Beltran, E. de Lera Acedo, and A. J. Faulkner, “A 16-element LPDA random sparse prototype array for the SKA AA-mid instrument”, in *2016 10th European Conference on Antennas and Propagation (EuCAP)*, Apr. 2016, pp. 1–4. doi: 10.1109/EuCAP.2016.7481792

[A3] J. Abraham, H. B. Van, E. de Lera Acedo, and C. Craeye, “Numerical modelling of SKA AA-Mid tile configurations using HARP”, in *2017 11th European Conference on Antennas and Propagation (EUCAP)*, Mar. 2017, pp. 3837–3841. doi: 10.23919/EuCAP.2017.7928253

[A4] H. Bui-Van, J. Abraham, M. Arts, Q. Gueuning, C. Raucy, D. González-Ovejero, E. de Lera Acedo, and C. Craeye, “Fast and Accurate Simulation Technique for Large Irregular Arrays”, *IEEE Transactions on Antennas and Propagation*, vol. 66, no. 4, pp. 1805–1817, Apr. 2018. doi: 10.1109/TAP.2018.2806222

[A5] E. de Lera Acedo, H. Pienaar, N. R. Ghods, *et al.*, “SKA LFAA Station Design Report”, Tech. Rep., Mar. 2020, arXiv: 2003.12744

Contents

Acronyms

$\mathcal{CN}$ complex normal 81
$\mathcal{CN}$-**RV** complex normal random vector 43, 138–142, 146, 148–150, 159, 165, 166
3GPP 3rd Generation Partnership Project 3, 121, 165
5G fifth generation mobile networks 6, 119
6G sixth generation mobile networks 119, 120

AI artificial intelligence 22
AoA angle of arrival 140
AWGN additive white Gaussian noise 4, 9, 106

BER bit error rate 5
BPSK binary phase shift keying 4
BS base station xxiii, xxiv, 3, 5, 7–10, 14–25, 28–33, 35–42, 44, 50–59, 61–63, 67, 68, 76–83, 86, 103, 132, 138, 140, 141, 148, 153, 158, 159, 161, 162, 164–166

CCDF complementary cumulative distribution function 82–85
CDF cumulative distribution function xxii, xxiv, 12–14, 29, 30, 33, 41, 42, 44, 61, 62, 66, 67, 82–85, 103, 105, 106, 109, 110, 121–128, 130, 132–136, 139, 140, 148–151, 159, 160, 165, 166
CGQF complex Gaussian quadratic form xxii–xxiv, 33, 34, 42, 43, 140, 149, 150, 157, 160, 161, 165
CIR channel impulse response 61
CSI channel state information 19, 20, 22–26, 28, 33, 35, 36, 39, 43, 44, 51, 138
CTF channel transfer function 51, 55, 57, 60, 61

DFT discrete Fourier transform 148
DKW Dvoretzky-Kiefer-Wolfowitz 122
DL downlink 51, 59–63, 66, 68, 69
DTR distributed time reversal 36, 80–84, 86

ECDF empirical cumulative distribution function xxv, 17, 18, 35, 40, 104, 106, 111, 113–115, 122, 123
ELAA extremely large aperture arrays 21, 39, 43, 44
eMBB enhanced mobile broadband 6

FDD frequency division duplex 19

FEC forward error correction 120

GSCM geometry-based stochastic channel model 23, 43
GSM Global System for Mobile Communications 3

HPBW half power beam width xxv, 53, 155, 156

IDFT inverse discrete Fourier transform 55, 57
iid independent identically distributed 10, 24, 32–34, 36, 144, 149
IoT internet of things 6, 7, 28, 35
IQR interquartile range 31
ISI inter-symbol-interference 9, 108, 111, 116

LOS line of sight 11, 40, 54, 113, 138
LPDA log-periodic dipole array 53
LSAS large-scale antenna system 3, 7, 21, 22, 27, 28, 30, 39, 41–43, 138, 139, 149, 166
LTE Long Term Evolution 3, 52

MGF moment-generating function xxiii, 149, 150
MIMO multiple-input multiple-output xiii, 3–8, 10, 12, 14–16, 18–28, 30, 31, 33, 37, 40, 42–44, 50, 52, 53, 59, 68, 76, 85, 104, 105, 108, 111, 120–122, 131, 138–140, 165, 166
MISO multiple-input single-output 59, 104
ML machine learning 22, 23
MMSE mimimum mean square error 10, 18, 78
mMTC massive machine-type communication 6, 7
MPC multi path component 57
MRC maximum ratio combining 10, 51, 124, 133, 134, 138, 139, 148
MRT maximum ratio transmission 10, 60, 78, 80, 83
MUI multi user interference 10, 16, 78, 104, 108

NI National Instruments 52, 53
NLOS non-line of sight 11, 35, 40, 56, 113
NTNU Norwegian University of Science and Technology iii, ix, 27, 33, 52

OFDM orthogonal frequency division multiplexing 55, 78

PAP peak-to-average power 80, 85, 86
PAS power angular spectrum xxiii, 42, 138, 140–143, 145, 146, 152–155, 158–166

PDF probability density function xxi, xxii, xxiv, 11–13, 41, 42, 44, 122, 127, 128, 134–136, 139–141, 143, 148–151, 153, 165, 166

PDP power delay profile xxiii, xxiv, 35, 36, 63–65, 81, 105, 115, 138, 140–144, 146

PI power inversion 36, 80–86

QAM quadrature amplitude modulation 4

QuaDRiGa Quasi Deterministic Radio Channel Generator 24

ReRaNP Reconfigurable Radio Network Platform 27, 28, 33, 49, 52

RIS reconfigurable intelligent surface 22

rms root mean square 49, 51, 61, 66, 68, 76

RMT random matrix theory 43, 165

RX receiver 61

SC selection combining 133, 134

SIC successive interference cancellation 23

SIMO single-input multiple-output 104

SINR signal-to-interference-plus-noise ratio xxv, 4, 18, 43, 108, 111, 116, 139

SISO single-input single-output 4, 23, 25, 57, 59, 60

SKA Square Kilometre Array 31

SMS Short Messaging Service 5

SNR signal-to-noise ratio xxiv, xxv, 3–6, 9–11, 14, 18, 22, 44, 51, 60, 108, 111, 116, 121, 130, 139

TDD time division duplex 7, 14, 19, 20, 52, 53, 59, 138

TR time reversal 10, 31, 36, 37, 40, 78, 80–84, 86

UE user equipment 50–57, 59, 61, 70

UL uplink 51, 52, 55, 59, 63

ULA uniform linear array 25, 26, 38, 42, 139, 140, 152, 153, 157, 158, 160–164, 166

UR ultra-reliability 30, 40, 41, 119–123, 127, 128, 130, 133–135

URA uniform rectangular array 21, 25, 26, 140

URLLC ultra-reliable low-latency communication 6, 7, 40, 119, 120, 131

USRP Universal Software Radio Peripheral 52

WLAN wireless local area network 3

WSN wireless sensor network 7, 35–37, 50, 52, 76–78, 86, 120

ZF zero-forcing 10, 18, 78

Symbols

$\star$ convolution
$(\cdot)^*$ conjugation
$(\cdot)^{\mathbf{H}}$ hermitian conjugate transpose
$(\cdot)^{\mathbf{T}}$ transpose
$|\cdot|$ absolute value (envelope)
$\|\cdot\|$ two-norm
$\mathbf{1}$ one vector
a_n plane wave scaling of the n-th wave
A_b power coupling of beam b
$\mathbf{A}$ operator matrix
b beam index
B number of beams branches
$\mathbf{B}$ beam sweeping matrix
c normalisation / scaling coefficent
  c_l normalisation coefficent for user l
  $c_l^{\mathbf{DTR}}$ normalisation coefficent for user l and distributed time reversal
  $c_l^{\mathbf{TR}}$ normalisation coefficent for user l and time reversal
  $c_l^{\mathbf{PI}}$ normalisation coefficent for user l and power inversion
$\mathbf{C}$ correlation matrix
$\mathcal{CN}$ complex normal distribution
$\mathbb{C}$ complex number
d scaling coefficient
Δd antenna spacing
$\mathcal{D}$ local diversity
D_0 maximum directivity
$D(\theta, \phi)$ antenna directivity
e noise coefficient
  $e[n]$ receiver noise on delay tap n
  $e_k[n]$ received noise at user k for delay tap n
  $\boldsymbol{e}$ noise vector
$\mathbb{E}\{\cdot\}$ expectation operator
  $\mathbb{E}_x\{\cdot\}$ expectation over x
f frequency / sub-carrier index
$f(\cdot)$ probability density function (PDF)
  $f_{\mathcal{CN}}(\cdot)$ PDF of a complex normal distributed variable
  $f_{\gamma}(\cdot)$ PDF of a non-central Gamma distributed variable
  $f_{\text{Rayleigh}}(\cdot)$ PDF of a Rayleigh distributed variable

  - $f_{\text{Rayleigh}^2}(\cdot)$ PDF of the squared envelope of a Rayleigh distributed variable
  - $f_{\text{Rice}}(\cdot)$ PDF of a Rice distributed variable
  - $f_{\text{Rice}^2}(\cdot)$ PDF of the squared envelope of a Rice distributed variable
  - f_Q PDF of a complex Gaussian quadratic form (CGQF)
  - $f_{\boldsymbol{S}_{L:L}}$ PDF of the maximum synchronisation gain
  - $f^{\mathbf{A}}$ PDF of the amplitude gain
  - $f^{\mathbf{P}}$ PDF of the power gain
- F number of sub-carriers
- $F(\cdot)$ cumulative distribution function (CDF)
  - $F_\gamma(\cdot)$ CDF of a non-central Gamma distributed variable
  - $F_{\text{Rayleigh}^2}(\cdot)$ CDF of the squared envelope of a Rayleigh distributed variable
  - $F_{\text{Rice}^2}(\cdot)$ CDF of the squared envelope of a Rice distributed variable
  - F_Q CDF of a CGQF
  - $F^{\mathbf{P}}$ CDF of the power gain
- $F_M(\cdot)$ fading margin
- $F(\theta, \phi)$ direction dependent shape of an antenna pattern
- $\boldsymbol{g}$ channel vector (incl. large-scale fading and path loss)
- $G_m(\theta, \phi)$ direction dependent gain pattern of antenna element m
- $G_{mk}[f]$ channel coefficient (incl. large-scale fading) for user k at antenna element m on sub-carrier f
- h channel coefficent
  - $\bar{h}$ deterministic channel coefficient
  - $\tilde{h}$ diffuse channel coefficient
  - $h_m[n]$ channel coefficient at antenna m for delay tap n
  - $h_{mk}[n]$ channel coefficient of user k at antenna m for delay tap n
  - $\boldsymbol{h}$ channel vector
  - $H_{mk}[f]$ channel coefficient of user k at antenna m on sub-carrier f
  - $\boldsymbol{H}$ channel vector
  - $\tilde{\boldsymbol{H}}$ diffuse component channel vector
  - $\bar{\boldsymbol{H}}$ specular component channel vector
- $\mathcal{H}$ effective channel coefficent
  - $\mathfrak{h}[n]$ effective channel coefficient for delay tap n
  - $\mathfrak{h}_k[n]$ effective channel coefficient of user k for delay tap n
  - $\mathfrak{h}_{kl}[n]$ effective channel coefficient for user k with weights for user l for delay tap n
  - $\mathfrak{H}_k[f]$ effective channel frequency response for user k on sub-carrier f
- i index
- $\mathbf{I}$ identity matrix
- $\mathrm{I}_a(x)$ Modified Bessel function of the first kind
- j index
- $\mathbf{j}$ imaginary unit

$\mathrm{J}_a(x)$ Bessel function of the first kind

k user-index

$\boldsymbol{k}$ wave vector

K number of users

$\mathcal{K}$ Rician $\mathcal{K}$-factor

- $\mathcal{K}_{l,t}$ Rician $\mathcal{K}$-factor in local area l for delay tap t

l local area index

- l_i local area index of antenna-tap index i
- l_j local area index of antenna-tap index j

L number of diversity branches

$\mathbf{L}$ matrix decomposition result

$\mathcal{L}$ leakage coefficient

m antenna index

- m_i antenna index of antenna-tap index i
- m_j antenna index of antenna-tap index j

M number of base station (BS) antennas

$M_{\mathcal{Q}}(\cdot)$ moment-generating function (MGF) of a CGQF

n delay tap index

- n_i delay tap index of antenna-tap index i
- n_j delay tap index of antenna-tap index j

N number of delay taps

$N_m[f]$ combined BS noise coefficient at antenna m on sub-carrier f

p probability

$p_k[n]$ power delay profile (PDP) coefficent of user k of delay tap n

$p(\theta, \phi)$ direction dependent power angular spectrum (PAS)

- $\bar{p}(\theta, \phi)$ deterministic direction dependent PAS
- $\tilde{p}(\theta, \phi)$ diffuse direction dependent PAS
- $p_{l,t}(\theta, \phi)$ direction dependent PAS in local area l and delay tap t

$\mathfrak{p}_k[n]$ effective PDP coefficent of user k of delay tap n

P transmit power

- $P_{\mathbf{DL}}$ transmit power (downlink)
- $P_{\mathbf{UL}}$ transmit power (uplink)
- $P_{mk}^{\mathbf{Ant,R}}$ relative transmit power of antenna element m for user k
- $P_{\mathbf{dif}}$ diffuse power
- P_e power of noise signal e
- $P_k^{\mathbf{BS,R}}$ relative BS transmit power for user k
- $P_{mk}^{\mathbf{RX,R}}$ relative effective received power for user k
- P_x power of signal x
- $\tilde{P}$ diffuse power
- $\bar{P}$ specular power

- $P_a(\cdot,\cdot)$ complementary Marcum Q-function of order a
- $Q(\cdot)$ inverse CDF (quantile function)
- $\mathcal{Q}$ effective channel power gain
- $\mathfrak{Q}_k[f]$ normalised power gain for user k on sub-carrier f
- $\boldsymbol{r}$ position vector
  - $\boldsymbol{r}_m$ position vector of antenna element m
- R number of samples
- $\mathfrak{R}_k[\Delta f]$ frequency correlation coefficient of user k for frequency offset Δf
- $S_{l,t}$ PDP coefficent for local area l and delay tap t
- $\boldsymbol{S}$ synchronisation gain vector
- $\boldsymbol{S}_{L:L}$ maximum synchronisation gain
- $\mathbf{SNR}$ signal-to-noise ratio (SNR)
- $\mathbf{SNR}_{\mathcal{H}}$ SNR of the effective channel
- $\mathbf{SNR}_{\mathbf{ref}}$ reference SNR
- $U_k(s)$ auxiliary variable of modified CGQF
  - $\tilde{U}_k(s)$ transformed auxiliary variable of modified CGQF
- $\boldsymbol{v}$ random vector
- $V_t(s)$ auxiliary variable of modified CGQF
  - $\tilde{V}_t(s)$ transformed auxiliary variable of modified CGQF
- $\mathbb{V}\{\cdot\}$ variance operator
- w combination / precoding weight
  - $w_m[n]$ weight for antenna element m and delay tap n
  - $w_{mk}[n]$ weight for user k at antenna m of delay tap n
  - $\boldsymbol{w}$ weight vector
  - $\boldsymbol{W}$ weight vector
  - $W_{mk}[f]$ weight for user k at antenna m on sub-carrier f
  - $W_{mk}^{\mathbf{MRT}}[f]$ MRT weight for user k at antenna m on sub-carrier f
- $w_\rho(x;\alpha,\mu)$ PDF of a non-central Gamma distribution
- $W_\rho(x;\alpha,\mu)$ CDF of a non-central Gamma distribution
- x transmit symbol
  - $x[n]$ BS transmit signal on delay tap n
  - $x_k[n]$ BS transmit signal for user k on delay tap n
- $X_k^{\mathbf{BS}}[f]$ BS transmit signal for user k on sub-carrier f
- $X_k^{\mathbf{UE}}[f]$ transmit signal of user k on sub-carrier f
- y received symbol
  - $y_{\mathbf{DL}}$ received symbol (downlink)
  - $y_{\mathbf{UL}}$ received symbol (uplink)
  - $y[n]$ user receive signal on delay tap n
  - $y_k[n]$ receive signal of user k on delay tap n
- $Y_m^{\mathbf{BS}}[f]$ BS receive signal at antenna element m on sub-carrier f

$Y_k^{\mathbf{UE}}[f]$ receive signal of user k on sub-carrier f
z plane wave index
Z number of plane waves
α Hermitian angle between channel vector and weight vector
β large-scale fading coefficient incl. path loss
  β_k large-scale fading coefficient for user k incl. path loss
$\gamma[n]$ instantaneous signal-to-interference-plus-noise ratio (SINR)
Γ mean SNR
$\gamma_\rho(\alpha, \beta)$ non-central Gamma distribution with index ρ, scale α and non-centrality β
$\Gamma(\rho, \alpha)$ Gamma distribution with shape ρ and scale α
δ_n Dirac delta on delay tap n
δ_{ij} Kronecker delta function for indices i and j
$\delta(\cdot)$ Direc delta function
ϵ error term
ζ order of generic cosine antenna pattern
η antenna efficiency
θ azimuth
  θ_0 reference azimuth of an antenna element
  $\bar{\theta}$ azimuth angle of deterministic component
  $\tilde{\theta}_0$ reference azimuth of diffuse component
  $\tilde{\theta}_n$ azimuth angle of plane wave n
  $\theta_{\mathbf{HPBW}}$ half power beam width (HPBW) in azimuth
κ parameter of von Mises distribution
λ wavelength
λ_i eigenvalue
μ mean value
  $\boldsymbol{\mu}$ mean vector
  $\tilde{\boldsymbol{\mu}}$ transformed mean vector
ξ target confidence for empirical cumulative distribution function (ECDF)
π pi
$\rho_{i,j}$ correlation coefficient between antenna-tap indices i and j
  $\rho_{i,j}^t$ correlation coefficient between antenna-tap indices i and j (related to tap t
  $\rho_{i,j}^{\mathbf{omni}}$ corr. coefficient of an omni-directional channel between antenna-tap indices i and j
σ^2 variance
  σ_e^2 noise variance
  $\boldsymbol{\Sigma}$ covariance matrix
τ_{rms} delay spread
  $\hat{\tau}_{rms}$ effective delay spread
  $\hat{\tau}_{rms}^i$ instantaneous effective delay spread
$\Delta\tau$ sample duration

ϕ polar angle / elevation
  $\bar{\phi}$ polar angle of deterministic component
  $\tilde{\phi}_n$ polar angle of plane wave n
φ_m phase on antenna element m
  $\varphi(\theta, \phi)$ phase of an incident plane wave
  $\bar{\varphi}$ phase due to discrete channel component
  $\tilde{\varphi}_{n,m_i}(\tilde{\theta}_n, \tilde{\phi}_n)$ phase due to plane wave n on antenna element m_i
$\Delta\varphi_{m_i,m_j}$ phase offset between antenna elements m_i and m_j
χ^2 χ-squared distribution
χ'^2 non-central χ-squared distribution
ψ opening angle of sector channel
Ω full sphere integration surface

Remarks on the Notation

Variables may be complex valued. Coefficients o, vectors $\boldsymbol{o}$ and matrices $\mathbf{o}$ are written in italic normal font, bold italic font and bold upright font, respectively. Elements of vectors and matrices, potentially enclosed in square brackets, are indexed with subscripts, e.g. $\boldsymbol{o}_i$, $[\boldsymbol{o}]_i$, $[\mathbf{o}]_{ij}$ and $\mathbf{o}_{ij}$. Square brackets are used where it is not clear if different vectors and matrices or their elements are referenced.

Part I

Introduction

1 Introduction to Massive MIMO

> Any sufficiently advanced technology is
> indistinguishable from magic.
>
> Arthur C. Clarke

Wireless communication stands at the core of modern society. It enables humankind to access and exchange information anytime, everywhere and even beyond the limits our home planet. Services like terrestrial radio, satellite television, mobile telephony, instant messaging or remote control of rovers on other planets are just a few examples that require wireless technology. Guglielmo Marconi demonstrated in 1901 successfully the first transatlantic transmission, showcasing the potential of the technology. Meanwhile, the wireless community has provided several advancements and breakthroughs resulting in today's omnipresence of applications. Together, Academia, industry and standardisation bodies drive the development, documentation and coordination of wireless technology forward. E.g. the Wi-Fi Alliance takes care of the 802.11 standards for wireless local area network (WLAN) [1] and the 3rd Generation Partnership Project (3GPP) coordinates the standards related to cellular networks like: Global System for Mobile Communications (GSM), Long Term Evolution (LTE) and 5G [2].

This thesis focuses on *massive multiple-input multiple-output (MIMO)* base stations (BSs) with finite size large-scale antenna system (LSAS). The main goal is the description of methods for the analysis of single users that current systems neglect by optimising the average performance. To that extend, necessary background information is provided in the following introductory chapter. The next sections discuss general cellular network centric performance measures and highlight differences of applications that are not human-centric. A general system model is provided, allowing for a stochastic description of the signal-to-noise ratio (SNR). This basis is used to explain the core features of massive MIMO, namely *channel hardening* and *favourable propagation*.

An important peculiarity of wireless communications is the shared medium. Interference can arise unintentionally by other services operating over the same spectrum or intentionally to jam a wireless system. The the signal-to-interference-plus-noise ratio (SINR) captures the deterioration of the SNR.

Driving factors for the advancements of cellular systems have been performance improvements of energy and spectral efficiency, coverage, reliability and interference suppression. Information theory provides the Shannon-Hartley theorem for the capacity of a single-input single-output (SISO) link in additive white Gaussian noise (AWGN) [3]:

$$\text{Capacity}\left[\frac{\text{bit}}{\text{s}}\right] = \text{Bandwidth [Hz]} \times \log_2\left(1 + \text{SNR}\right). \tag{1.1}$$

The channel capacity is the maximum rate at which information can be transmitted without error. The equation provides multiple insights: Increasing the spectral bandwidth provides more capacity than improvements of the SNR or SINR. This is one reason why higher carrier frequencies are being used in modern systems. More spectral bandwidth can be allocated to each user, which increases the capacity if the SINR is kept constant. Furthermore, increased pathloss helps to reduce interference to unintended users. Normalising the achieved rate with the bandwidth of the system leads to the spectral efficiency with unit bit/(s Hz). This measure describes how efficiently a Hertz of bandwidth is used to transfer information. One way of improving the spectral efficiency of a transmission is the usage of higher order modulation schemes. Fig. 1.1 compares uncoded binary phase shift keying (BPSK) and multiple uncoded quadrature amplitude modulations (QAMs) with the capacity bound, showing that a better SNR allows for more complicated modulation schemes.

The data rate can be increased beyond the single link limit, if MIMO techniques are used. Multiple antennas enable the parallel transmission of information, if the spatial branches are orthogonal. This allows to extend the capacity in Eqn. (1.1) to the sum capacity:

$$\text{Sum Capacity}\left[\frac{\text{bit}}{\text{s}}\right] = \sum_{\substack{\text{orthogonal}\\ \text{branches}}} \text{Branch Capacity}\left[\frac{\text{bit}}{\text{s}}\right]. \tag{1.2}$$

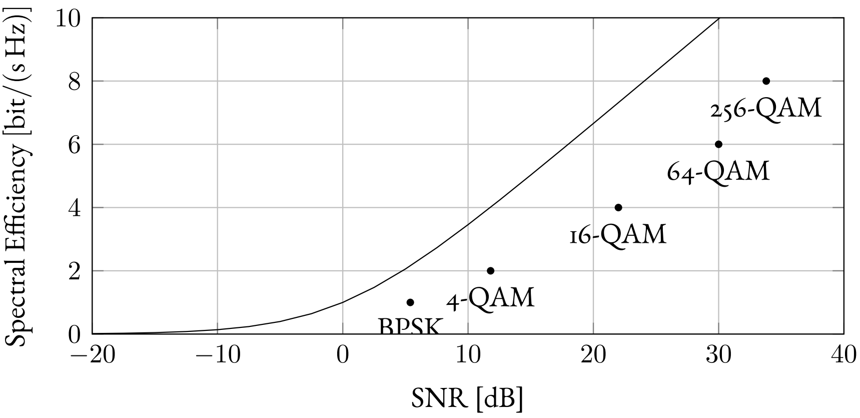

Figure 1.1: The limiting spectral efficiency of the capacity bound is compared with the minimum SNR of different uncoded modulation schemes to achieve a bit error rate (BER) of 1×10^{-4}.

Basically, MIMO enables spatial multiplexing if the radio channel in combination with the antenna systems provides enough degrees of freedom.

The evolutionary step of massive MIMO is the change of perspective from a single link between two stations, to a cellular system where a BS serves multiple users in parallel. Multiple antennas on one side of a MIMO link belong to multiple physically separated users to exploit the spatial selectivity of the radio channel. Thereby, the cell throughput is increased, serving multiple users in the same time-frequency resource.

Throughput plays a major role for the revenue of a cellular network operator, since telephony and Short Messaging Service (SMS) have become part of flat rate tariffs. The income is mainly connected to the combined data traffic provided to customers and network costs scale with spectral bandwidth due to license costs and the deployment density of cells. Unfortunately, aspects like coverage or fair distribution of resources in a cell are not directly connected to the revenue. They are more difficult to assess continuously and harder to explain to a customer.

In addition, a recent preprint is challenging the usefulness of wireless physical layer research [4]. The authors, based on econometric methodologies, assess that improvements of cellular networks have mainly been made through densification and increased spectrum usage. A much smaller impact on overall system performance is coming from advancements in academic research.

Both observations illuminate a central issue, throughput centric research is not necessarily improving cellular networks to a large extent. Moreover, a focus on throughput has the tendency to mainly improve the performance of users that are already sufficiently served. In contrast, the analysis of the (instantaneous) performance of individual single users, provided in this thesis, helps to evaluate users that are not covered by current systems concerned with improving the average performance. This analysis requires the full distribution of massive MIMO radio channels and not only their expectation captured by the SNR.

1.1 Applications

Assuming that all the implementation details of massive MIMO are sorted out and multiple users can be served at the same time, then additional use cases can be supported by fifth generation mobile networks (5G) cellular networks or application specific systems. The 5G standardisation process has focused particularly on [5]:

- enhanced mobile broadband (eMBB),
- massive machine-type communication (mMTC),
- ultra-reliable low-latency communication (URLLC).

eMBB is the use case that extends the standard capabilities of cellular networks for (human) mobile users by increasing peak data-rates per terminal, such that applications like augmented reality can be realised. This is in a sense the evolution of 4G systems with the same user group in mind.

Wireless communication for different users groups is at the centre of the other two focus areas. mMTC provides connectivity between machines for the internet of things (IoT) [6] or wireless sensor network (WSN) [7]. Some applications, especially in safety critical areas, require URLLC.

All applications have different requirements with respect to data traffic pattern, uplink and downlink rates or latency. A WSN might report sensor data in a regular interval (weather station data) or event based (forest fire detection), but has the tendency to be uplink focused and might not even need a downlink in extreme cases. An IoT network, especially in industrial contexts, might combine the acquisition of sensor data with optimisation and control of production process parameters, which balances up- and downlink traffic. Massive MIMO can be a key factor in all three mentioned domains, but will most likely have more impact on mMTC by increasing the number of served users per area due to favourable propagation and URLLC by increasing the robustness of each individual link by channel hardening. Especially for the implementation of URLLC, massive MIMO appears to be the most promising technology today.

1.2 System Model

This section will introduce a system model to describe the wireless communication between a single user and a BS. The system model is the foundation to understand different aspects of massive MIMO and LSAS. The classic time division duplex (TDD) case, where uplink and downlink are sharing the same frequency band [8], is considered. This allows to use pilot symbols in the uplink to estimate the channel efficiently for reciprocity based precoding in the downlink.

A complex valued symbol x is transmitted and the BS provides spatial realisations for M elements of a LSAS in either up- or downlink. The transmitted symbol potentially spreads over N delay taps at the receiver. Stacking the N delay taps for each antenna element m results in a complex valued vector $\boldsymbol{g}$ where MN elements are used to describe the radio propagation. The depicted massive MIMO system is outlined in Fig. 1.2.

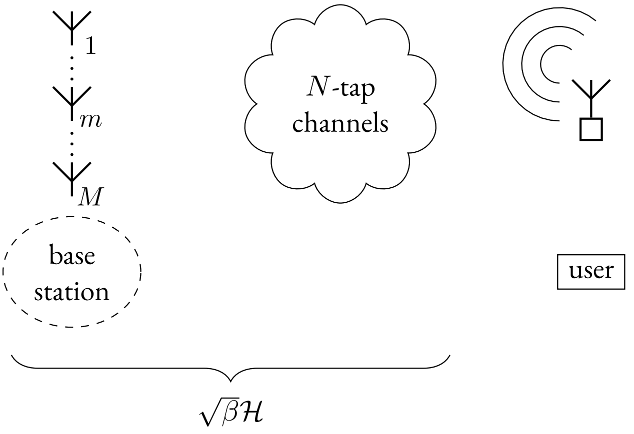

Figure 1.2: A massive MIMO BS with M antenna elements interacts with a user through M N-tap channels. The user can only observe the precoded effective channel $\mathcal{H}$ after superposition by the radio propagation environment under consideration of large-scale fading and path loss β.

The uplink- and downlink-case have a similar input-output relation for the received symbol y:

$$y_{\text{UL}} = \boldsymbol{w}^{\text{T}} \left(\boldsymbol{g}x + \boldsymbol{e}\right) = \sqrt{\beta}\boldsymbol{w}^{\text{T}}\boldsymbol{h}x + \boldsymbol{w}^{\text{T}}\boldsymbol{e} = \sqrt{\beta}\mathcal{H}x + \boldsymbol{w}^{\text{T}}\boldsymbol{e}, \tag{1.3a}$$

$$y_{\text{DL}} = \boldsymbol{g}^{\text{T}}\boldsymbol{w}x + e = \sqrt{\beta}\boldsymbol{h}^{\text{T}}\boldsymbol{w}x + e = \sqrt{\beta}\mathcal{H}x + e, \tag{1.3b}$$

where the contributing noise sources, covered by e and $\boldsymbol{e}$, differ. The channel coefficients in $\boldsymbol{g}$ can be split into a large-scale fading and path loss coefficient $\sqrt{\beta}$ and a small-scale fading vector $\boldsymbol{h}$, so that the effective channel $\mathcal{H} = \boldsymbol{w}^{\text{T}}\boldsymbol{h}$ describes the small-scale fading effects including the combination or precoding strategy. The effective channel $\mathcal{H}$ is an important abstraction to describe the input-output relation from the perspective of a user, where the complex interaction of each branch with the propagation environment is reduced to a single coefficient. In the uplink case, the weight vector $\boldsymbol{w}$ is combining the noise of every branch non-coherently, whereas in the downlink case the weights only interact with the transmit symbol. Moreover, the downlink weight vector influences the actual transmit power. Therefore, it has to adhere to restrictions of the element or BS output power (details are presented in [C1]). The uplink noise vector $\boldsymbol{e}$ captures the AWGN of the different branches. The downlink noise term e corrupts the combined symbol at the user. Inter-symbol-interference (ISI) is not modelled in the introduction, since it has no significant impact on systems discussed in this thesis [J1]. Still, the more involved multi-user case is described in the delay domain for the model used in [C1].

1.3 Signal to Noise Ratio

Inspection of the system model in the previous section shows that the SNR of the link between user and BS depends on the following factors:

- the power P of the transmit symbol,
- the attenuation due to large-scale fading β,
- the noise terms $\boldsymbol{e}$ and e,
- and the statistics of the effective channel power gain $\mathcal{Q} = |\mathcal{H}|^2$.

To isolate the effect of small scale fading, a reference SNR for a local area is defined:

$$\mathrm{SNR}_{\mathrm{ref}} = \beta \frac{P}{\sigma_e^2}. \tag{1.4}$$

The reference SNR depends on the large-scale fading and propagation loss β, the BS or user transmit power P and the noise variance σ_e^2. The transmit power in the uplink is purely depending on the symbols:

$$P_{\mathrm{UL}} = \mathbb{E}\{|x|^2\}, \tag{1.5}$$

whereas the BS transmit power also depends on the norm of the weight vector:

$$P_{\mathrm{DL}} = \|\boldsymbol{w}\|_2^2 \, \mathbb{E}\{|x|^2\}. \tag{1.6}$$

The SNR expression in uplink and downlink, considering independent identically distributed (iid) noise for the BS antenna elements, results in:

$$\mathrm{SNR}_{\mathrm{UL}} = \frac{\mathbb{E}_x\left\{\left|\sqrt{\beta}\mathcal{H}x\right|^2\right\}}{\mathbb{E}_{\boldsymbol{e}}\left\{\left|\boldsymbol{w}^{\mathrm{T}}\boldsymbol{e}\right|^2\right\}} = \beta\frac{\mathbb{E}\left\{|x|^2\right\}}{\sigma_e^2}\frac{|\mathcal{H}|^2}{\|\boldsymbol{w}\|_2^2} = \beta\frac{P_{\mathrm{UL}}}{\sigma_e^2}\frac{|\mathcal{H}|^2}{\|\boldsymbol{w}\|_2^2}, \tag{1.7a}$$

$$\mathrm{SNR}_{\mathrm{DL}} = \frac{\mathbb{E}_x\left\{\left|\sqrt{\beta}\mathcal{H}x\right|^2\right\}}{\mathbb{E}_e\left\{|e|^2\right\}} = \beta\frac{\mathbb{E}\left\{|x|^2\right\}}{\sigma_e^2}|\mathcal{H}|^2 = \beta\frac{P_{\mathrm{DL}}}{\sigma_e^2}\frac{|\mathcal{H}|^2}{\|\boldsymbol{w}\|_2^2}. \tag{1.7b}$$

Both equations show the same structure:

$$\mathrm{SNR} = \mathrm{SNR}_{\mathrm{ref}}\frac{|\mathcal{H}|^2}{\|\boldsymbol{w}\|_2^2} = \mathrm{SNR}_{\mathrm{ref}}\mathrm{SNR}_{\mathcal{H}} \tag{1.8}$$

where the only difference is the dependence of the BS output power on the weight vector. This highlights that $\mathcal{H}$ is the effective channel coefficient, which can be formed by applying weights according to maximum ratio combining (MRC) [9], maximum ratio transmission (MRT) [10], time reversal (TR) [11], π or other strategies. There are additional strategies like zero-forcing (ZF) or mimimum mean square error (MMSE) that take multi user interference (MUI) into account. That means that the weight vector $\boldsymbol{w}$ is chosen not only considering the channel vector of the intended user, but the channel vectors of other users too.

For the focus of this thesis, orthogonality between users needs to be provided by other measures than interference suppression, since every interference suppression strategy compromises the signal of the intended user. One of those measures is favourable propagation, an aspect of massive MIMO which will be introduced later. Scheduling over timeslots can orthogonalise the remaining users that have too similar channel vectors.

Many of the named combination and precoding strategies are based on the conjugate of the channel element together with some common normalisation c:

$$\boldsymbol{w} = \frac{\boldsymbol{h}^*}{c}. \tag{1.9}$$

Evaluating $\mathrm{SNR}_{\mathcal{H}}$ for those weights gives:

$$\mathrm{SNR}_{\mathcal{H}} = \frac{|\mathcal{H}|^2}{\|\boldsymbol{w}\|_2^2} = \frac{|\boldsymbol{w}\boldsymbol{h}|^2}{\|\boldsymbol{w}\|_2^2} = \frac{\left|\frac{1}{c}\boldsymbol{h}^{\mathrm{H}}\boldsymbol{h}\right|^2}{\frac{1}{|c|^2}\|\boldsymbol{h}\|_2^2} = \|\boldsymbol{h}\|_2^2 \,. \tag{1.10}$$

This shows that $\mathrm{SNR}_{\mathcal{H}}$ is invariant to a normalisation applied to the weight vector for a large group of strategies. It solely depends on the quadratic form of the channel vector. Moreover, conjugate weights are optimal, since all contributing branches are phase aligned before summation.

1.4 Fading Distributions

This section introduces distributions to describe the individual random small-scale fading of every branch. These are building blocks of the effective channel power gain. Hence, the instantaneous SNR will fluctuate randomly and can be characterised with a distribution based on the branch distributions.

Classic line of sight (LOS) and non-line of sight (NLOS) scenarios are associated with Rayleigh and Rician fading, respectively. For the former, a large number of independent plane waves impinges on an antenna element from multiple directions. For the latter, an additional deterministic plane wave is superimposed with the continuum of indpenden plane waves. The deterministic wave can arise from LOS propagation or a specular reflection, whereas all other plane waves belong to the diffuse scattering part of the channel. The large number of plane waves allows to apply the central limit theorem, which means that the superposition of all plane waves gives rise to a complex normal distribution of the channel coefficient. The deterministic plane wave is associated with the mean μ and the diffuse channel with the variance σ^2 of that distribution:

$$h \sim \mathcal{CN}\left(\mu, \sigma^2\right) . \tag{1.11}$$

The probability density function (PDF) $f_{\mathcal{CN}}(h)$ is [12]:

$$f_{\mathcal{CN}}(h) = \frac{1}{\pi\sigma^2} \exp\left(-\frac{(h-\mu)^*(h-\mu)}{\sigma^2}\right) . \tag{1.12}$$

Since sorting complex numbers is ambiguous, a general cumulative distribution function (CDF) can not be provided.

For the envelope $|h|$, the PDF f_{Rice} is [13]:

$$f_{\mathrm{Rice}}(|h|) = \frac{2\,|h|}{\sigma^2} \exp\left(-\frac{|h|^2 + |\mu|^2}{\sigma^2}\right) \mathrm{I}_0\left(\frac{2\,|h|\,|\mu|}{\sigma^2}\right), \tag{1.13}$$

with I_0 being the zeroth order modified Bessel function of the first kind. Using the quadratic form $|h|^2$ simplifies the envelope PDF further:

$$f_{\mathrm{Rice}^2}(|h|^2) = \frac{1}{\sigma^2} \exp\left(-\frac{|h|^2 + |\mu|^2}{\sigma^2}\right) \mathrm{I}_0\left(\frac{2\,|h|\,|\mu|}{\sigma^2}\right). \tag{1.14}$$

The CDF of the quadratic form can be expressed compactly with the complementary Marcum Q-function $P_a(x, y)$ [14] as defined in (8.5), such that:

$$F_{\mathrm{Rice}^2}(|h|^2) = P_1\left(\frac{|\mu|^2}{\sigma^2}, \frac{|h|^2}{\sigma^2}\right) = F_{\mathrm{Rice}}(|h|). \tag{1.15}$$

The CDF of the quadratic form and the envelope are similar, only the argument of the function differs. Setting $\mu = 0$ allows to express PDFs and CDFs for the Rayleigh case:

$$f_{\mathrm{Rayleigh}}(|h|) = \frac{2\,|h|}{\sigma^2} \exp\left(-\frac{|h|^2}{\sigma^2}\right), \tag{1.16}$$

$$f_{\mathrm{Rayleigh}^2}(|h|) = \frac{1}{\sigma^2} \exp\left(-\frac{|h|^2}{\sigma^2}\right), \tag{1.17}$$

$$F_{\mathrm{Rayleigh}^2}(|h|^2) = 1 - \exp\left(-\frac{|h|^2}{\sigma^2}\right) = F_{\mathrm{Rayleigh}}(|h|). \tag{1.18}$$

The quadratic form distribution of Rician fading belongs to the class of *non-central Gamma distributions* $\gamma_\rho(\alpha, \beta)$. The PDFs of the quadratic form of Rician

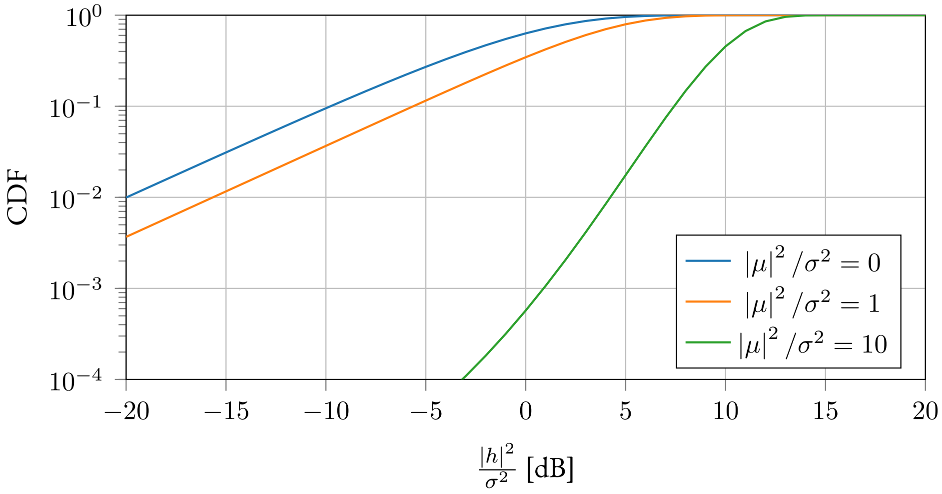

Figure 1.3: The CDFs of Rayleigh ($\mu = 0$) and Rician fading channels are shown. A growing deterministic component in the radio propagation environment reduces the probability of low effective channel gains.

fading is a particularisation with index $\rho = 1$, scale $\alpha = \sigma^2$ and non-centrality parameter $\beta = |\mu|^2/\sigma^2$.

$\gamma_\rho(\alpha, \beta)$ has the general PDF f_γ [15, Eqn. (1.47')]:

$$f_\gamma(x) = \begin{cases} \frac{1}{\alpha} \exp\left(-\frac{x}{\alpha} - \beta\right) \left(\frac{x}{\alpha\mu}\right)^{\frac{1}{2}(\rho-1)} \mathrm{I}_{\rho-1}\left(2\sqrt{\frac{x\mu}{\alpha}}\right) & x > 0 \\ 0 & x \leq 0 \end{cases} \tag{1.19}$$

and corresponding CDF F_γ [C4]:

$$F_\gamma(x) = P_\rho\left(\beta, \frac{x}{\alpha}\right). \tag{1.20}$$

For Rayleigh fading, $\gamma_\rho(\alpha, \beta = 0)$ is fully described by the better known (central) Gamma distribution $\Gamma(\rho, \alpha)$.

The envelope and quadratic form can be expressed in decibel, which counteracts the differences of the CDFs by the decibel scaling for powers and envelopes.

Fig. 1.3 shows a few CDFs for the effective channel of a single antenna single tap link with variance normalisation. This reflects the scenario where deterministic components with varying power are blocked by the environment and the diffuse propagation is fixed. A strong deterministic component increases the steepness of the CDF and reduces the probability of low SNR.

1.5 Massive MIMO

Massive MIMO has been conceptualised [16], experimentally tested and commercially implemented in the 2010s [8], [17], [18]. The general idea is to increase the number of antenna elements at the BS to exploit the spatial diversity of the radio channel. The concept diverged from standard MIMO and considers a cellular network, where multiple spatially distributed users are considered as one end of the communication system. This approach exploits that the radio channel differs between distant users. Having multiple antennas per user and favourable propagation, these radio channels orthogonalise. Multiple users can use the same time-frequency resource in parallel. Additionally, each and every radio channel to specific users is subject to channel hardening, which reduces the variability of the effective channel.

Central to the performance improvements of massive MIMO is the scalability of BS antenna elements. If TDD is used, then increasing the number of elements has no overhead penalty on the uplink channel estimation, because ll antenna elements receive pilot signals in parallel. Relying on channel reciprocity, the channel changing negligibly between up- and downlink, channel hardening and favourable propagation arise even for finite array sizes. Their aspects are described in the next subsections.

1.5.1 Channel Hardening

Channel hardening is best introduced in a Rayleigh fading scenario with independent antenna elements. More complex cases are discussed in later parts of this thesis. Let a random vector $\boldsymbol{h} \sim \mathcal{CN}_M(0, \mathbf{I})$ describe the small-scale fading in the propagation environment. Moreover, $\boldsymbol{h}$ includes the array gain of a BS with M antenna elements:

$$\mathbb{E}\{\mathrm{SNR}_{\mathcal{H}}\} = \mathbb{E}\{\|\boldsymbol{h}\|_2^2\} = \mathbb{E}\left\{\sum_{m=1}^{M} |[\boldsymbol{h}]_m|^2\right\} = \sum_{m=1}^{M} \mathbb{E}\{|[\boldsymbol{h}]_m|^2\} = M. \tag{1.21}$$

The last equation shows a decomposition of $\mathrm{SNR}_{\mathcal{H}}$ into a sum over independent quadratic forms, such that:

$$\|\boldsymbol{h}\|_2^2 \sim \gamma_M(1,0) = \Gamma(M,1). \tag{1.22}$$

A widely used measure of channel hardening is described in [19, Eqn. (2.17)], where the squared coefficient of variation of the effective channel is supposed to go towards zero for a growing number of antennas:

$$\frac{\mathbb{V}\{\|\boldsymbol{h}\|^2\}}{\left(\mathbb{E}\{\|\boldsymbol{h}\|^2\}\right)^2}. \tag{1.23}$$

The authors noted that a value of 10^{-2} is sufficient to obtain channel hardening. For the independent Rayleigh fading scenario, variance and mean of $\Gamma(M,1)$ are readily available to evaluate the measure as: $1/M$. Hence, channel hardening could be achieved by 100 antenna elements.

In this thesis, alternative measures of channel hardening are provided, namely a *fading margin* [C3] and a *local diversity* measure [C4]. For the sake of the introduction, only the fading margin is covered in the next paragraph, because a more detailed discussion of both measures is provided in sec. 3.1. The fading margin describes the amount of power needed to overcome the remaining small-scale fading of the effective channel and provides a link budget motivated insight into massive MIMO BS design. Fig. 1.4 shows the result for the independent Rayleigh scenario, so that 99.9 % of the channel realisations are above the target threshold (median of the uncompensated fading channel). A growing BS antenna array has diminishing returns, since the curve flattens out. E.g. 64 independent branches provide a fading margin of 1.8 dB. Doubling the number of antenna elements

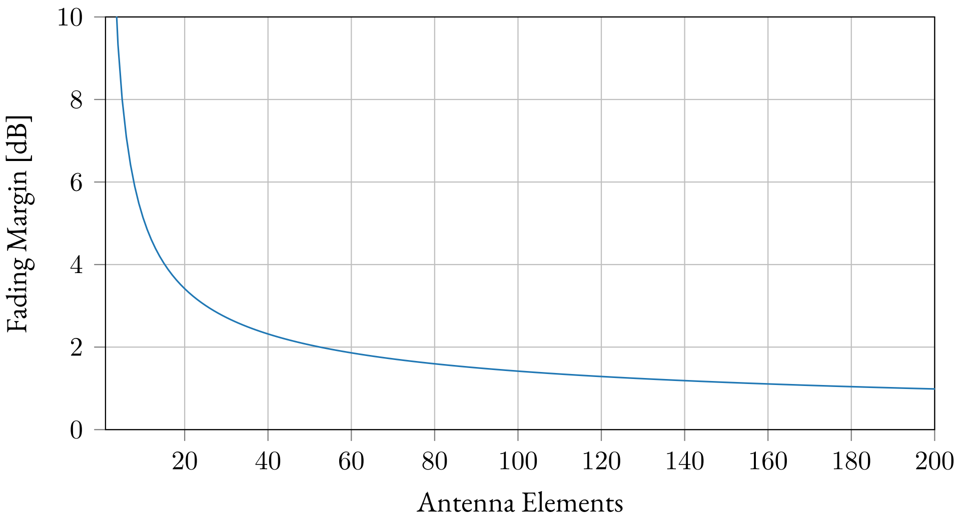

Figure 1.4: The fading margin to compensate 99.9 % of the channel realisations is shown for a BS with a growing number of antenna elements. About 50 independent elements provide a fading margin reduction to 2 dB for the chosen target outage.

improves the margin by 0.6 dB to 1.2 dB. Hence, there is little benefit to be expected from increasing the number of antenna elements beyond an application dependent point.

1.5.2 Favourable Propagation

Since massive MIMO usually assumes orthogonal pilots in the uplink, favourable propagation can be seen as a feature of downlink transmissions. Basically, MUI is reduced the more antenna elements a BS is equipped with, since all the transmit signals have to be superimposed constructively at the intended user. This reduces the probability of constructive superposition at unintended users. Favourable propagation can be quantified considering two channel vectors $\boldsymbol{h}_1$ and $\boldsymbol{h}_2$ by [19, Eqn. (2.19)]:

$$\mathbb{V}\left\{\frac{\boldsymbol{h}_{\mathbf{1}}^{\mathrm{H}}\boldsymbol{h}_{\mathbf{2}}}{\sqrt{\mathbb{E}\{\|\boldsymbol{h}_{\mathbf{1}}\|_2^2\}\,\mathbb{E}\{\|\boldsymbol{h}_{\mathbf{2}}\|_2^2\}}}\right\}. \tag{1.24}$$

This variance goes towards zero for an increasing number of BS antenna elements.

Since this thesis focuses on the single user performance, favourable propagation has not been discussed in detail in the attached publications. Nonetheless, a structural similar measure to the achievable synchronisation gain [C2] can be used to quantify favourable propagation with a link budget perspective in mind. A leakage coefficient $\mathcal{L}$:

$$\mathcal{L} = \frac{\boldsymbol{w}_{\mathbf{1}}^{\mathrm{T}}\boldsymbol{h}_{\mathbf{2}}}{\|\boldsymbol{w}_{\mathbf{1}}\|_2\,\|\boldsymbol{h}_{\mathbf{2}}\|_2} \tag{1.25}$$

where the weight vector $\boldsymbol{w}_{\mathbf{1}}$ targets the intended user and the channel vector $\boldsymbol{h}_{\mathbf{2}}$ covers the propagation to an unintended user gives an input-output relation of the remaining interference. Geometrically, $\mathcal{L}$ describes the Euclidean angle between two complex valued vectors [20].

To demonstrate the behaviour of favourable propagation, two uncorrelated users suspect to Rayleigh fading over M independent antenna elements

$$\boldsymbol{h}_{\mathbf{1}}, \boldsymbol{h}_{\mathbf{2}} \sim \mathcal{CN}_M(0, \mathbf{I}) \tag{1.26}$$

are considered. With the conjugate precoder (Eqn. (1.9)), the leakage coefficient becomes:

$$\mathcal{L} = \frac{\sum_{m=1}^{M} [\boldsymbol{h}_{\mathbf{1}}^{*}]_m\,[\boldsymbol{h}_{\mathbf{2}}]_m}{\sqrt{\|\boldsymbol{h}_{\mathbf{1}}^{*}\|_2^2\,\|\boldsymbol{h}_{\mathbf{2}}\|_2^2}}. \tag{1.27}$$

The structure of the equation shows a sum over independent complex Double Gaussians [21] normalised by the square-root over the product of two non-central Gamma distributions. Hence, distribution functions for $\mathcal{L}$ are not simple and Monte Carlo simulations of $\mathcal{L}$ generate the ECDFs for Fig. 1.5. The Fig. shows the complementary ECDF to highlight when the leakage power gain exceeds a certain threshold. Increasing the number of antennas reduces this probability and the expectation of the quadratic form of the leakage coefficient takes the form of

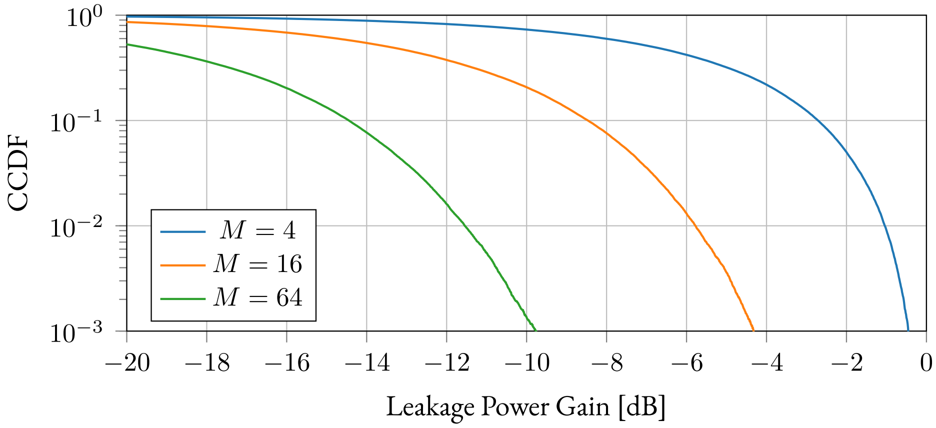

Figure 1.5: Complementary empirical cumulative distribution functions (ECDFs) of the leakage power gain between an intended and an unintended user are shown for (normalised) conjugated precoding. The leakage power gain is reduced for a larger number of antenna elements due to favourable propagation.

Eqn. (1.24). Evaluating this expectation for the described scenario shows a scaling of $1/M$ for the leakage power gain.

This is the ideal scaling for conjugate precoding without correlation between the two users as well as the antenna elements of the BS array. Hence, it can be expected that the leakage in real world scenarios scales slower towards zero. As mentioned earlier, precoding strategies like ZF and MMSE can reduce the leakage power gain to improve the SINR of unintended users, but it will compromise the SNR of the intended user.

2 Research Overview

> Deep in the human unconscious is a
> pervasive need for a logical universe that
> makes sense. But the real universe is always
> one step beyond logic.
>
> Frank Herbert

This chapter gives a selection of topics in massive MIMO that are adjacent to the focus of this thesis. The field has developed fast over the last decade and a database query with the search term *massive MIMO* returns more than 1400 publications per year for the period from 2017 to 2020 (see Fig. 2.1). Hence, this chapter can only give a broad overview over the development of the field.

The general concept of massive MIMO [16] has been summarised in a few magazine style publications [22], [23]. Furthermore, two books have been published that give a general introduction with focus on network aspects [19], [24]. An interesting way of discussing aspects and areas of misunderstanding is provided by a manuscript about myths surrounding massive MIMO systems [25].

Massive MIMO was introduced under the assumption of TDD. Unfortunately, legacy mobile networks operate with different up- and downlink frequency bands. To support frequency division duplex (FDD) operation, channel reciprocity has to be sacrificed and it is still an open question, how to exploit spatial diversity properly. Finding efficient solutions would ease upgrades of legacy cellular networks. To overcome the lack of reciprocity, channel state information (CSI) feedback allows to focus the downlink towards each individual user. It consumes extra resources and trades channel estimate accuracy and data-throughput off. This solution is less desirable than the TDD approach as it ultimately limits the scaling of BS antenna elements. At least slow mobility scenarios can be served, since slower channel evolution might require fewer CSI feedback resources.

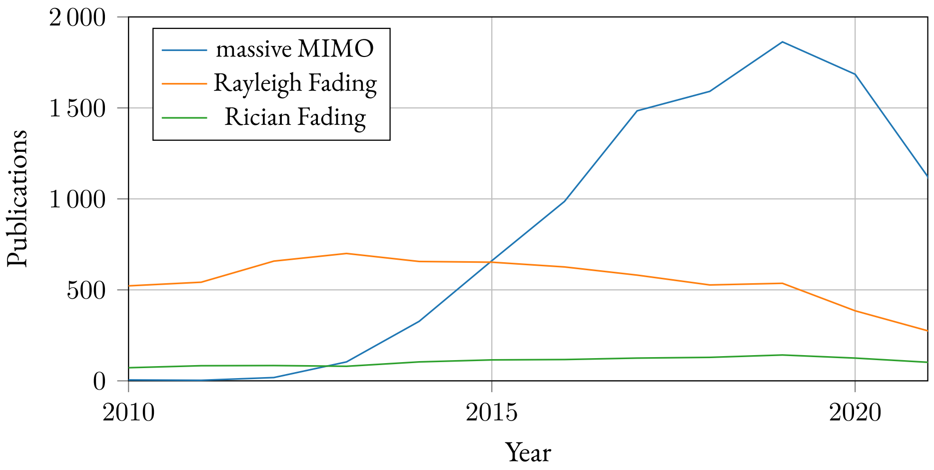

Figure 2.1: Number of publications per year according to the Web of Science Core Collection for the specified search term (query date 2021-11-17).

An alternative solution is based on enhanced prediction methods at the BS. Propagation paths are extrapolated, with high resolution methods, from uplink channel estimates to predict the downlink [26]. Hence, CSI feedback can be avoided. According to the authors, the penalty is between 1 dB to 3 dB for a well calibrated BS and favourable propagation.

There has been an attempt to standardise requirements for a *massive MIMO cellular network* in a more recent summary from 2020 [8]. The network should have:

- at least two synchronous TDD cells,
- a BS with at least 64 antenna elements and digital transceivers per element,
- at least 8 users per cell with linear combining and precoding to exploit the spatial properties of the channel and
- more than one BS antenna per active user.

This definition is in line with the original description of massive MIMO [16] and highlights where differences between theoretical systems and practical implementations might sacrifice performance. Furthermore, the authors indicate that full consideration of spatial correlation is a necessity for the development of the field.

In 2019 it was declared that massive MIMO is a mature technology [18]. The first commercial actors had started selling their BSs equipped with LSAS. The authors identified 5 promising directions for the research community:

- extremely large aperture arrays (ELAA)
- holographic massive MIMO,
- six-dimensional positioning,
- large-scale MIMO radar and
- intelligent massive MIMO.

The proposed research directions cover recent developments in massive MIMO and will be outlined in the remainder of the section.

The ELAA regime describes systems beyond LSAS size. An ELAA has larger physical extents and/or an increased number of array elements to ensure spatial non-stationarity of the radio channel. The array can be envisioned as e.g. a complete building facade with many antennas, distributed systems [27] or cell-free massive MIMO [28], where the network side array elements are distributed freely throughout a region. In cell-free massive MIMO is a user only communicating with elements providing strong radio channels, which should keep the number of interacting elements low, but requires practical backhaul coordination strategies. The wide spatial distribution of antenna elements is the core difference to LSAS, opening up to mitigate large-scale fading effects arising from shadowing or blockage. The large extent of the antenna array requires additionally that the far-field and near-field aspects are taken into account. There is a difference between the far-field of an antenna element and the whole array. The *Björnson distance* has been introduced for a hypothetical uniform rectangular array (URA) with square aperture elements [29], to describe the distance where amplitude variations originating from a spherical wave become negligible over the array. The Fraunhofer array distance describes the point where the phase variations over the array disappear and is in general larger than the Björnson distance. It is possible to constructively superimpose the incoming wave by correcting for the phase in the region between Björnson and Fraunhofer array distance, since it is locally plane for each antenna element.

The holographic massive MIMO concept considers the integration of a large number of antenna elements into a limited spatially continuous aperture. This approach deviates from the classic $\lambda/2$ antenna array design and needs to embrace mutual coupling between elements. Especially meta-materials might be the enabler to build systems which are called large intelligent surfaces or reconfigurable intelligent surface (RIS). A recent survey [30] sees potential to improve the SNR with RIS even in the sub-10 GHz regime, but they point out that supporting measurements are lacking.

Six-dimensional positioning is supposed to provide the orientation in addition to an accurate location ($<$ 10 m) of a user in space. With LSASs and enough bandwidth, direct and reflected propagation paths can be resolved to provide additional spatial resolution in a cell. Moreover, higher frequency bands require more directional antenna elements and potentially arrays at the user in addition. Hence, the orientation of a terminal can be derived from precise angular resolution. Using a massive MIMO BS for joint communication and sensing opens up for radar applications [31].

The last research direction is combining the developments in artificial intelligence (AI) and machine learning (ML) with signal processing challenges related to LSAS. The term of intelligent massive MIMO has been coined. Especially the large amount of data arising from observing the channel with many antenna elements over larger bandwidths provides a rich information source. A possible application is channel charting [32], where the high-dimensional CSI is processed in a way that generates two-dimensional channel charts (a pseudo-map that is supposed to preserve the local spatial geometry). The approach can use processed CSI from multiple BS too [33]. The channel chart might allow to locate users relative to each other, opening up for geometrically motivated scheduling to ensure favourable propagation. Furthermore, ML methods can be used to replace estimators in specific signal processing algorithms. E.g. successive interference cancellation (SIC) can integrate a data-driven learning algorithm [34] to gain robustness against non-linearities of channels and noise corruption.

2.1 Channel Models for Massive MIMO

The fading distributions in chapter 1 are building blocks of stochastic channel models and provide one abstraction of real-world wave propagation. This thesis makes heavy use of them to model the individual links between a user and antenna elements of a massive MIMO BS. In general, channel models can be divided into three general categories:

- stochastic channel models,
- deterministic channel models and
- recorded CSI.

All those models have been explored to describe SISO systems, where one end of the link is potentially mobile. For massive MIMO those models can be constructed as well, dependent on the system aspect that is of most interest.

Stochastic models, containing the most prominent Rayleigh and Rician fading channel, are not location-specific. Originally, the Rician distribution was described in the 1940s to consider a sinusoidal component in addition to random noise [35]. It can be used to describe a deterministic plane wave in a mixture of a large number of other plane waves that capture the diffuse part of the radio propagation. If the deterministic component disappears, then Rayleigh fading is the model of choice. Both fading models are still in active use, which can be seen from their relevance in current publications (see Fig. 2.1). They are used in this thesis due to their versatility and compact mathematical description.

Geometry-based stochastic channel models (GSCMs) are used where spatial consistency is required. Scatterers and clusters are stochastically generated to produce channel coefficients with the statistics of a specific environment type. The

COST 2100 MIMO channel model [36] has been extended by considering visibility regions at the BS [37], elevation angles, polarisation and closely spaced users [38] and other aspects to the COST 2100 model with massive MIMO extensions [39]. In comparison to measurement data, channel hardening is more accurately described with this model than iid complex normal models [40]. Additionally, there are attempts to extend the Quasi Deterministic Radio Channel Generator (QuaDRiGa) [41] (an extension of the WINNER channel models) to account for aspects of massive MIMO [42].

Deterministic channel models are based on evaluations of Maxwell equation approximations (e.g. by ray tracing or ray bouncing) to calculate channel coefficients. This approach requires an accurate description of the propagation environment (e.g. geometry and electro-magnetic properties of the materials) to generate site-specific models. A ray-based channel model has been used to analyse e.g. a dense urban scenario [43].

Recorded CSI is the basis for the last category of channel models. Physical observations of radio waves are used to investigate site-specific propagation. Large amounts of data have to be handled, whereas stochastic models require only few parameters and random processes to generate channels. Especially for test cases and channel emulation is a recorded CSI model valuable.

In summary, channel models vary in accuracy, complexity and site-specificity. Pure stochastic models tend to have lower accuracy, lower complexity and no site-specificity. Recorded CSI has higher accuracy, high data acquisition complexity and no generality. The development process of new or adjusted models can be seen as a data reduction and generalisation process. It starts with observing physical propagation environments and ends with a few parameters that capture the essence of a class of propagation environments.

2.2 Measurement Datasets

Every theory and every model should be evaluated against real-world measurements. Either to validate the theory, to check the accuracy of the model or to analyse which model assumptions have been violated. The latter is a necessary step to align models with the evolution of practical implementations. From an engineering perspective, it is important to know which aspects of the physical world can be neglected without compromising some uncertainty requirement. There is a trade-off between accuracy, applicability and complexity of models.

One important aspect of massive MIMO is the parallelism of the observations at the BS. Therefore, to acquire relevant CSI, the channel response should be collected in a synchronised parallel manner. Virtual massive MIMO measurements, where sequential SISO observations are used to characterise the channel, neglect that aspect and are therefore mainly relevant for low (environmental) mobility cases. The effort of parallel data collection is more complicated and requires additional hardware and personnel. Fortunately for the research community, multiple datasets from different groups have been made publicly available during the last few years. The following non-exhaustive list shows some available massive MIMO sub-6 GHz datasets:

- indoor and outdoor datasets[1] (UHF, 2.4 GHz, 5 GHz, up to 104 antenna elements, up to 8 users) [44]
- indoor-outdoor dataset[2] (2.6 GHz, co-located vs distributed antenna array, up to 64 antenna elements, up to 12 users) [45]
- outdoor dataset[3] (2.6 GHz, two distributed 32 antenna arrays, sequential placement of user pairs) [46]
- indoor dataset[4] (2.6 GHz, two distributed 32 antenna arrays, sequential placement of user pairs) [47]
- dense indoor datasets[5] (2.6 GHz, uniform linear array (ULA), URA and distributed antenna arrays, sequential users) [48]–[50]

---

[1] `https://renew.rice.edu/datasets.html`

[2] `https://github.com/networkedsystems/MaMIMO_IndoorOutdoorExperiment`

[3] `https://github.com/networkedsystems/MaMIMO_outdoor_expermient-`

[4] `https://github.com/networkedsystems/MaMIMO_indoor`

[5] `https://homes.esat.kuleuven.be/~sdebast/measurements/measurements_index.html`

- outdoor dataset[6] (ULA, URA, 860 MHz) [51]

In addition, we have collected indoor CSI in December 2017 with a 64 antenna elements array in four frequency bands between 1 GHz and 5 GHz. This dataset has been the basis for the work in [J1], [R1] focusing on the comparison of the four frequency bands. The work in [C3] is using indoor datasets for 2.4 GHz and 5 GHz from Rice University [44] for its case study. Moreover, we have used the dense datasets from [48]–[50] which provide user positions on a 5 mm grid to get a better understanding of spatial properties of real massive MIMO channels.

---

[6] `https://dramco.be/massive-mimo/measurement-selector/#Sub-GHz`

3 Thesis Overview and Key Contributions

> Gedanken ohne Inhalt sind leer,
> Anschauungen ohne Begriffe sind blind.
> (Thoughts without content are empty,
> intuitions without concepts are blind.)
>
> Immanuel Kant

The following chapter gives an overview over the research work that we have performed at the Norwegian University of Science and Technology (NTNU) between 2017 and 2021. Studying the foundations of massive MIMO leads to quite a few questions if you are having a background in antennas, propagation and random arrays. The squared coefficient of variation as measure of channel hardening might be practical to determine the asymptotic behaviour of massive MIMO, but for finite system size and design trade-offs other measures might be more practical. Hence, our first central question is: *How to characterise channel hardening?*. The finite aspect of practical systems leads naturally to a second general question: *How many antenna elements are sensible?*. A third general question arises from the user-centric perspective: *What are the statistics of the effective channel?*.

There is no definite answer to any of the questions besides a cautious *it depends*. Our publications provide ways to tackle those questions for some cases and can be grouped into three parts related to LSAS for massive MIMO:

1. measurements,
2. system practicalities
3. and theoretical considerations.

The first publication [J1] provides results of an indoor measurement campaign with the Reconfigurable Radio Network Platform (ReRaNP). The measured data indicates similar behaviour of the radio channel between 1 GHz and 5 GHz. Even in the relative simple environment did some users experience a loss of over-the-air synchronisation for some positions. This observation gave rise to the analysis in [C2], describing the achievable synchronisation gain and the implications of a growing number of antenna elements at the BS. Other groups have used cables to synchronise users and BS in some measurement campaigns to circumvent the issue.

Furthermore, [J1] paved the path towards research on system practicalities and led to the analysis of a π scheme [C1], which is realisable with reasonable excess power for LSAS. Moreover, fading margins were derived in [C3] to describe the effect of channel hardening from a system perspective, in contrast to the commonly used squared coefficient of variation [19, Eqn. (2.17)] of the effective channel gain.

In parallel to covering some system practicalities of massive MIMO in our publications, we worked on the commission of ReRaNP. The goal was the usage of 128 antenna elements as BS array and simultaneous CSI acquisition to investigate industrial IoT scenarios. Multiple challenges along the way delayed the deployment of the testbed. Small antenna elements and low-loss coaxial cables provide a challenge on the mechanical stability of their connection. and proper verification of simultaneous data acquisition, handling a large complex system with little personell is tedious. The final factor preventing in-house measurements was the outbreak of the coronavirus disease, which stopped the planned experimental work completely. Fortunately, we changed the direction of the thesis work already in summer 2020 even without knowing how the pandemic would evolve. Moreover, more research groups have started to make their measurement data available for external analysis. Hence, theoretical work can be tested against real world date without conducting measurements locally.

The more theoretical orientation resulted in a description of local diversity [C4], a measure to describe the robustness of radio links requiring ultra-reliability. Additionally, we worked on the statistics of correlated Rician fading in [J2], to provide a general description of the effective channel gain. The last manuscript was born from our observations in [C3], [R1], that none of the measurements showed performance anywhere close to the diversity predicted by a number of uncorrelated taps times the number of antenna elements. We had used correlation as a potential source of performance degradation as argument and needed a framework that can incorporate the complexity of real world systems (non-isotropic antennas, random antenna positions and orientations, non-omni-directional propagation) into a Rician fading environment, providing a compact and clear tool to analyse scenarios beyond uncorrelated models.

In the following, the three overarching questions are discussed in the light of the results from [J1], [J2], [C1], [C2], [C3], [C4], followed by individual summaries of the manuscripts of this thesis. The chapter concludes with potential future work and condensed answers of the central questions for considered cases.

3.1 How to characterise channel hardening?

As introduced in subsection 1.5.1, channel hardening is a property of the effective channel, which becomes more deterministic the more antennas a BS is equipped with. Ultimately, small-scale fading can be mitigated in a radio propagation environment providing enough spatial degrees of freedom. This qualitative description needs to be translated into some quantitative measure to be useful for performance evaluation and design of BSs. The common squared coefficient of variation as figure of merit has the downside that it is hard to put into context of a link budget. Furthermore, channel hardening provides no binary decision boundary, since a fully deterministic effective channel only arises asymptotically.

In Eqn. (7.1) [C3] we introduced a fading margin, which is based on the inverse CDF $Q(p)$ of the effective channel for probability p:

$$F_M(p) = 10\log_{10}\left(\frac{Q(0.5)}{Q(p)}\right). \tag{3.1}$$

This measure is invariant to the array gain because it is normalised by the median of distribution. It describes the amount of excess power needed to move the outage probability from 50 % to the target probability. Ultimate channel hardening would be achieved, if all outage probabilities result in a fading margin of 0 dB, i.e. the effective channel does not suffer from small-scale fading. The measure is well suited to give insights into the trade-off between BS antenna array size and excess power to counteract the effective channel gain fluctuations.

For example, a single antenna link at an outage probability of 10^{-3} has a fading margin of 28.4 dB. For 8 uncorrelated antennas is the fading margin reduced to 5.9 dB and 32 antenna elements require 2.6 dB excess power to close the gap. A squared coefficient of variation of 10^{-2} (an ad-hoc sufficient condition for channel hardening in [19]) would relate to a fading margin of 1.4 dB at an outage probability of 10^{-3}. The fading margin is a local measure of channel hardening with respect to the CDF, since it is evaluated at a specific outage probability.

In addition to the fading margin, we have introduced the local diversity $\mathcal{D}(\mathcal{Q})$ of the effective channel power gain $\mathcal{Q} = |\mathcal{H}|^2$ in Eqn. (8.8) [C4]. This measure relates channel hardening to the slope of the effective channel CDF:

$$\mathcal{D}(\mathcal{Q}) = \frac{d}{d10^{\mathcal{Q}/10}} 10\log_{10}\left(F(\mathcal{Q})\right) = \mathcal{Q}\frac{f(\mathcal{Q})}{F(\mathcal{Q})}, \tag{3.2}$$

as a local measure related to an outage probability. The derivative is scaled such that a local diversity of one coincides with a slope of 10 dB per decade outage probability, which is the slope of a single degree of freedom Rayleigh fading channel. For $\mathcal{Q} \to 0$ converges the local diversity to the classic diversity. The local diversity can be plotted as function of the outage probability to highlight that the classic diversity is misleading for LSAS. Low tail approximations of the effective channel CDF do not describe the behaviour in the operational regime of a BS in the ultra-reliability (UR)-relevant region. The local diversity as measure of channel hardening provides a connection to physical degrees of freedom.

3.2 How many antenna elements are sensible?

After exposure to the early work on massive MIMO, we have always wondered where the sweet spot for the number of antenna elements is. In the following discussion, an antenna element is synonymous with a full transceiver chain.[1] The general trade-off is the exchange of some system performance improvement for an increasing number of antenna elements (hardware cost).

Extremely large aperture arrays are explored as potential extension to massive MIMO with the number of antenna elements growing beyond 1000 elements [18], to exploit the spatial non-stationarity of the radio propagation environment. At the time of writing, these numbers of synchronised antenna elements are purely theoretical. Implementation challenges for extremely large aperture arrays are related to synchronisation, joint processing, mechanical properties and energy budget. In the adjacent field of radio astronomy is the Square Kilometre Array (SKA), an extremely large radio telescope, comparable to a receive only wide-band BS. They use random phased arrays consisting of 256 antenna elements [A5] and use multiple stations to distribute over a quarter million of antenna elements.

Returning to cellular networks, is it worthwhile to build such large installations or is it a wasteful use of resources? We have been considering the single user performance throughout our contributions and find that it is not worthwhile to use more than 32 antenna elements per user due to diminishing returns. Furthermore, not all 32 elements contribute equally to the system performance.

The diminishing returns for a growing number of antennas in our indoor measurements [J1] have not been evaluated explicitly. Nonetheless, inspection of Fig. 4.8 shows that the interquartile range (IQR) of the normalised effective power for 1, 4, 16 and 64 antenna elements is about 12 dB, 7 dB, 4 dB and less than 2 dB, respectively. Furthermore, the reduction of the effective delay spread (temporal focusing in the effective channel) in Fig. 4.10 is getting smaller for larger number of antenna elements. Already 16 antenna elements are enough to confine most of the realisations to a single delay bin. Additionally, the power variations per antenna element have almost converged for the TR and π strategy for 16 antenna elements (see Fig. 5.1) [C1], since the realisations of the π normalisation are close to an expectation of $\sqrt{M}$. The empirical fading margins at an outage probability

---

[1] Ericsson is marketing BS solutions with a variable number of transmitter and receiver chains being connected to a potentially larger number of antenna elements [52].

of 10^{-3} show small improvements beyond 32 antenna elements in the narrow- as well as wide-band case (see Tab. 7.2) [C3].

All observations and theoretical discussions in this thesis indicate that a single user is well served with 16 to 32 antenna elements. Additional elements, at least in compact arrays, provide little improvements in combating small-scale fading with channel hardening. Considering the gain gap between the synchronisation gain and the user-centric gain in addition [C2], shows that smaller BS are preferable, to avoid complex beam sweeping strategies for full cell coverage.

3.3 What are the statistics of the effective channel?

We have based all our antenna element statistics on Rayleigh or Rician fading. This is a reasonable assumption for many radio propagation scenarios with varying deterministic and diffuse parts. The corresponding antenna element channel coefficient h can be described by a complex normal distribution. Different effective channels have been discussed for different purposes in this thesis, but all are based on combinations of the element coefficients from multiple antennas and/or delay taps. Antennas and delay taps can be seen as interchangable sources of diversity.

In [C1], we are introducing a *maximum diversity channel* which is based on L diversity branches in iid Rayleigh fading:

$$\boldsymbol{h} \sim \mathcal{CN}_L(0, c\mathbf{I}), \tag{3.3}$$

where c is some common scaling of the element distributions. This gives rise to the effective channel power gain following a Gamma distribution:

$$\mathcal{Q} = \|\boldsymbol{h}\|_2^2 \sim \Gamma(L, c). \tag{3.4}$$

The effective channel for the combined uplink in [C3] reuses the iid Rayleigh fading maximum diversity channel with the corresponding Gamma distribution.

In [C4] is the effective channel based on uncorrelated Rician fading, which requires a generalised or non-central Gamma distribution. The last contribution

[J2] handles correlated Rician fading, based on approximations of a complex Gaussian quadratic form (CGQF) to describe the distribution functions in a compact fashion. Moreover, we provide a physically motivated parametrisation of the mean and covariance of the complex normal random vector to describe the correlated diversity branch statistics.

The effective channel in [C2] is slightly different to the (non-central) Gamma type results, because the strongest synchronisation channel is of interest. The relevant statistic is found by comparison of effective channel gains for different precoding weights, resulting in multiple beams illuminating the radio channel. The best synchronisation gain, results from the beam that is closest to the target user channel. Therefore, it can be solved as a selection combing problem with order statistics [53], [54]. For iid Rayleigh fading and Fourier or Hadamard beam sweeping matrices, exponential distributions describe the channel illuminated by different beams. Choosing the strongest channel gives a CDF based on the L-th power of the CDF of the individual L beams.

As a summary, the flow chart in Fig. 3.1 shows an overview over the different relevant distributions arising from complex normal random vectors, highlighting which forms have been used in the different manuscripts.

3.4 Summaries of Included Papers

3.4.1 Paper J1

G. Ghiaasi, J. Abraham, E. Eide, and T. Ekman, "Effective Channel Hardening in an Indoor Multiband Scenario", *International Journal of Wireless Information Networks*, vol. 26, no. 4, Jul. 2019. DOI: `10.1007/s10776-019-00438-7`

This paper reports the results of the first measurement campaign conducted in December 2017 with ReRaNP, the NTNU massive MIMO testbed. CSI has been collected with a 64 antenna element BS from 40 user positions over four different 20 MHz frequency bands between 1 GHz and 5 GHz. The capabilities of the testbed are further described in the article.

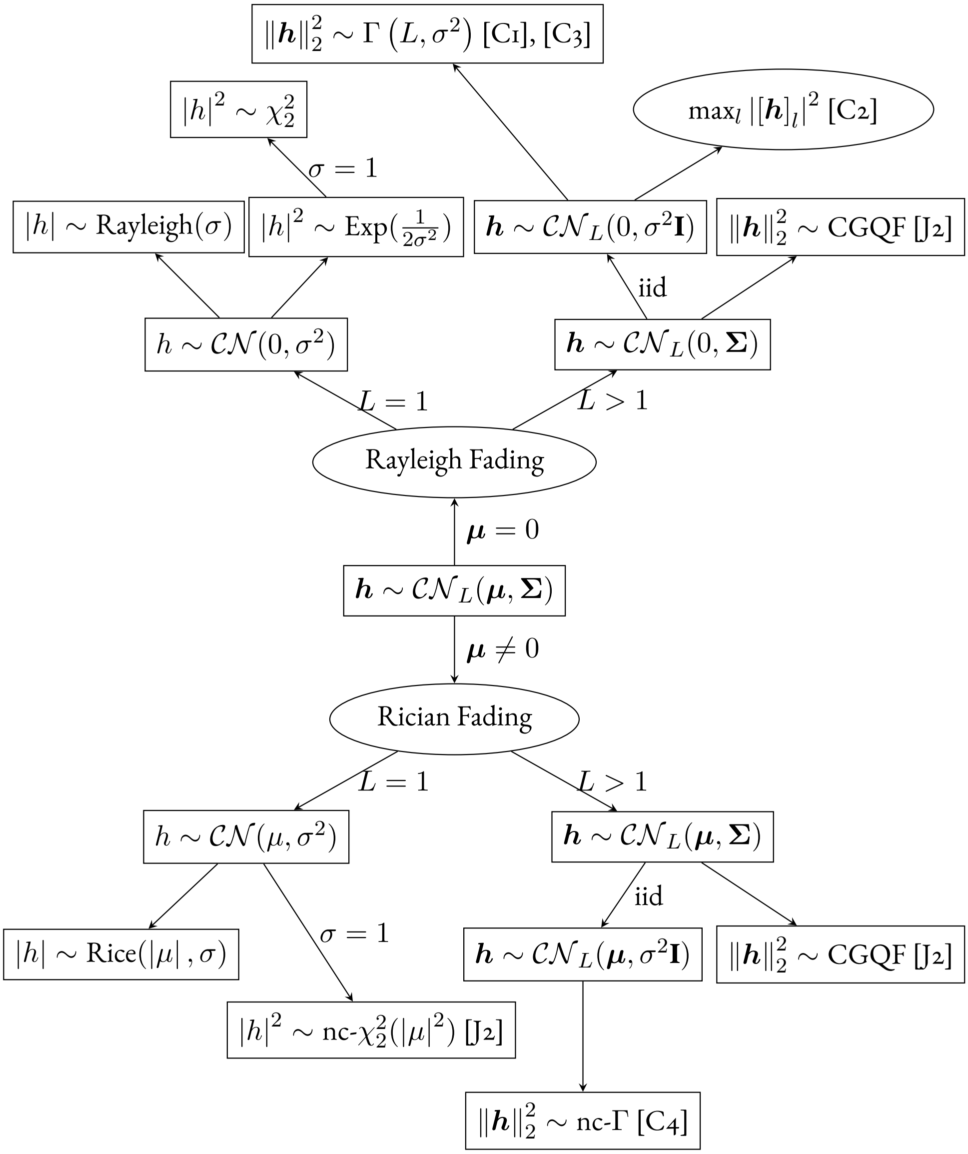

Figure 3.1: The relationship between a complex normal random vector $\boldsymbol{h}$ and different envelope as well as power distributions is shown in this flowchart. The distributions that have been used in the different manuscripts attached to this thesis are referenced.

The collected CSI captures an indoor scenario where antennas had been oriented so that NLOS conditions were excited. The power delay profiles (PDPs) are similar for all considered frequency bands and show that most power is confined in a 1 µs window. Furthermore, channel hardening was investigated with ECDFs of normalised subcarrier powers. They show a variability between −4 dB to 2 dB with 64 antenna elements, which is a huge improvement over the single antenna case.

A convenient side-effect of time-reversal precoding is temporal compression in the downlink. The delay spread of the effective channel is reduced to less than the duration of a single tap (50 ns for the system parameters) when all 64 antenna elements are used. This allows simple receivers without complex equalisation at the user side, which is convenient for WSN and IoT applications. The effective delay spread is reduced by increasing the number of BS antennas, but has diminishing returns.

In addition, we argue that coherence bandwidth is an unusable measure for the effective channel, by deriving a lower bound for a rectangular PDP (a maximum diversity example). The central tap of the effective channel PDP grows proportional to the number of antenna elements, whilst the remaining taps are roughly constant. This is based on coherent addition of the channel coefficient for the zero-delay tap and non-coherent addition for the rest of the effective PDP. Hence, for a growing number of BS antennas is the effective PDP converging towards a Dirac delta function, which can be seen as convergence towards flat-fading in the frequency domain. As a consequence, the frequency correlation function is bounded below by $\frac{M}{M+1}$ for the effective channel based on an environment with rectangular PDP.

3.4.2 Paper C1

J. Abraham and T. Ekman, “Power Inversion of the Massive MIMO Channel”, in *Proceedings of the 2019 Symposium on Information Theory and Signal Processing in the Benelux (SITB2019)*, arXiv:1905.07555, Gent, Belgium: Werkgemeenschap

Informatie- en Communicatietheorie (WIC) & IEEE Benelux Signal Processing Chapter, May 2019, pp. 3–7

This paper considers the behaviour of the effective downlink channel in the delay domain for WSNs and sensor nodes with a single tap receiver. Time reversal is applied as precoder and different normalisation strategies are introduced. They influence the signal fluctuation at the wireless sensor. In addition, the output power at each BS antenna element and the sum output power of the BS are affected. The former is of interest for the system designer and the latter is of interest from a regulatory perspective. Channel hardening reduces the effect of small scale fading. Hence, the necessary excess power to achieve power inversion is falling into a reasonable range and we quantify it. With perfect CSI, small scale fading could be completely eliminated.

To analyse the three different powers, we model the limiting maximum diversity case by using iid Rayleigh distributed channel coefficients for all delay taps at each antenna element. This choice describes a rectangular PDP observed with an uncorrelated BS antenna array. The precoder weights follow the TR principle, using the reversed and complex conjugated tapped delay line channel. Three different normalisation strategies are presented:

(a) classic TR (keeping the BS output power fixed),
(b) power inversion (PI) (keeping the received power at the node fixed)
(c) and distributed time reversal (DTR).

The latter strategy normalises the precoding weights based on statistical information and avoids continuous feedback of channel estimates, which the two former options would require.

Importantly, the antenna element output power converges to the distribution of the DTR strategy for a growing number of antennas, a Gamma distribution parameterised by the number of taps. PI fixes the received power at the user by using more transmit power at the antenna elements to compensate for weak channel realisations. Under the iid Rayleigh fading assumption, some of the powers (see Tab. 3.1) can be described with Gamma distributions.

Table 3.1: Analytical distributions are available for some powers in dependence of the normalisation scheme.

Normalisation	Element Power	BS Power	Recieved Power
Classic TR		const.	$\sim \Gamma(MN, \frac{1}{MN})$
Distributed TR	$\sim \Gamma(N, \frac{1}{N})$	$\sim \Gamma(MN, \frac{1}{MN})$	$\sim \Gamma^2(MN, \frac{1}{MN})$
Power Inversion			const.

E.g., a BS with 16 antenna elements and a rich rectangular four tap channel has ideally 64 degrees of freedom that provide channel hardening. Allowing for 0.5 dB of excess power on each antenna element in 10^{-4} cases allows for power inversion. This results in an excess sum power of 2.2 dB in 10^{-4} cases for the BS.

In summary, the power inversion strategy allows to eliminate small scale fading in exchange for some excess power at the BS. A more robust downlink, only depending on large scale fading to WSN nodes, can be provided.

3.4.3 Paper C2

J. Abraham and T. Ekman, "Achievable Synchronisation Gain In Uncalibrated Large Scale Antenna Systems", in *2020 14th European Conference on Antennas and Propagation (EuCAP)*, Mar. 2020, pp. 1–5. DOI: `10.23919/EuCAP48036.2020.9136063`

This paper examines the initial synchronisation of a user with the BS before channel reciprocity can be exploited through massive MIMO. The *user directed gain* is bigger than the *synchronisation gain*, leaving a gain gap that should be considered in the system design. This gap influences the cell coverage area for initial access to the network, where timing and configuration information have to be acquired by the user. This issue can be reduced by beam sweeping, an open-loop beam forming strategy demonstrated with the Argos testbed [55]. Other measurement campaigns avoided the issue by using cabled synchronisation of the user terminals (e.g. [17]).

We analyse the gain gap of different beam sweeping strategies analytically and provide closed form solutions for uncorrelated Rayleigh fading. The Rician case is more involved and was analysed with representative simulations to allow a comparison. The gain gap is calculated based on the Hermitian angles [20] between the beams provided by a beam sweeping matrix and a random flat fading channel. Order statistics [53] provide the means to find the distribution for the best beams with respect to the fading channel.

We have restricted our analysis to an ULA with $\lambda/2$ spacing and three representative orthogonal beam sweeping matrices:

(a) the identity matrix (sweeping through each BS antenna element individually),
(b) the Fourier matrix (array factor achieving beams)
(c) and the Hadamard matrix (split beams).

If the array is uncalibrated, then each signal branch is subject to an additional random phase. In this case, the actual choice of the beam sweeping matrix does not matter and the system behaves as if it was Rayleigh fading independently of a specular component being present. This is due to the random mixing of the specular component, giving non-coherent addition.

A Fourier matrix is advantageous in Rician fading in the calibrated case, since it achieves the full array factor. The orthogonality requirement of the beam sweeping matrix can be relaxed, which allows to scan more directions with the full array gain. A trade-off between sweep duration and probability that the beam is close to the channel vector of an actual user can be achieved.

The behaviour for a growing number of base station antennas is shown for the median gain gap and synchronisation gain in Fig. 3.2. There are diminishing returns for the synchronisation gain if the BS output power is fixed. A 1000 antenna element BS achieves relative to a single antenna BS only 8.6 dB sync gain with an orthogonal beam sweeping strategy. The gain gap is −21.4 dB with respect to the maximum array factor gain.

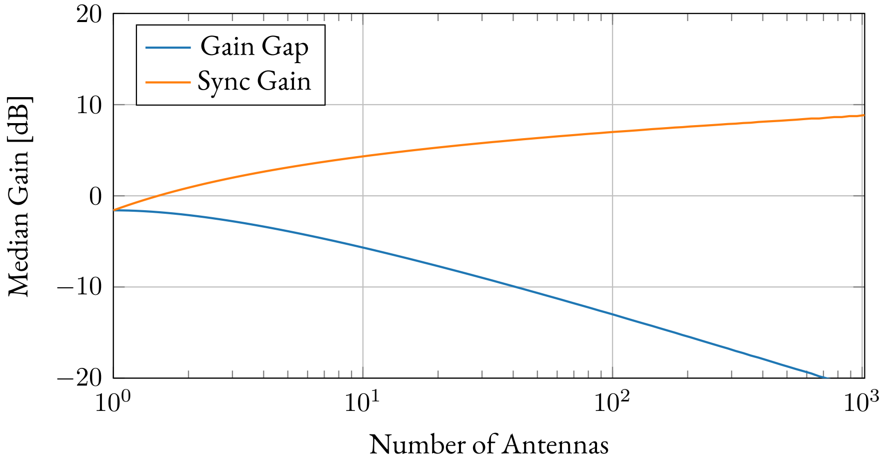

Figure 3.2: The median gain gap and sync gain are shown for a growing number of antenna elements suspect to Rayleigh fading and the BS output power is normalised to unity. The sync gain is relative to a single antenna BS and demonstrates that even 1000 antenna elements do provide less than 10 dB extra gain. The gain gap shows that the sync signal is more than 20 dB weaker than the user directed gain for the same BS and orthogonal beam sweeping.

To ensure proper cell coverage of synchronisation signals, broadcast capabilities of LSAS have to be considered. A straightforward orthogonal beam sweeping strategy can reduce the penalty of lacking CSI. More advanced synchronisation strategies have to be developed, if ELAA are to be deployed successfully.

3.4.4 Paper C3

J. Abraham and T. Ekman, “Fading Margins for Large-Scale Antenna Systems”, in *ICC 2021 - IEEE International Conference on Communications*, Montreal, QC, Canada: IEEE, Jun. 2021, pp. 1–5. DOI: `10.1109/ICC42927.2021.9500328`. arXiv: `2102.09903`

This paper introduces a fading margin as a practical figure of merit for channel hardening at a specific outage probability. It gives the amount of extra BS power which is needed to move the outage probability from 50 % to the target outage probability. This measure gives better insight into the trade-offs from a system perspective than the more common squared coefficient of variation in Eqn. (1.23).

We reuse an uncorrelated maximum diversity Rayleigh channel and TR precoding to show the scaling of the fading margin under ideal conditions. E.g. 8 degrees of freedom give a fading margin of 5.9 dB and 24 degrees of freedom give a fading margin of 3.1 dB at an outage probability of 10^{-3}. Additionally, measurement data from Rice University [44] is used to study the empirical fading margin, comparing narrow- and wide-band systems for up to 93 antenna elements. Four datasets are evaluated to investigate the 2.4 GHz and 5 GHz band in LOS and NLOS conditions. For all datasets, using the full 20 MHz channel instead of a single subcarrier with 93 antenna elements provides less than 1.7 dB improvement of the fading margin at an outage probability of 10^{-3}. Even for a smaller subarray of 32 antenna elements is the difference between narrow- and wide-band operation small. The LOS 2.4 GHz dataset shows about 12 degrees of freedom for a BS with 93 antenna elements operating in a 20 MHz band.

The squared coefficient of variation is supposed to be below 10^{-2} to classify a radio channel as hard, which corresponds to 100 degrees of freedom. Hence, the outage probabilities 10^{-2}, 10^{-4} and 10^{-6} relate to the channel hardening threshold fading margins 1.1 dB, 1.7 dB and 2.2 dB, respectively. These margins have not been observed in the analysed datasets.

3.4.5 Paper C4

J. Abraham and T. Ekman, “Local Diversity and Ultra-Reliable Antenna Arrays”, in *2021 55th Asilomar Conference on Signals, Systems and Computers*, Nov. 2021. arXiv: `2108.00712`, submitted and presented

This paper considers URLLC and highlights that massive MIMO can provide improved link robustness due to channel hardening. The UR-relevant regime spans a range of outage probabilities from 10^{-9} to 10^{-5}. Reliable characterisation of a non-parametric ECDF at a certain outage probability requires about twice the order of observations with respect to the inverse of the outage probability. E.g. 10^{12} observations are needed for a reasonable accuracy at an outage of 10^{-6}. To ease the estimation burden, lower tail approximations have been proposed in the literature, to describe the behaviour of systems at low outage probabilities [56].

We demonstrate that lower tail approximations do not provide good insight into the system behaviour of LSAS both for Rayleigh and Rician fading. The local diversity is introduced to quantify the deviation from the lower tail. It is a measure proportional to the steepness of the effective channel gain CDF and converges to the classic diversity for outage probabilities going to zero. In short, the local diversity D quantifies the steepness of the CDF in $10/D$ dB per decade, e.g. a local diversity of 1 and 10 gives a steepness of 10 dB and 1 dB per decade outage probability.

A narrow-band uncorrelated Rician channel was used to derive compact expressions for the PDF, CDF and local diversity in terms of the complementary Marcum Q-function. This is used to show that the lower tail approximation overestimates the local diversity for situations with many antennas and low $\mathcal{K}$-factors. For situations with high $\mathcal{K}$-factors, the lower tail approximation underestimates the local diversity, which shows superelevation over a certain range. We provide a simple scenario to demonstrate that distributed smaller BSs might provide better average channel gain with similar local diversity than a larger co-located BS.

The discussion closes with a general argument. The collection of statistics per antenna element might provide more accurate insight into UR-relevant statistics, than operating directly on the effective channel gain. This idea is based on the observation that the UR-relevant regime of the effective channel gain is mainly characterised by events with higher probability for the individual antenna elements. The downside is the necessity to actively consider the correlation in the LSAS to combine the element statistics properly.

3.4.6 Paper J2

J. Abraham, P. Ramírez-Espinosa, and T. Ekman, “Statistics of the Effective Massive MIMO Channel in Correlated Rician Fading”, *IEEE Open Journal of Antennas and Propagation*, vol. 3, pp. 238–248, Jan. 2022. DOI: `10.1109/OJAP.2022.3147015`. arXiv: `2112.06692`

This paper introduces a framework to describe a massive MIMO multi-tap Rician fading environment. The propagation from a user terminal is modelled as a complex normal random vector, where each element describes the channel gain for an antenna element in a delay tap. Correlation is considered by inclusion of the power angular spectrum (PAS), the antenna element pattern as well as antenna positions. This extends the common simplification of isotropic antenna elements, with plane waves coming from all directions. The influence of varying directivity and squinting angles between antenna elements with the same pattern on correlation coefficients is demonstrated.

We provide accurate approximations of the effective channel gain for the CDF, PDF and local diversity, based on a CGQF. The approximations have been improved over those found in the literature, to allow for a larger number of vector elements, so that LSAS can be described.

BSs with a ULA and a half-circle array are compared for different antenna element directivities to demonstrate the possibilities of the framework,. The usage of low directivity elements for BS with many antennas appears to be advantageous, since the array factor is steerable and the antenna element factors are fixed. The half-circle array BS provides a more even illumination of a region than the ULA, but has lower maximum gain due to the slight squint between antenna elements. Additionally, it captures less local diversity than the ULA, since fewer antenna elements contribute significantly to the effective channel.

The generality of the framework opens up for the evaluation of many different other scenarios, which can be quickly evaluated. The provided approximations allow handling of different BS geometries and varying antenna element designs to cover different use cases.

3.5 Future Work

As indicated in chapter 2, the field of massive MIMO has evolved quickly during the last few years and based on theoretical considerations, many promising concepts have been suggested. There is a need to explore those concepts with demonstrators and testbeds to find the challenges that practical implementations pose. Investigating the details might not be as prestigious as coming up with revolutionary ideas, but allows to transfer the evolutionary and revolutionary research ideas into reality. This is the challenging borderland on the interface between science and engineering.

Future work should investigate the link between the medium complexity GSCM and a simpler correlated complex normal random vector ($\mathcal{CN}$-RV) model. Especially for systems with many spatial branches is the effective channel less sensitive to variation of element channel coefficients. That means, estimation of all parameters of a GSCM might not be worth the effort to improve the model accuracy. The exploration of CGQF for large random vectors could allow to find a more compact representation of high-dimensional massive MIMO CSI. The decomposition of the effective channel in Eqn. (9.27) exposes the impact of eigenvalues of the spatial correlation structure, indicating that the eigenvalues and their distributions should be examined further.

Since the work in this thesis has been focusing on the single user performance, favourable propagation has been handled in an introductory fashion only. Work on distributions of the leakage coefficient can path the way to a framework describing the instantaneous interference in a massive MIMO system and should be considered in the future. Eventually, a stochastic description of the instantaneous SINR can help to capture the big picture for LSAS.

For ELAA is the distinction between large-scale and small-scale fading unclear. Each antenna element might belong to a different local area, which increases the need to handle distributions of the channel coefficient, including large-scale fading aspects. Due to a larger number of contributing elements, effective channel statistics might become tractable, considering that a central limit theorem for partially correlated element statistics could exist. Moreover, (finite) random matrix theory (RMT) [57]–[59] explores some promising ideas that might give the right tools to work with the statistics of ELAA.

3.6 Conclusion

This thesis provides methods for the analysis of finite massive MIMO systems. Channel hardening can be described user-centric with a fading margin, to allow link budget analysis. Moreover, the local diversity relates channel hardening to effective degrees of freedom under consideration of a target outage probability operation point. Furthermore, channel hardening allows π with reasonable amounts of excess power to compensate for the remaining small-scale fading.

A BS with 16 to 32 antenna elements can serve a single user properly, if the propagation environment provides enough degrees of freedom. More antenna elements have diminishing returns for channel hardening and require advanced strategies to overcome the gain gap between the synchronisation gain without available CSI and the user-directed gain with CSI.

The effective channel power gain statistics have closed-form approximations for correlated Rician fading, which simplify to exact expressions in the uncorrelated case. Additionally, synchronisation gains can be described with order statistics to analyse different beam sweeping strategies.

All provided methods of this thesis target massive MIMO aspects in real world deployments. Special focus has been given to performance trade-offs relevant for link budget considerations. Especially the correlation aware closed form approximations of the PDF and CDF of the effective channel gain can give detailed insight into the impact of base station design on the SNR distribution for single users.

Part II

Publications

In the following, the manuscripts of two journal publications and four conference publications are reproduced from the original LaTeX-sources to follow the typography of the whole thesis. Minor modifications and improvements, where necessary, are listed in front of each manuscript. Changes to text are further indicated with bars in page columns.

4 Paper J1: Effective Channel Hardening in an Indoor Multiband Scenario

Authors	G. Ghiaasi, J. Abraham, E. Eide and T. Ekman
Journal	International Journal of Wireless Information Networks
Date	July, 2019
Original-URL	`https://link.springer.com/article/10.1007%2Fs10776-019-00438-7`
DOI	10.1007/s10776-019-00438-7

Changenotes

- Notation
  - convolution symbol $*$ changed to $\star$
- hyphenation of large-scale and small-scale

4.1 Abstract

We evaluate channel hardening for a large-scale antenna system by means of indoor channel measurements over four frequency bands, 1.472 GHz, 2.6 GHz, 3.82 GHz and 4.16 GHz. NTNU's Reconfigurable Radio Network Platform has been used to record the channel estimates for 40 radio links to a 64 element array with wideband antennas in a rich scattering environment. We examine metrics for channel hardening, namely, the coherence bandwidth, the rms delay spread and the normalized effective subcarrier power, for the effective channel perceived by a single user after precoding and superposition in the downlink. We describe these metrics analytically and demonstrate them with measured data in order to characterize the rate of hardening of the effective channel as the number of antenna

elements at the base station increases. The metrics allow for direct insight into the benefits of channel hardening with respect to radio system requirements.

4.2 Introduction

Massive MIMO systems are envisioned as a key feature of the next generation of communication systems which provide large sum capacity as well as spectral and energy efficiency, while simultaneously serving multiple users. Some of the theoretical properties [22], [25], [60] have been empirically shown through recent measurement campaigns [61]–[63]. In these analyses, keeping the number of users 10 folds less than number of BS antennas is considered good practice.

The large-scale antenna systems are being investigated as contenders for WSNs to offer mass connectivity with high reliability in 5G paradigm. In these systems, a BS equipped with a large number of antennas serves a very large number of sensor nodes such as ships, automobiles, trains, engines and robots, which are categorically referred to as user equipments (UEs). As many of these applications are safety critical, the robustness of the wireless communication links is vital. Channel hardening could be exploited, in order to establish reliable links between BS and UEs. By definition, the channel hardens when by increasing the number of BS antennas, the deviation of the gain of the perceived channel at each UE decreases and the channel gain value becomes deterministic [64].

From a radio system perspective, the desirability of channel hardening at sensor nodes is twofold: The signals traveling from the BS to each single UE are precoded at the antenna elements and filtered by the physical channel and then will superpose and form what is referred to as effective channel. When the effective channel hardens, it is as if the propagation happened through a quasi-deterministic flat-fading equivalent channel by averaging out the small fading effects, as a result forming a reliable link from the BS to the UE. Considering channel hardening in the delay domain, complex equalization and estimation at the UE side can be avoided because the effective channel collapses to a single tap due to the delay dispersion being smaller then the delay tap resolution.

In [65], [66], the authors have looked at channel hardening for the subcarriers using MRC in the uplink (UL). The standard deviation is used to examine the dispersion of the channel. Alternatively, the work in [67] formulates the concept of an effective (equivalent) received channel at a single UE by using time-reversal precoding. Here, the measured channels between the UE and the BS are used to examine temporal focusing by using the delay spread and the strongest tap power distribution. In [68] the measured channels between a 128 antenna BS and 36 UEs have been used to evaluate the root mean square (rms) delay spread of the effective combined channel for three common linear precoding schemes.

In this paper, we refer to the perceived channel at a single user in the downlink (DL) as an *effective channel*. This is the channel formed by precoding, propagation and superposition of signals from each BS antenna element. A calibration of the transmitter and receiver chains at the BS is necessary, such that the reciprocity assumption holds [69].

Channel hardening is considered from two points of view: firstly, as a property that causes the effective channel transfer function (CTF) between the UE and the BS to become more deterministic, secondly as a property to focus the received signal in the delay domain as the number of BS antennas increases. We illustrate these properties in the effective channel in order to determine how many antennas are sufficient to achieve a certain level of channel hardening. This will allow for the remaining BS antennas to be considered as contributors to achieve a multi-user system by using the remaining degrees of freedom to orthogonalize the effective channels.

We base our analysis on a channel dependent precoding which weights the signal at the antenna elements and relies on exploiting channel reciprocity in the DL to form a matched filter combination when observed by the UE. The aim of the precoding is to guarantee the best average SNR at the UE under the assumption that the CSI of the channel is perfectly known and no co-channel interference exists.

We formulate the normalized effective subcarrier power in order to examine the flatness of the effective channel at the UE. Additionally, the coherence bandwidth as well as the effective delay spread are analyzed. All three metrics have been characterized with measurement data at 4 frequency bands: 1.472 GHz, 2.6 GHz, 3.82 GHz and 4.16 GHz. These constitute the commonly considered frequency range for 5G and WSN systems and highlight potential frequency dependencies.

This manuscript is organized as follows: in Section 4.3 the measurement campaign which was carried out in an indoor area with industrial profile forming a quasi-static scenario is reviewed. The acquired data corresponds to 40 spatial sample points characterizing UL channels to a 64 element array in the above-mentioned frequency bands. The details of this campaign are reported in [R1]. In Section 4.4, the concept of the effective channel is introduced and the measured channel data is used to analytically form the effective channels. The metrics of hardening are described and evaluated in section 4.5. We show that coherence bandwidth ceases to be a practical measure for effective channel evaluation. Lastly, the conclusions are presented in Section 4.6.

4.3 Measurement Description

The investigation reported in this paper is based on the measured data acquired during a campaign carried out at the NTNU in December 2017 using the ReRaNP. The details of the UEs and the BS including channel estimate acquisition are described in [R1].

4.3.1 Measurement Setup

For our BS, we used two modules of the NTNU massive MIMO testbed with 32 National Instruments (NI) USRP-2943R devices. Two RF chains exist in each Universal Software Radio Peripheral (USRP) unit, as a result we have 64 radio chains at the BS. These units are controlled by one CPU which is running the NI LabVIEW Communications MIMO Application Framework. They form a TDD system with a LTE-like physical layer with 20 MHz operational bandwidth [70]. To implement the UEs, the radio chains of 4 NI USRP-2953R units were

Table 4.1: Massive MIMO Testbed Parameters

Parameter	Value
# of BS antennas	64 used
# of UEs	8
Center Frequency	1.2 GHz to 6 GHz
Bandwidth of Operation	20 MHz
Baseband Sampling Rate	30.72 MS/s
Subcarrier Spacing	15 kHz
# of Subcarriers	1200
FFT size	2048
Frame Duration	10 ms
Subframe Duration	1 ms
Slot Duration	0.5 ms
TDD periodicity	1 ms

controled through NI LabVIEW Communications MIMO Application Framework in Mobile configuration. The key parameters of the system are summarized in Table 4.1.

The BS antenna array and UE are equipped with wide-band log-periodic dipole arrays (LPDAs) covering the frequency band between 1.3 GHz to 6.0 GHz. The linearly polarized LPDA element has been designed to provide a half power beam width (HPBW) of approximately 110° in the H-plane and 70° in the E-plane giving a directive gain of 6 dBi when used as a single element. Each UE is equipped with one LPDA antenna element in vertical polarization, whilst the BS is equipped with 4 subarrays each containing 32 LPDA elements in an equally spaced 4x8 rectangular configuration as illustrated in Fig. 4.1. The antennas in the arrays are mounted with an element spacing of 110 mm on a common ground plane. As shown in Fig. 4.1 the antenna elements have interleaved polarization such that each element has a neighbor with orthogonal polarization. This reduces the mutual coupling effects between the elements to a minimum, hence the effect on the input impedance and radiation pattern for the elements are minimized. 64

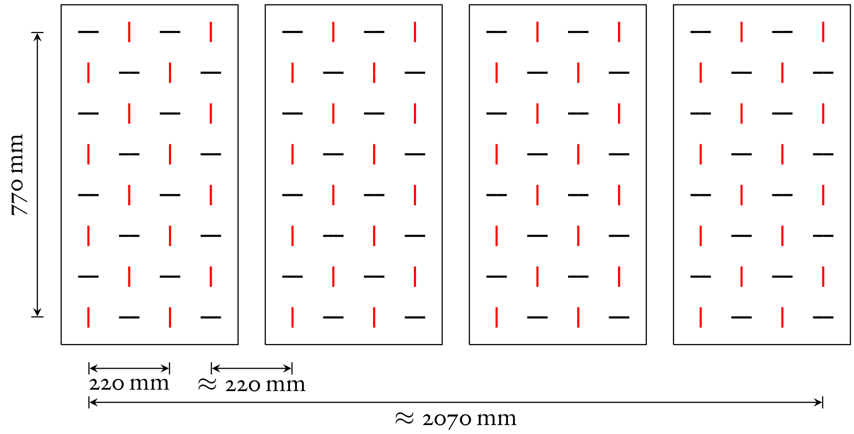

Figure 4.1: Frontal view of the antenna element configuration. Only vertically oriented elements were used for the reported measurement campaign.

vertically polarized elements were terminated at the BS whilst the other 64 horizontally polarized elements were left open. The configuration is depicted in Fig. 4.1.

4.3.2 Measurement Scenario

The measurement campaign was carried out in an indoor space with industrial profile in presence of glass, stone and metal reflecting surfaces. As depicted in Fig. 4.2 the BS was set up at the balcony at the end of the long hall while the cart containing the 8 UEs was placed on a wheeled cart at around 15 meter distance from the BS. The antennas of the UEs are positioned in a semi-circle configuration as shown in Fig. 4.3. They are directed away from the BS to suppress the LOS links and to ensure reflected links are more accentuated. The approximate distance between the UE cart and the main reflectors at the end of the hall is around 30 m. As shown in the campaign photos in Fig. 4.3 and Fig. 4.4, there exist many reflecting surfaces, such as concrete walls, window glasses, metal lamp posts and metal bars (at the end of the hallway) which form a rich scattering environment. For each frequency band, the UE cart was positioned along 5 premarked locations within 1 m diameter to obtain more sampling points of the environment.

4.3.3 Channel Estimate Acquisition

The system has M antennas on the BS side, K UEs and uses orthogonal frequency division multiplexing (OFDM) with 1200 usable subcarriers distributed over a 20 MHz band. Each user k transmits pilot symbols on a unique set of F subcarriers (in total 100 subcarriers for each UE) during the channel estimate acquisition to ensure orthogonality between the pilot symbols. These symbols are used to estimate the channel coefficient $G_{mk}[f]$, with m, k and f as BS antenna index, user index and subcarrier index, respectively, by a least-squares method.

A received symbol Y_{mf}^{BS} in the UL can be written as

$$Y_m^{\mathrm{BS}}[f] = \sum_K G_{mk}[f] X_k^{\mathrm{UE}}[f] + N_m[f] \tag{4.1}$$

where $X_k^{\mathrm{UE}}[f]$ is the transmit symbol and $N_m[f]$ the noise at the receiver. Furthermore, the channel coefficient is divided into a large-scale fading and shadowing factor ($\sqrt{\beta_k}$) and a small-scale fading factor $H_{mk}[f]$:

$$G_{mk}[f] = \sqrt{\beta_k} H_{mk}[f]. \tag{4.2}$$

If $G_{mk}[f]$ is distributed according to a complex normal variable with zero mean and variance β_k, that is $G_{mk}[f] \sim \mathcal{CN}(0, \beta_k)$), then $H_{mk}[f] \sim \mathcal{CN}(0, 1)$. The complex CTF coefficient $H_{mk}[f]$ is used in the rest of the manuscript to analyse properties of channel hardening. The delay domain representation is readily available via an inverse discrete Fourier transform (IDFT) along the frequency axis

$$h_{mk}[n] = \underset{f}{\mathrm{IDFT}} \left\{ H_{mk}[f] \right\} \tag{4.3}$$

where n denotes the delay bin. This representation corresponds directly to a tapped delay line.

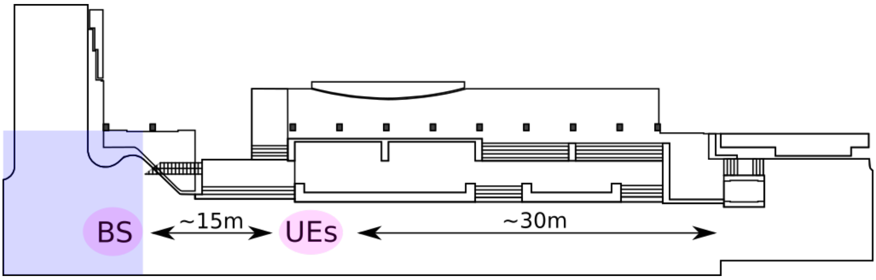

Figure 4.2: Top down sketch of the scenario. The base station (BS) is placed on a balcony indicated with blue color. The user equipments (UEs) were placed at a distance of approximately 15 m with antenna orientation away from the BS subarrays.

Figure 4.3: Positioning of the base station on the balcony and the user equipment cart. The antennas are pointing away form the balcony to illuminate non-line of sight links. Five physical locations in the black square were measured for each frequency band.

Figure 4.4: Overview of the measurement scenario from the base station balcony as seen by the antenna array.

4.3.4 Measurement Results

To represent the measured radio environment and to highlight the variations over the frequency range, we present one single CTF per frequency band in Fig. 4.5. Each CTF, normalized to its average power, demonstrates significant fading below −10 dB, as expected for a rich scattering environment.

Fig. 4.6 represents normalized power delay profiles for all measured SISO channels by averaging over the realizations for all UEs and BS antennas. The channel confines most of the power in a delay window of 1 µs. Furthermore, 5 to 6 multi path components (MPCs) are clearly resolved for the observation bandwidth of the user. The response outside of a ±1 µs window of the effective channel is considered to contain measurement noise and is therefore discarded. Additionally, artifacts of the IDFT at the delay border and noise contributions are hereby reduced.

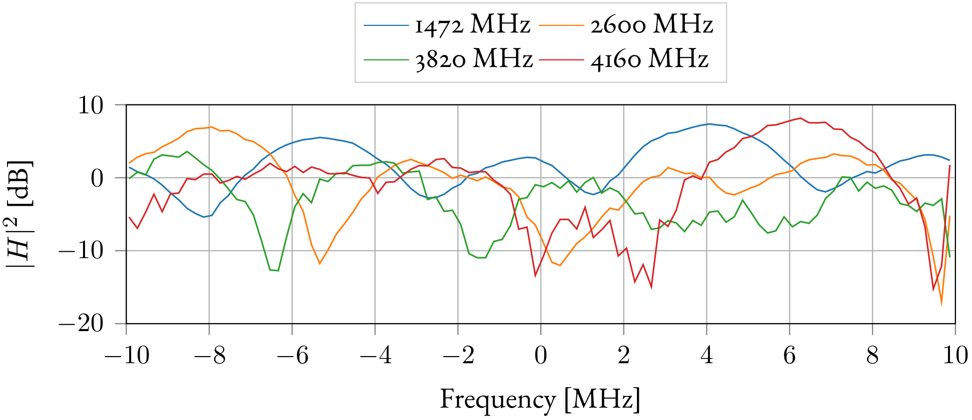

Figure 4.5: Selected transfer functions of uplink channels between a single user and a single base station antenna are shown. Some subcarriers experience severe fading of more then 10 dB.

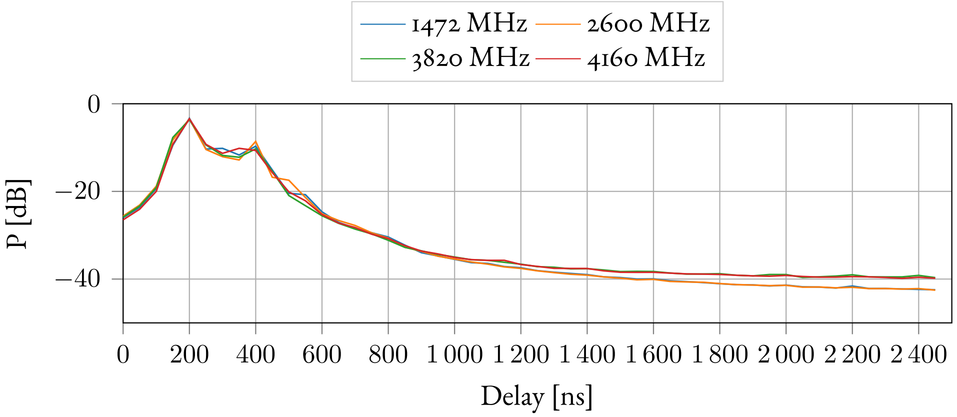

Figure 4.6: Power delay profiles for the four frequency bands are shown. They were estimated by averaging over all base station antennas, users and measurement locations in a small area. Observed differences between the frequency bands are small. Hence, the small-scale fading behaviour is not changing considerably between 1472 MHz and 4160 MHz in the reported scenario.

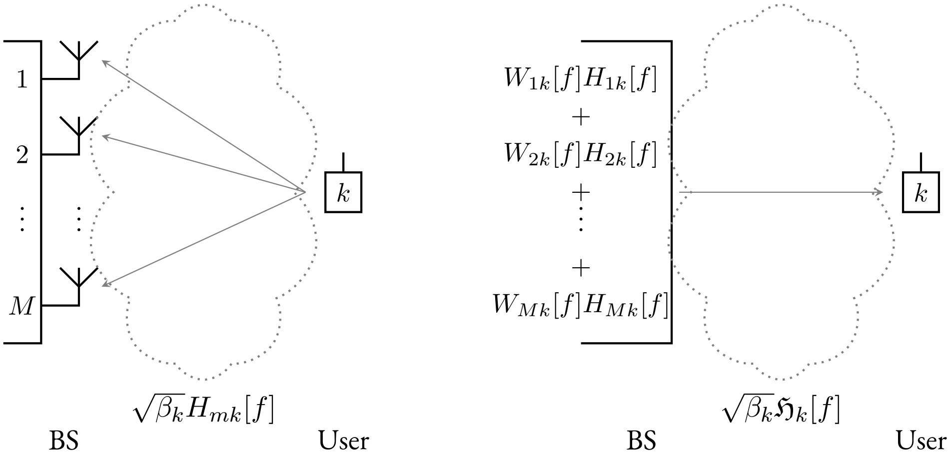

(a) Uplink Pilot Transmission

(b) Effective Downlink Channel

Figure 4.7: Conceptual massive MIMO TDD operation. Subfigure (a): Pilot signalling in the uplink to estimate $\mathfrak{H}_{mk}[f]$ at the base station. Subfigure (b): Precoded downlink transmission with superposition at the user, who experiences the effective channel.

4.4 Effective Channel Concept

In TDD massive MIMO systems, the UL channels between BS and UEs are estimated at the BS by using a set of orthogonal pilot symbols sent by each UE and received at each antenna element in the arrays, as depicted in Fig.4.7a. Given reciprocity holds for the transmitter and receiver chains in the coherence bandwidth of the system, these channel estimates denoted by $H_{mk}[f]$ are used to calculate the precoding weights at each antenna element. If no co-channel interference is assumed, the system can be considered as a multiple-input single-output (MISO) system and the *effective channel* perceived at the UE is formed by superposition of these individual channels. In other words, the UE, unaware of any beam forming or precoding, observes a DL SISO channel from the BS which is the *effective channel*.

As shown in Fig. 4.7b, from the UE's perspective, all the signals from the BS form an effective channel according to Eq. (4.4).

In our specific analysis, weighted sums of SISO CTF coefficients with freely chosen weights $W_{mk}[f]$ are used to form the effective channel CTF coefficients $\mathfrak{H}_k[f]$,

$$\mathfrak{H}_k[f] = \sum_M W_{mk}[f] H_{mk}[f]. \tag{4.4}$$

Therefore is the received signal at user k in the DL

$$\begin{aligned} Y_k^{\text{UE}}[f] =& \sqrt{\beta_k}\mathfrak{H}_k[f] X_k^{\text{BS}}[f] \\ &+ \sqrt{\beta_k} \sum_M H_{mk}[f] \sum_{l \neq k}^{K} W_{ml}[f] X_l^{\text{BS}}[f] + N_k[f], \end{aligned} \tag{4.5}$$

where $Y_k^{\text{UE}}[f]$ is the received DL signal at user k and the DL symbol to user k is $X_l^{\text{BS}}[f]$. The second term constitutes the multiuser interference and $N_k[f]$ is the additive noise at user k. To illustrate the properties of the effective channel we choose the weights to be the complex conjugate of the CTF coefficients with a normalization of $\sqrt{M}$ to impose an average power constraint

$$W_{mk}[f] = \frac{H_{mk}^*[f]}{\sqrt{M}}. \tag{4.6}$$

This differs from MRT,

$$W_{mk}^{MRT}[f] = \frac{H_{mk}^*[f]}{\sqrt{\sum_M |H_{mk}[f]|^2}} \tag{4.7}$$

where the normalization is an instantaneous power constraint over the array [10]. For large M the difference disappears as $\sum_M |H_{mk}[f]|^2 \approx ME\{|H_{mk}[f]|^2\} = M$ due to the self averaging property of the large array. The chosen normalization for the matched filtering does maximize the average SNR in the DL and simplifies the time domain analysis in Sections 4.5.1 and 4.5.2 as it directly transfers to time reversal precoding.

We take different subsets over the M base station antennas, in order to form several effective channels and use them to determine how the different metrics behave for increasing number of antennas in the following section.

4.5 Channel Hardening Metrics

In the frequency domain, channel hardening is regarded as flat fading of the effective CTF over a large bandwidth. In the delay domain the channel hardening implies that the strong contributions of the effective channel impulse response (CIR) are confined to a single delay tap, with reliable tap power for most realizations. Since the rms delay spread of the effective CIR determines the necessity for an equalizer in the UE design, with sufficient channel hardening, the UE receiver could be simplified. The next three subsections describe the figures of merit for characterizing channel hardening in both delay and frequency domains.

4.5.1 Power Variation of the Effective Channel

Characterizing power variations between different subcarriers of the effective channel is a metric to assess the flatness of the CTF over the observed bandwidth. To allow for comparison between BS antenna subsets with different cardinality, the subcarrier power needs to be normalized by the expectation of its distribution, namely $\mathbb{E}\{|\mathfrak{H}_k[f]|^2\} = M + 1$. The details of this derivation can be seen in Appendix 4.A. The normalized power in the frequency domain is then

$$\mathfrak{Q}_k[f] = \frac{|\mathfrak{H}_k[f]|^2}{M+1}. \tag{4.8}$$

The distribution of $\mathfrak{Q}_k[f]$ allows to characterize the power level fluctuations in the DL a narrow band receiver (RX) will see over the frequency range. Hence, it allows to draw conclusions about the amount of fading that the link budget needs to take into account.

Fig. 4.8 shows the empirical CDFs of $\mathfrak{Q}_k[f]$. The combinations are formed from 1, 4, 16 and 64 antenna elements over all measured frequency bands, with channels drawn from similar subsets of consecutive close antenna elements in the subarrays. The observed statistics of the channel is practically the same in the range

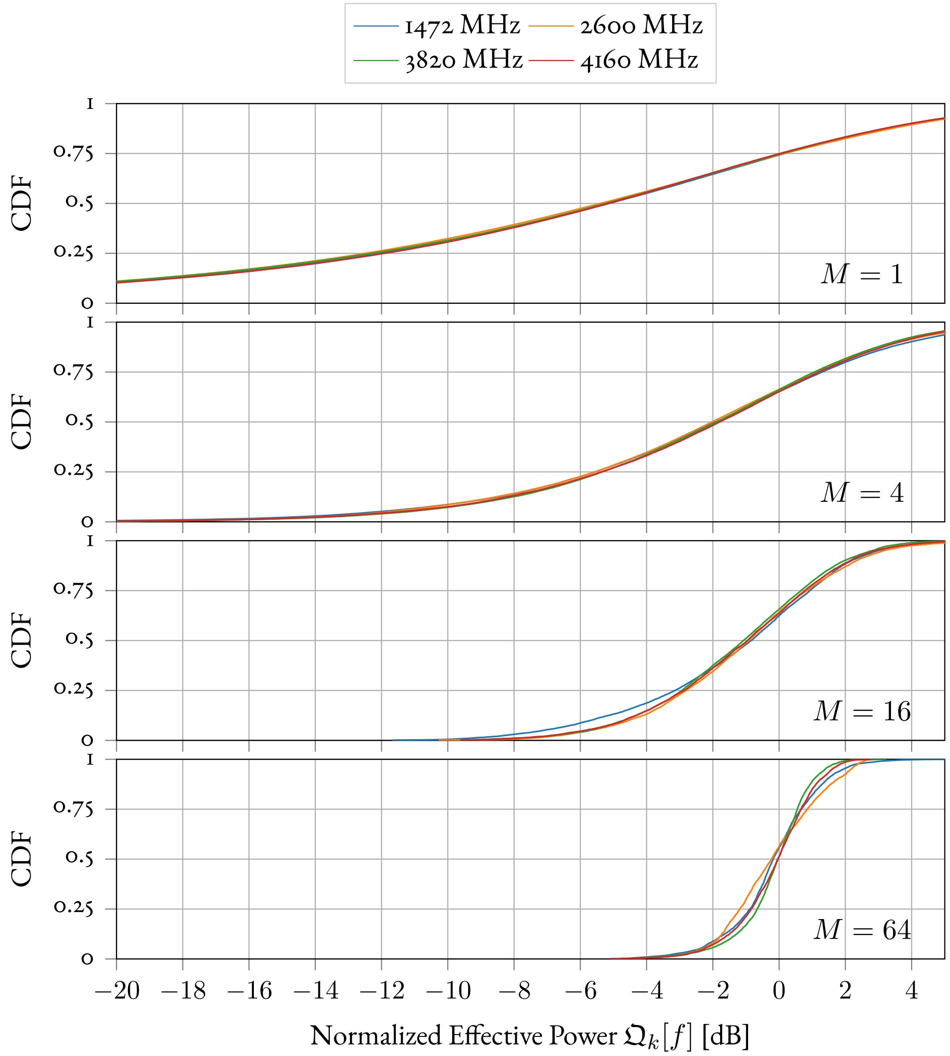

Figure 4.8: Empirical cumulative distribution functions for the normalized effective subcarrier power are shown. Fading has a lesser impact the higher the number of used BS antennas in the DL. Combination of 64 transmit signals at the receiver reduce the fading to less then 2 dB in 90 % of the realisations for all four frequency bands.

1.5 GHz to 4.2 GHz. Furthermore, the variation of $\mathfrak{Q}_k[f]$ reduces with increasing M. Considering the link budget, channel hardening would reduce the fading to 2 dB for 90 % of the observed effective channels with 64 antennas at the BS.

4.5.2 Effective PDP and Coherence Bandwidth

In this section, first we derive an analytical form for the effective PDP as a function of the PDP of the UL channels. Weights given by Eq. (4.6) are used to implement time reversal precoding in the DL. The frequency correlation is calculated as the Fourier transform of the effective PDP, then coherence bandwidth can be obtained as a metric for evaluation of the effective channel.

Under the assumption of independent and equally distributed channels for user k at all antenna elements, the channel can be described as complex normal distributed $h_{mk}[n] \sim \mathcal{CN}\left(0, p_k[n]\right)$ where $p_k[n] = \mathbb{E}\left\{|h_{mk}[n]|^2\right\}$ is the PDP for all the channels from user k to the array. With the normalization of path loss and large-scale fading the average channel gain is $\sum p_k[n] = 1$. The use of the weights from Eq. (4.6) in Eq. (4.4) corresponds to applying the matched filter in the time domain,

$$w_{mk}[n] = h_m^*[-n]/\sqrt{M}, \tag{4.9}$$

which is time-reversal precoding [67]. The normalization keeps the average output power from the array independent of M when these weights are used in a precoding filter. An instantaneous power constraint would give the normalization with $\sqrt{\sum_M \sum_n |h_{mk}[n]|^2}$, which for large M approximately is $\sqrt{M}$ as

$$\sum_M \sum_n |h_{mk}[n]|^2 \approx ME\{|h_{mk}[n]|^2\} = M \tag{4.10}$$

The effective channel in the delay domain becomes

$$\mathfrak{h}_k[n] = \sum_M w_{mk}[n] \star h_{mk}[n]. \tag{4.11}$$

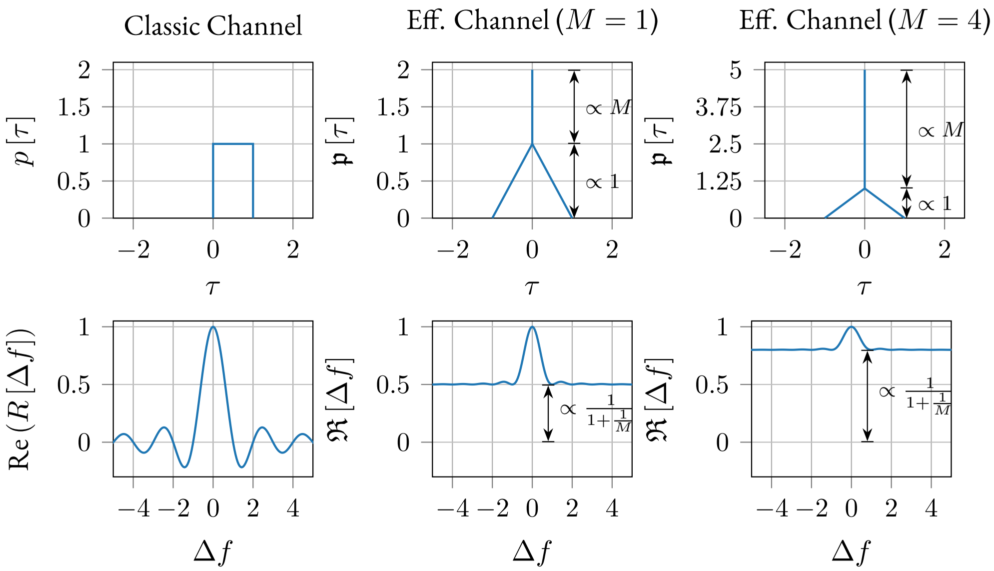
Classic Channel

Eff. Channel ($M = 1$)

Eff. Channel ($M = 4$)

Figure 4.9: The effective PDPs of an original square PDPs and the Fourier related frequency correlation functions are shown in (a), (b), (c) and (d), (e), (f), respectively. The effective channels has a scaling behaviour of the PDP for different numbers of antennas. The increasing peak in the PDP for larger M corresponds to an increasing lower bound on the frequency correlation, which approaches flat fading for large M.

The corresponding effective PDP is derived in Appendix 4.B and is given as

$$\mathfrak{p}_k[n] = p_k[-n] \star p_k[n] + \delta_n M. \tag{4.12}$$

The temporal focusing is visualized in Fig. 4.9 a-c. It can be seen that the ratio of the amount of energy at the zero delay tap to the amount of energy at non-zero taps increases as the number of combined elements grows. The frequency correlation function for all the channels for user k is denoted $R_k[\Delta f]$ and is the Fourier transform of the PDP $p_k[n]$ [71]. The correlation function $\mathfrak{R}_k[\Delta f]$ for the effective channel $\mathfrak{h}_k[n]$ is hence the Fourier transform of $\mathfrak{p}_k[n]$. The PDP $\mathfrak{p}_k[n]$ consist of two terms. The convolution $p_k[-n] \star p_k[n]$ corresponds in the frequency domain to the absolute square of the frequency correlation, that is $|R_k[\Delta f]|^2$. The peak $\delta_n M$ in Eq. (4.12) at zero lag corresponds to an offset for all frequencies. Hence, with a normalization so that $\mathfrak{R}_k[0] = 1$ we obtain

$$\mathfrak{R}_k[\Delta f] = \frac{|R_k[\Delta f]|^2 + M}{1 + M}. \tag{4.13}$$

The link between the PDP and the frequency correlation is illustrated in Fig. 4.9. Because the correlation function $R_k[\Delta f]$ is bounded as $0 \leq |R_k[\Delta f]|^2 \leq 1$, the effective frequency correlation becomes bounded as

$$\frac{1}{1 + 1/M} \leq \mathfrak{R}_k[\Delta f] \leq 1. \tag{4.14}$$

The large offset caused by the matched filtering limits the variability of the frequency correlation function. Even with just one antenna, matched filtering reduces the maximum range of $\mathfrak{R}_k[\Delta f]$ to 3 dB as illustrated in Fig.0 4.9e. For four antennas it is 1 dB and for 8 antennas it is 0.5 dB. Hence, the common 3 dB coherence bandwidth measure can not be applied for the effective channel using matched filtering, as the coherence bandwidth will become the whole bandwidth when using two or more antennas. The channel hardening is here seen as the reduction in frequency selectivity, which results in a coherence bandwidth equal to almost the full bandwidth. Using an instantaneous power constraint would even further reduce the variability.

As the variability of the frequency response $\mathfrak{H}_k[f]$ reduces with M the coherence bandwidth will increase simply because all the subcarriers will have just minor differences in amplitude around a dominating average.

4.5.3 The Effective Delay Spread

The effective PDP $\mathfrak{p}[n]$ will have an effective delay spread given by

$$\hat{\tau}_{rms} = \Delta\tau \sqrt{\frac{\sum_{n=-\infty}^{\infty} n^2 \mathfrak{p}[n]}{\sum_{n=-\infty}^{\infty} \mathfrak{p}[n]}}, \tag{4.15}$$

where $\Delta\tau$ is the duration between samples. To be able to study the variability of temporal focusing of the matched filtering for the realizations we use the instantaneous delay spread, adapted from [72],

$$\hat{\tau}^{i}_{rms_k} = \Delta\tau \sqrt{\frac{\sum_{n=-\infty}^{\infty} n^2 \left|\mathfrak{h}_k[n]\right|^2}{\sum_{n=-\infty}^{\infty} \left|\mathfrak{h}_k[n]\right|^2}}, \tag{4.16}$$

where the expectations in Eq. (4.15) are exchanged with realizations. Channel hardening manifests as a reduction in variability whereas temporal focusing results in an over all reduction of this measure. Fig. 4.10 shows the empirical CDF of the instantaneous rms delay spread for all channel realizations. Both the value and the variability of $\hat{\tau}^{i}_{rms_k}$ reduce with M. For large M this will make it possible to have low complexity receivers in the DL as the channel effectively becomes a single tap channel.

The ratio between the effective delay spread $\hat{\tau}_{rms}$ and the delay spread before combining τ_{rms}, derived in Appendix 4.C, can be expressed as a function of the number of antennas M as

$$\frac{\hat{\tau}_{rms}}{\tau_{rms}} = \sqrt{\frac{2}{1+M}}. \tag{4.17}$$

For a single antenna the matched filtering does not change the delay spread. Fig. 4.11 shows the ratio $\hat{\tau}_{rms}/\tau_{rms}$ for the empirical delay spread from the measurements together with the ratio given by Eq. (4.17). The delay spread converges slower to a single tap than the coherence bandwidth approaches the full bandwidth when increasing the number of combined antennas. Using 7 antennas will halve the delay spread whereas 16 antennas reduce it by approximately a third and 32 by a fourth.

The observed channel hardening is the focusing of the signal in the delay domain resulting in a smaller delay spread. In addition, the variability of the delay spread in the realizations reduce with increasing numbers of combined antennas as seen in Fig. 4.10.

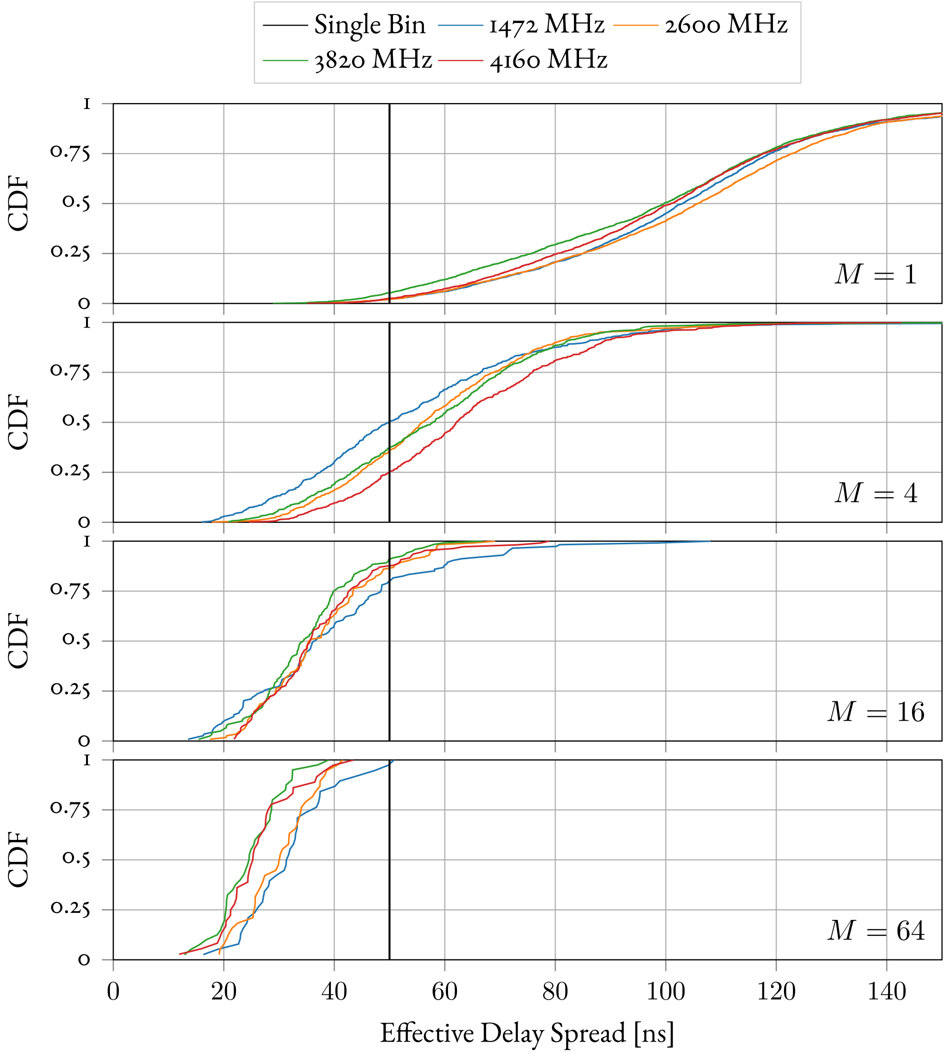

Figure 4.10: Empirical CDFs for the effective delay spread. Both the mean as well as the variance are decreasing for an increasing number of antennas, demonstrating temporal focusing and channel hardening. A base station with 64 antennas could shrink the delay spread to fit into a single delay bin allowing for a simplified receiver at the user side.

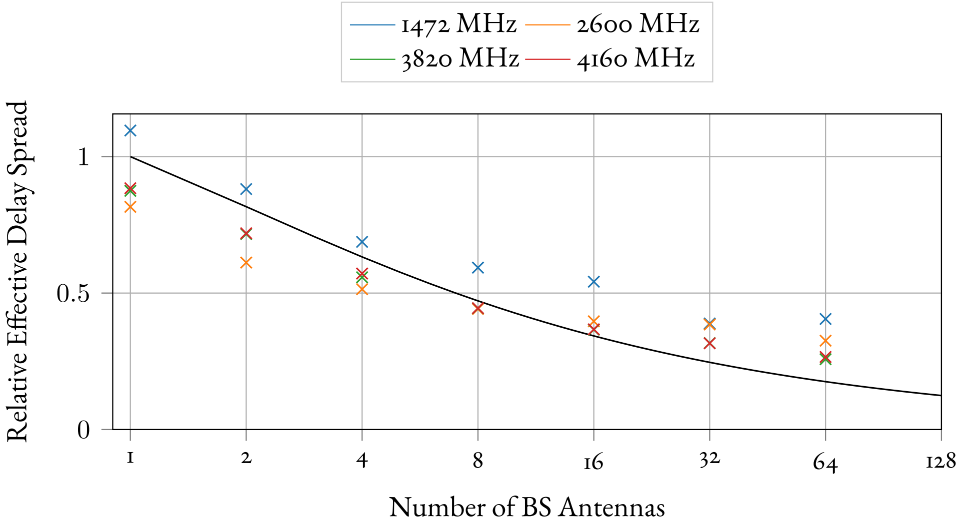

Figure 4.11: The ratio of effective delay spread and the delay spread of the channel as a function of antennas used for combining is shown. The theoretical scaling is drawn with a black line (Eq. (4.17)). A system with 8 antennas at the base station could reduce the delay spread by a factor of two and the effect has diminishing returns for larger systems.

4.6 Conclusion

Measured data from a quasi-static indoor radio environment over four frequency bands in the range from 1.4 GHz to 4.2 GHz are used to study channel hardening properties in massive MIMO when using time-reversal precoding. The measurements contain 40 single user realizations against a 64 element antenna array BS to elucidate channel hardening in both the delay and the frequency domain. The observed statistical properties for the channels are practically the same over the studied frequency bands. The coherence bandwidth is demonstrated to have limited merit as a measure for the effective DL channel. The rms delay spread and the normalized subcarrier power of the effective radio channel are described as physically motivated figures of merit for low complexity single tap receivers.

4.A Expectation of the Effective Channel Power in the Frequency Domain

Taking the small-scale coefficients $H_m[f] \sim \mathcal{CN}(0,1)$ from a user to antenna m on subcarrier f and normalizing the matched filter weights $W_m[f]$ with $\sqrt{M}$ allows us to write the effective channel with dropped user dependency in Eq. (4.4) as follows:

$$\begin{aligned}\mathfrak{H}[f] &= \sum_M W_m[f]H_m[f] = \frac{1}{\sqrt{M}}\sum_M H_m^*[f]H_m[f] \\ &= \frac{1}{\sqrt{M}}\sum_M |H_m[f]|^2 .\end{aligned} \tag{4.18}$$

As $\mathbb{E}\{|H_m[f]^2|\} = 1$ and $\mathbb{E}\left\{|H_m[f]|^4\right\} = 2$ for a complex circular Gaussian variable with unit variance [73], using the Kronecker delta function δ_{ij}, the effective channel power is obtained as

$$\begin{aligned}\mathbb{E}\left\{|\mathfrak{H}[f]|^2\right\} &= \frac{1}{M}\sum_{m=1}^{M}\sum_{l=1}^{M}\mathbb{E}\left\{|H_m[f]|^2\,|H_l[f]|^2\right\} \\ &= \frac{1}{M}\sum_{m=1}^{M}\sum_{l=1}^{M}\begin{bmatrix}(1-\delta_{ml})\,\mathbb{E}\left\{|H_m[f]|^2\right\}\mathbb{E}\left\{|H_l[f]|^2\right\} \\ +\delta_{ml}\,\mathbb{E}\left\{|H_m[f]|^4\right\}\end{bmatrix} \\ &= \frac{1}{M}\sum_{m=1}^{M}\sum_{l=1}^{M}(1-\delta_{ml}) + 2\delta_{ml} \\ &= \frac{1}{M}\sum_{m=1}^{M}\sum_{l=1}^{M}(1+\delta_{ml}) = \frac{1}{M}\left(M^2+M\right) = M+1.\end{aligned} \tag{4.19}$$

Hence, the expectation of the effective channel power and the SNR in the DL scales with $M+1$, if the weights are normalized with $\sqrt{M}$.

4.B Power Delay Profile of the Effective Channel

Examining the single user case the user index is neglected. The channel from UE to antenna m is given as $h_m \sim \mathcal{CN}\left(0, p[n]\right)$, where $p[n]$ is the power delay profile assumed the same over the whole array. The average channel gain is one, that is $\sum_{n=0}^{\infty} p[n] = 1$. With the matched filtering $w_m[n] = h_m^*[-n]/\sqrt{M}$ the PDP for an effective channel is the expectation of the absolute square of the effective channel impulse response,

$$\mathfrak{p}[n] = \mathbb{E}\{|\mathfrak{h}[n]|^2\} = \mathbb{E}\left\{\frac{1}{M}\left|\sum_{m=1}^{M} h_m^*[-n] \star h_m[n]\right|^2\right\} \tag{4.20}$$

As the channels $h_m[n]$ are causal, the matched filtering of channel m, that is the convolution, can be expressed as

$$\begin{aligned}\mathfrak{h}_m[n] &= w_m[n] \star h_m[n] = \frac{h^*{}_m[-n]}{\sqrt{M}} \star h_m[n] \\ &= \frac{1}{\sqrt{M}} \sum_{\nu=-\infty}^{\infty} h_m^*[-\nu] h_m[n-\nu] \\ &= \frac{1}{\sqrt{M}} \sum_{\nu=-\infty}^{0} h_m^*[-\nu] h_m[n-\nu] = \frac{1}{\sqrt{M}} \sum_{\nu=0}^{\infty} h_m^*[\nu] h_m[n+\nu].\end{aligned} \tag{4.21}$$

Here $\mathfrak{h}_m[n]$ is the effective channel for a single antenna m after matched filtering. The expectation is

$$\mathbb{E}\{\mathfrak{h}_m[n]\} = \frac{1}{\sqrt{M}} \sum_{\nu=0}^{\infty} \underbrace{\mathbb{E}\{h_m^*[\nu] h_m[n+\nu]\}}_{\delta_n p[\nu]} = \frac{\delta_n}{\sqrt{M}} \tag{4.22}$$

where we use that the sum power in the PDP is one and the corresponding effective PDP for antenna m is

$$\begin{aligned}\mathfrak{p}_m[n] = \mathbb{E}\left\{|\mathfrak{h}_m[n]|^2\right\} &= \mathbb{E}\left\{\frac{1}{M}\left|\sum_{\nu=0}^{\infty} h_m^*[\nu]\star h_m[n+\nu]\right|^2\right\}\\ &= \frac{1}{M}\sum_{\nu=0}^{\infty}\sum_{\mu=0}^{\infty}\mathbb{E}\{h_m^*[\nu]h_m[n+\nu]h_m[\mu]h_m^*[n+\mu]\}\,. \end{aligned} \tag{4.23}$$

The expectation in the sum can be broken down in four terms, each a combination of $n = 0, n \neq 0$ and $\nu = \mu, \nu \neq \mu$. Using δ_{ij} and the unit impulse δ_i to separate the terms we obtain

$$\begin{aligned}&\mathbb{E}\{h_m^*[\nu]h_m[n+\nu]h_m[\mu]h_m^*[n+\mu]\} =\\ &(1-\delta_n)(1-\delta_{\nu\mu})\cdot 0 + \delta_n(1-\delta_{\nu\mu})\underbrace{\mathbb{E}\left\{|h_m[\nu]|^2\right\}}_{p[\nu]}\underbrace{\mathbb{E}\left\{|h_m[\mu]|^2\right\}}_{p[\mu]}\\ &+(1-\delta_n)\delta_{\nu\mu}\underbrace{\mathbb{E}\left\{|h_m[\nu]|^2\right\}}_{p[\nu]}\underbrace{\mathbb{E}\left\{|h_m[n+\nu]|^2\right\}}_{p[n+\nu]} + \delta_n\delta_{\nu\mu}\underbrace{\mathbb{E}\left\{|h_m[\nu]|^4\right\}}_{2p^2[\nu]}\end{aligned} \tag{4.24}$$

Using the WSSUS model, taps corresponding to different delays are independent and hence the first term is zero. Gathering the terms containing either $\delta_{\nu\mu}$ or δ_n in Eq. (4.24) the expectation becomes

$$\begin{aligned}&\mathbb{E}\{h_m^*[\nu]h_m[n+\nu]h_m[\mu]h_m^*[n+\mu]\}\\ &\quad= \delta_{\nu\mu}p[\nu]p[n+\nu] + \delta_n p[\nu]p[\mu]\end{aligned} \tag{4.25}$$

Using this in Eq. (4.23) the effective PDP for channel m is obtained as

$$\begin{aligned}\mathfrak{p}_m[n] &= \frac{1}{M}\sum_{\nu=0}^{\infty}\sum_{\mu=0}^{\infty}\left(\delta_{\nu\mu}p[\nu]p[n+\nu] + \delta_n p[\nu]p[\mu]\right)\\ &= \frac{1}{M}\sum_{\nu=0}^{\infty}p[\nu]p[n+\nu] + \frac{\delta_n}{M}\underbrace{\sum_{\nu=0}^{\infty}p[\nu]}_{1}\underbrace{\sum_{\mu=0}^{\infty}p[\mu]}_{1}\\ &= \frac{1}{M}\left(p[-n]\star p[n] + \delta_n\right)\end{aligned} \tag{4.26}$$

Using Eq. (4.22) the expectation of the effective channel is

$$\mathbb{E}\{\mathfrak{h}[n]\} = \mathbb{E}\left\{\sum_{m=1}^{M} \mathfrak{h}_m[n]\right\} = \sqrt{M}\delta_n \tag{4.27}$$

The effective PDP after combining is

$$\mathfrak{p}[n] = \mathbb{E}\left\{\left|\sum_{m=1}^{M} \mathfrak{h}_m[n]\right|^2\right\} = \sum_{m=1}^{M}\sum_{l=1}^{M} \mathbb{E}\{\mathfrak{h}_m[n]\mathfrak{h}_l^*[n]\} \tag{4.28}$$

Approaching the expectation in the same manner as in Eq. (4.24) we obtain

$$\begin{aligned}\mathbb{E}\{\mathfrak{h}_m[n]\mathfrak{h}_l^*[n]\} = {} & (1-\delta_n)(1-\delta_{ml})\cdot 0 \\ & + \delta_n(1-\delta_{ml})\underbrace{\mathbb{E}\{\mathfrak{h}_m[0]\}}_{1/\sqrt{M}}\underbrace{\mathbb{E}\{\mathfrak{h}_l[0]\}}_{1/\sqrt{M}} + \delta_{ml}\underbrace{\mathbb{E}\left\{|\mathfrak{h}_m[n]|^2\right\}}_{\mathfrak{p}_m[n]}\end{aligned} \tag{4.29}$$

which when introduced in Eq. (4.28) together with Eq. (4.26) result in

$$\begin{aligned}\mathfrak{p}[n] &= \sum_{m=1}^{M}\sum_{l=1}^{M}\left(\delta_{ml}\mathfrak{p}_m[n] + \frac{\delta_n(1-\delta_{ml})}{M}\right) \\ &= \sum_{m=1}^{M}\mathfrak{p}_m[n] + (M-1)\,\delta_n \\ &= p[-n]\star p[n] + M\delta_n.\end{aligned} \tag{4.30}$$

The effective PDP has the shape of the convolution of the underlying PDP with it's reverse with an additional $M\delta_n$ peak in the middle, formed by the coherent summing. The gain of the effective PDP is

$$\begin{aligned}\sum_{n=-\infty}^{\infty}\mathfrak{p}[n] &= \sum_{n=-\infty}^{\infty}\sum_{\nu=0}^{\infty} p[\nu]p[n+\nu] + M\sum_{n=-\infty}^{\infty}\delta_n \\ &= \underbrace{\sum_{\nu=0}^{\infty}p[\nu]}_{=1}\underbrace{\sum_{n=-\infty}^{\infty} p[n+\nu]}_{=1} + M = 1 + M\end{aligned} \tag{4.31}$$

Of special interest is the center tap $\mathfrak{p}[0]$ which is obtained from Eq. (4.29) and that can be bounded as

$$M < \mathfrak{p}[0] = \sum_{\nu=0}^{\infty} p^2[\nu] + M \leq 1 + M. \tag{4.32}$$

where we use that all the terms in the sum are either zero or positive and that $p^2[n] \leq p[n] \leq 1$.

4.C Delay Spread of the Effective Channel

As the effective PDP is symmetric around zero the average delay is zero. The squared delay spread for the effective channel is therefore given by

$$\hat{\tau}_{rms}^2 = \Delta\tau^2 \frac{\sum_{n=-\infty}^{\infty} n^2 \mathfrak{p}[n]}{\sum_{n=-\infty}^{\infty} \mathfrak{p}[n]} = \frac{\Delta\tau^2}{M+1} \sum_{n=-\infty}^{\infty} n^2 p[-n] \star p[n] \tag{4.33}$$

where we insert the result from Eq. (4.29) and use Eq. (4.30). The delay spread of the channels is given by

$$\bar{\tau} = \Delta\tau \frac{\sum_{n=0}^{\infty} n p[n]}{\sum_{n=0}^{\infty} p[n]} = \Delta\tau \sum_{n=0}^{\infty} n p[n] \tag{4.34}$$

$$\tau_{rms}^2 = \Delta\tau^2 \frac{\sum_{n=0}^{\infty} n^2 p[n]}{\sum_{n=-\infty}^{\infty} p[n]} - \bar{\tau}^2 = \Delta\tau^2 \sum_{n=0}^{\infty} n^2 p[n] - \bar{\tau}^2 \tag{4.35}$$

For notational convenience we set $\Delta\tau = 1$ and henceforth express the average delay and delay spread in samples. The effective delay spread can then be expressed as

$$\begin{aligned} \hat{\tau}_{rms}^2 &= \frac{1}{M+1} \sum_{n=-\infty}^{\infty} n^2 \sum_{\nu=0}^{\infty} p[\nu] p[n+\nu] \\ \overset{[}{\mu}= n + \nu] &= \frac{1}{M+1} \sum_{\nu=0}^{\infty} p[\nu] \sum_{\mu=-\infty}^{\infty} (\mu - \nu)^2 p[\mu], \end{aligned} \tag{4.36}$$

where a variable substitution in the second equality make it possible to separate the sums. The second sum can be evaluated as

$$\sum_{\mu=0}^{\infty}(\mu-\nu)^2 p[\mu] = \underbrace{\sum_{\mu=-\infty}^{\infty} \mu^2 p[\mu]}_{\tau_{rms}^2-\bar{\tau}^2} - 2\nu \underbrace{\sum_{\mu=-\infty}^{\infty} \mu p[\mu]}_{\bar{\tau}} + \nu^2 \underbrace{\sum_{\mu=-\infty}^{\infty} p[\mu]}_{=1} \qquad (4.37)$$

which introduced back in Eq. (4.36) and performing the same type of evaluation of the sum as above result in

$$\hat{\tau}_{rms}^2 = \frac{1}{M+1}\sum_{\nu=0}^{\infty} p[\nu]\left(\tau_{rms}^2 - \bar{\tau}^2 - 2\nu\bar{\tau} + \nu^2\right) = \frac{2\tau_{rms}^2}{M+1} \qquad (4.38)$$

The ratio of the delay spread between the original channels and the effective channel after MRC or MRT is hence

$$\frac{\hat{\tau}_{rms}}{\tau_{rms}} = \sqrt{\frac{2}{1+M}}. \qquad (4.39)$$

With a single antenna and matched filtering the delay spread is unaffected.

Acknowledgments

ReRaNP is supported by the Norwegian Research Council within the National Financing Initiative for Research Infrastructure. Further support was provided by Telenor ASA within the project Testing RAN Options for 5G.

5 Paper C1: Power Inversion of the Massive MIMO Channel

Authors	J. Abraham and T. Ekman
Conference	9th joint WIC IEEE SP Symposium on Information Theory and Signal Processing in the Benelux
Place	Gent, Belgium
Date	May, 2019
Original-URL	`http://w-i-c.org/proceedings/proceedings_SITB2019.pdf`
arXiv	1905.07555

Changenotes

- Notation
  - $\mathcal{E}\left\{\cdot\right\}$ changed to $\mathbb{E}\{\cdot\}$
  - $\mathcal{V}\left\{\cdot\right\}$ changed to $\mathbb{V}\{\cdot\}$
- modified legend entries of Fig. 5.1 to make plot lines visible on B5 paper

5.1 Abstract

Channel hardening characterises the diminishing influence of small scale fading on large scale antenna systems. The effective massive MIMO time domain channel is introduced and applied to a maximum diversity channel with rectangular power delay profile. This model bounds channel hardening and allows a proper interpretation from a radio design perspective. The reduced variability of the effective channel enables power inversion to obtain a downlink channel that only depends on the large scale fading properties.

5.2 Introduction

WSN are of increasing interest to industry and governments for surveillance of different environments. Large scale antenna systems (such as massive MIMO BS [23]) could become a leading technology to provide a robust single hop data link for thousands of sensor nodes. They make it possible to move complexity from the sensors to the BS to increase the lifetime of each node. Channel hardening and favourable propagation allow the simplification of the node transceiver design and a reduction of their output power. An alternative approach are mesh networks, but they suffer from uneven power usage for nodes close to the data gateway.

Even though a single radio channel can experience small and large scale fading (here pathloss and shadowing), it is highly unlikely that all antenna elements experience a fading dip at the same time. Thus, large scale antenna systems can exploit spatial diversity to compensate for small scale fading. Furthermore, the array gain can overcome some large scale fading.

This paper formulates an effective massive MIMO channel in the time domain, to describe the small scale fading in the downlink with a relative power measure. A similar approach in the frequency domain was chosen by the authors to investigate the behaviour of rms delay spread under channel hardening [R1]. The effective channel can directly be used to bound the fading margin and adheres to the philosophy that a receiver requires first and foremost a signal level above or at a minimal threshold. Both centralised and distributed normalisations of time reversal precoding and their influence on the remaining small scale fading are studied. In addition, focus is placed on the relative antenna element and BS power. The former is defining the required dynamic range of the BS transmitters. The latter is mainly of regulatory interest, but confines the overall power consumption of the BS in addition.

The next section describes the effective massive MIMO channel with consideration of time reversal precoding, normalisation and relative power measures. The following section shows the distributions for the relative power measures of a maximum diversity channel to give a best case bound of channel hardening. Afterwards, the results are applied to a four tap channel to demonstrate the ideal theoretical behaviour of large scale antenna systems with a growing number of transmitters. The last section summarises the findings and discusses necessary steps to realise time reversal power inversion for robust large scale antenna system WSNs.

5.3 The Effective Massive MIMO Channel

The complex valued input-output relation at time index n for downlink signal $x_l[n]$ intended for user l and signal $y_k[n]$ received by user k in a K user system with M antennas at the BS is described by

$$\begin{aligned} y_k[n] &= \sqrt{\beta_k} \sum_{l=1}^{K} \underbrace{\left(\sum_{m=1}^{M} h_{mk}[n] \star w_{ml}[n] \right)}_{\mathfrak{h}_{kl}[n]} \star x_l[n] + e_k[n] \\ &= \underbrace{\sqrt{\beta_k}\mathfrak{h}_{kk}[n] \star x_k[n]}_{\text{signal}} + \underbrace{\sqrt{\beta_k} \sum_{\substack{l=1 \\ l \neq k}}^{K} \mathfrak{h}_{kl}[n] \star x_l[n]}_{\text{multi-user interference}} + \underbrace{e_k[n]}_{\text{noise}} \end{aligned} \tag{5.1}$$

where β_k, e_k are large scale fading coefficient and noise, $h_{mk}[n]$ and $w_{ml}[n]$ are small scale fading channel impulse response for user k and precoding filter for user l transmitted from antenna m. The $\star$ denotes the convolution between two signals. Here β_k normalises the channel impulse response as

$$\mathbb{E}\left\{ \sum_{n=1}^{N} |h_{mk}[n]|^2 \right\} = 1 \tag{5.2}$$

with $\mathbb{E}\{\cdot\}$ denoting the expectation. Intrinsically, β_k is a global variable for all SISO channels from a user to the M BS antennas.

The effective channels $\mathfrak{h}_{kl}[n]$ are formed by the superposition of all signals from the BS at the user k. The intended effective channel is $\mathfrak{h}_{kk}[n]$, whereas all other effective channels contribute to multi-user interference.

5.3.1 Time Reversal

MRT, ZF and linear MMSE [10], [74] are the commonly used frequency domain linear precoding schemes in large scale antenna systems. MRT optimises the signal to noise ratio of a single user, ignoring MUI. ZF optimises the signal to interference ratio by suppressing MUI, ignoring the SNR of the intended user and the linear MMSE precoder has a control parameter to achieve a trade off between MRT and ZF.

Both ZF and MMSE require a matrix inversion operation of the multi user channel to calculate the precoding weights. The matrix inversion introduces the requirement of centralised weight calculations and is a computational heavy operation. It is our understanding that favourable propagation and user scheduling can alleviate the WSN in a heavily loaded large scale antenna system for WSN. Therefore, MRT will be the inspiration for the considered precoding scheme in the remainder of this paper.

MRT is usually applied to each sub-carrier of an OFDM system and closely related to TR [60]. Following the TR idea, the precoder weights can be calculated from the uplink channel with generic single user normalisation c_l

$$w_{ml}[n] = \frac{h^*_{ml}[-n]}{c_l} \tag{5.3}$$

where * denotes the complex conjugate. This approach reverses the channel impulse response to focus energy at the user in both space and time [11], partly reducing interference at other places. The importance of the effective zero delay tap $\mathfrak{h}_{kk}[0]$ becomes apparent by investigation of the sum over convolutions in Eqn. (5.1). It is the main contributor to the effective channel due to the coherent addition of the underlying SISO channel taps. Solving the convolutions for zero delay results in

$$\mathfrak{h}_{kk}[0] = \frac{1}{c_k} \sum_{m=1}^{M} \sum_{n=1}^{N} |h_{mk}[n]|^2. \tag{5.4}$$

This result describes the radio propagation between the BS and the user in a compressed form and captures the usable signal power for a single tap receiver. The remaining variability of $\mathfrak{h}_{kk}[0]$ is due to the uncompensated small scale fading.

5.3.2 Powers

At the BS, both the *relative antenna element transmit power* $P_{mk}^{\mathrm{Ant,R}}$ and the *relative BS transmit power* $P_{k}^{\mathrm{BS,R}}$ are random variables of interest. The former is describing how much the output power of each antenna is influenced by the precoding weights:

$$P_{mk}^{\mathrm{Ant,R}} = M \sum_{n=1}^{N} |w_{mk}[n]|^2 . \tag{5.5}$$

The distribution of $P_{mk}^{\mathrm{Ant,R}}$ characterises how much each transmitter at the BS has to cope with fluctuations of the antenna element output power. Furthermore, $P_{k}^{\mathrm{BS,R}}$ sums over all squared weights of a specific user to see the impact on the whole BS:

$$P_{k}^{\mathrm{BS,R}} = \sum_{m=1}^{M} \sum_{n=1}^{N} |w_{mk}[n]|^2 . \tag{5.6}$$

At the user, the *relative effective received power* captures the array gain normalised power fluctuation for a single tap receiver

$$P_{k}^{\mathrm{RX,R}} = \frac{1}{M} |\mathfrak{h}_{kk}[0]|^2 . \tag{5.7}$$

These fluctuations describe the remaining small scale fading and hereby how much spatial diversity is exploited by the precoding.

5.3.3 Normalisations

The three relative powers of interest are influenced by the choice of c_l in Eqn. (5.3). To implement a normalisation reminiscent to MMRT, the normalisation constant has to be calculated by

$$c_l^{\mathrm{TR}} = \sqrt{\sum_{m=1}^{M} \sum_{n=1}^{N} |h_{ml}[n]|^2}. \tag{5.8}$$

This scales each realisation of the precoding weights with the current state of the channel and ensures unit gain per user over the whole BS. Unfortunately, it requires a centralised weight calculation. However, the double sum can be replaced by its expectation, leading to a decentralised strategy. The inner sum follows Eqn. (5.2) with expectation one and the outer sum is self-averaging over values fluctuating around one. Eventually, a DTR normalisation can be obtained as:

$$c_l^{\mathrm{DTR}} = \sqrt{\mathbb{E}\left\{\sum_{m=1}^{M} \sum_{n=1}^{N} |h_{ml}[n]|^2\right\}} = \sqrt{M}. \tag{5.9}$$

A third normalisation can be chosen to apply more power to a weaker channel realisation. This PI approach is centralised and has similarity with channel inversion [75], but avoids a matrix inversion operation:

$$c_l^{\mathrm{PI}} = \frac{1}{\sqrt{M}} \sum_{m=1}^{M} \sum_{n=1}^{N} |h_{ml}[n]|^2. \tag{5.10}$$

PI is prohibitive for single antenna systems, because it could lead to an extreme peak-to-average power (PAP) on the antenna element. Nevertheless, it will be shown that finite large scale antenna systems can provide enough diversity to reduce the PAP to a viable amount.

The coefficients are following $c_l^{\mathrm{PI}} \geq c_l^{\mathrm{TR}} \geq c_l^{\mathrm{DTR}}$, if the channel realisation is weaker than the expectation $\sum_{m=1}^{M} \sum_{n=1}^{N} |h_{ml}[n]|^2 < \sqrt{M}$. Hence, PI is inverting the behaviour of TR and DTR where less power is transmitted if the channel realisation is weak.

5.4 Maximum Diversity Channel

A bound for channel hardening is found using an ideal maximum diversity channel. The corresponding PDP is modelled with a rectangular shape and independent identically distributed Rayleigh taps, since maximum diversity is achieved for a diffuse scattering environment if all diversity branches behave the same. The coefficients are therefore following a zero mean circular symmetric complex normal ($\mathcal{CN}$) distribution and we set the variance to $1/N$ for a N tap channel to adhere to the assumption in Eqn. (5.2).

For DTR, $P_{mk}^{\text{Ant,R}}$ is a scaled sum of squares of $h_{mk}[n]$ and each squared channel coefficent follows an exponential distribution. The scaling compensates for c_l^{DTR} such that the result is distributed according to a Gamma distribution with shape N and scale $1/N$ ($\Gamma(N, 1/N)$), since the N addends are independent identically distributed random variables of Gamma type ($\Gamma(1, 1/N)$) [76], [77].

The distributions for the other two normalisations diverge from $\Gamma(N, 1/N)$ since each realisation of the normalisation coefficient varies from $\sqrt{M}$. The variance of TR will be smaller than $1/N$ since less power is applied for weaker channels. The opposite is true for DTR because more power is applied for weaker channels.

For DTR and M independent realisations of the channel coefficents over N delay taps follows $P_k^{\text{BS,R}}$ $\Gamma(MN, 1/(MN))$. TR leads to a constant of one and PI has a higher variance of the relative BS transmit power due to the uncertainty of c_l^{PI} around $\sqrt{M}$.

The remaining small scale fading for a user is captured by the variation of $P_k^{\text{RX,R}}$. PI enforces a value of one, whilst TR leads to a distribution by $\Gamma(MN, 1/(MN))$. For DTR the result follows the square of $\Gamma(MN, 1/(MN))$ being a generalised Gamma distribution [78]. A summary of expectations and variances for the different powers is given in Tab. 5.1 showing the scaling properties with respect to the number of taps N and the number of BS antennas M.

Naturally, the power fluctuations per antenna element are only dependent on the length of the channel, whereas the relative BS transmit and the relative received

Table 5.1: Summary of expectations ($\mathbb{E}\{\cdot\}$) and variances ($\mathbb{V}\{\cdot\}$) for the relative antenna transmit power $P_{mk}^{\text{Ant,R}}$, the relative base station transmit power $P_{k}^{\text{BS,R}}$ and the relative effective received power $P_{k}^{\text{RX,R}}$ for a maximum diversity channel with N tap normalised rectangular power delay profile for a M antenna base station. The values are given for the different time reversal normalisations.

	$P_{mk}^{\text{Ant,R}}$			$P_{k}^{\text{BS,R}}$			$P_{k}^{\text{RX,R}}$		
	DTR	TR	PI	DTR	TR	PI	DTR	TR	PI
$\mathbb{E}\{\cdot\}$	1	1	≥ 1	1	1	≥ 1	$1 + \frac{1}{MN}$	1	1
$\mathbb{V}\{\cdot\}$	$\frac{1}{N}$	$\leq \frac{1}{N}$	$\geq \frac{1}{N}$	$\frac{1}{MN}$	0	$\geq \frac{1}{MN}$	$\frac{4}{MN} + \frac{10}{M^2N^2} + \frac{6}{MN^3}$	$\frac{1}{MN}$	0

power depend on the number the BS antennas providing diversity. We want to point the duality between BS antenna elements and channel taps in the effective channel out. Even for non-ideal channels, both can provide diversity to compensate for small scale fading.

5.5 Simulation

To validate the derived distributions and to demonstrate the impact of the different normalisations on the relative powers simulations were conducted. Realisations of $h_{mk}[n]$ were drawn from $\mathcal{CN}(0, 1/N)$ to apply post processing according to Eqns. (5.5), (5.6) and (5.7). This allows the generation of empirical CDFs and empirical complementary cumulative distribution function (CCDF) to simulate the behaviour of the maximum diversity channel for different finite large scale antenna system sizes.

An ensemble of one million realisations with $N = 4$ is used for demonstration purposes and the results for $M = 4$ and $M = 16$ are presented in Fig. 5.1. The CCDFs of the first row show the distribution of relative antenna element output power due to the realisations of the channel coefficients. As expected, TR and PI require less and more excess power (with respect to a reference at 0 dB) than DTR, respectively. The differences to DTR are vanishing for growing M, since

c_l^{TR} and c_l^{PI} are converging to $c_l^{DTR} = \sqrt{M}$ due to the self-averaging properties of the large scale antenna system.

The CCDF of $P_k^{\mathrm{Ant,R}}$ can for moderately sized finite large scale antenna systems be predicted from the distribution of the channel coefficients. For $M = 16$ do the requirements for PI and MRT vary less then 0.5 dB with respect to DTR.

The next row in Fig. 5.1 shows the CCDFs for the relative BS transmit power. Both, DTR and PI require more excess sum power then TR, but the difference is reduced for larger M. It is important to note that the reduction comes from averaging over multiple realisations of antenna output powers. Hence, the unit normalisation of TR is giving no insight into how the antenna element output powers are behaving. It only ensures that the sum over all antenna elements becomes one for the specific user.

The bottom row in Fig. 5.1 shows the CDFs for the relative received power at a user. The distributions describe the remaining small scale fading directly. PI compensates it completely whilst TR and DTR reduce it's severity. DTR is prone to a doubling in dB with respect to TR but opens up for distributed weight calculations. The trade-off between distributed and centralised weight calculation is directly accessible from the distribution of $P_k^{\mathrm{RX,R}}$. Furthermore, the results show how much the channel hardening is exploited by the different time reversal normalisations.

Fig. 5.2 shows how the empirical CCDFs and CDFs behave at a probability of 10^{-4} for growing M and $N = 4$. Channel hardening leads to fast convergence of the relative antenna element power to 6 dB, no matter the chosen normalisation. In addition, the relative power of the whole BS is converging towards the TR constant of 0 dB. The penalty of excess power between PI and DTR is vanishing around 32 antenna elements. Finally, small scale fading has a diminishing effect for TR and DTR. In summary, the figure shows the trade-offs for a four tap maximum diversity channel. If small scale fading is supposed to be mitigated completely, then PI could be used if a slight excess in output power from each antenna is acceptable. Each transmitter for a 32 antenna system would have to supply about 0.2 dB more excess power then TR, leading to an increased BS output power of 1.5 dB in less then 10^{-4} cases.

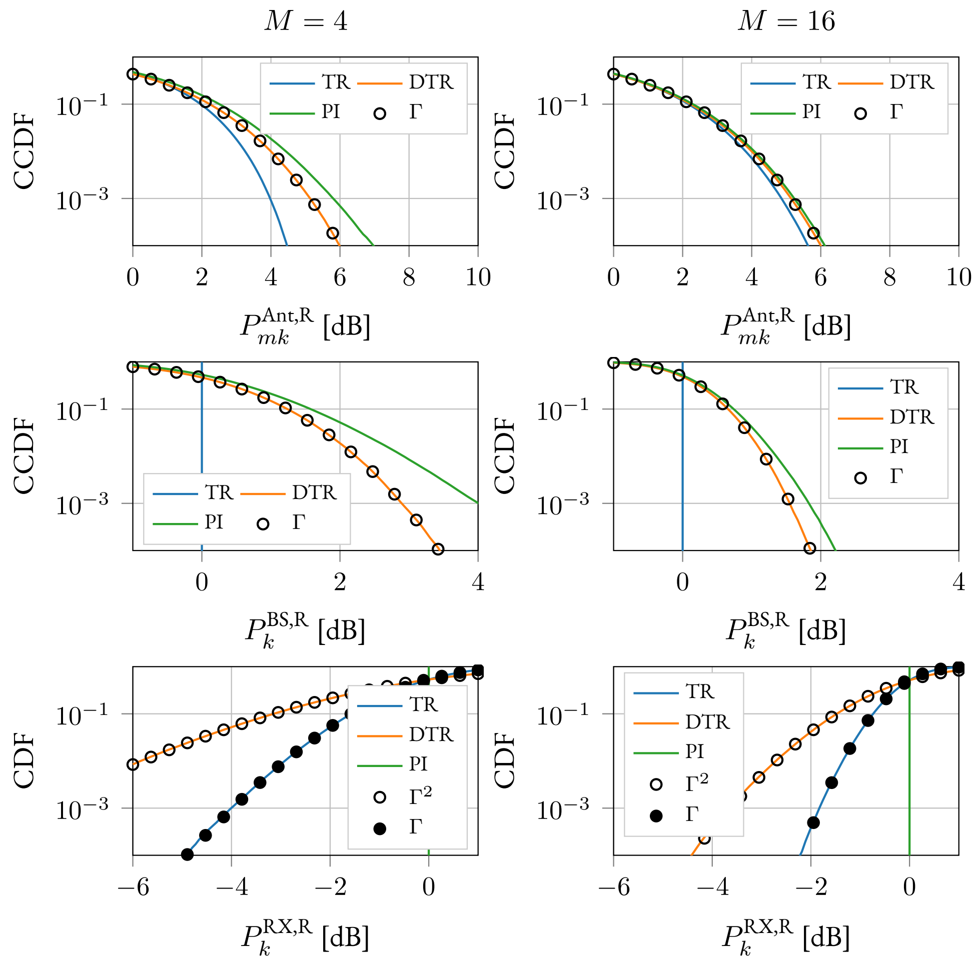

Figure 5.1: Empirical CCDFs are shown for the single antennas and the base station to highlight the excessive relative output power probabilities of a maximum diversity channel with a four tap rectangular power delay profile. The bottom row shows the empirical CDFs for the relative effective received power showing the remaining effects of small scale fading on the effective channel. Different normalisation coefficients are used for the time reversal weights: TR, DTR and PI.

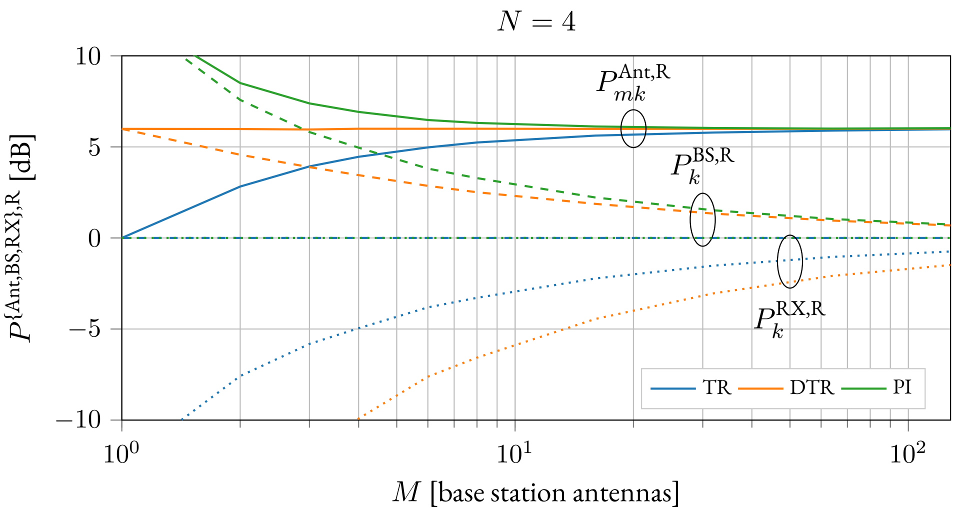

Figure 5.2: For the same simulation scenario as in Fig. 5.1 are relative power levels displayed. $P_{mk}^{\text{Ant,R}}$ and $P_k^{\text{BS,R}}$ represent the antenna element and the whole base station, respectively. The displayed values are exceeded with a probability of 10^{-4}. Additionally, relative power levels at the receiver $P_k^{\text{RX,R}}$ fall short of the shown value with the same probability.

The simulated findings encourage to incorporate realistic PDPs for comparison to the ideal maximum diversity channel. Additionally, measurements could provide the realisations for the empirical CCDFs and CDFs in realistic environments. Ultimately, fully synchronised uplink and downlink measurements should be conducted to verify that PI can completely compensate for small scale fading without exceeding a certain PAP requirement.

5.6 Conclusion

This paper considers the effective massive MIMO channel in the time domain to analyse the severity of small scale fading for an ideal maximum diversity channel. This approach bounds the remaining small scale fading and shows the exploitation of channel hardening. Time reversal precoding with different normalisations is described and the impact on relative transmitter power, sum BS power and effective received power for a single tap receiver is demonstrated. Furthermore, distributions for the relative powers with DTR normalisation are given. They can be used to bound the remaining small scale fading for system design purposes.

For large scale antenna systems, the actual normalisation coefficient has little impact on the relative excess transmit power requirement for each BS antenna element, but influences the excess sum BS power. The latter is merely of regulatory interest and depends on the averaging time window given by the authorities, since each single transmitter needs to fulfil it's PAP requirements nonetheless.

A time reversal precoder can allow for either distributed (DTR) or centralised (TR and PI) weight calculations. DTR relaxes the requirements on inter BS communication, since all fast weight calculations can be done locally at each antenna element. However, additional power needs to be spent to guarantee a specified downlink performance as the remaining small scale fading is larger than for TR.

If the system design allows for centralised weight calculation, then PI can be chosen over TR to compensate for the remaining small scale fading. The penalty is a slightly fluctuating relative BS power to realise a fixed relative received power at the user, whilst the requirements for the relative transmitter power increases negligibly.

The present study suggests that PI is realisable for environments with sufficient spatial diversity. An ideal 16 antenna system observing a maximum diversity four tap channel provides 64 degrees of freedom and the penalty for increasing the robustness of the link is as small as 0.5 dB excess power per antenna element in 10^{-4} cases. The overall BS power has an expectation of around one and exceeds it in less then 10^{-4} cases by 2.2 dB. The BS excess power is mainly of regulatory interest because the BS has to provide similar transmitters for all presented normalisations. Eventually, the resulting effective downlink channel can compensate for small scale fading, leaving the system engineer to consider large scale fading for the design of WSNs.

6 Paper C2: Achievable Synchronisation Gain in Uncalibrated Large Scale Antenna Systems

Authors	J. Abraham and T. Ekman
Conference	14th European Conference on Antennas and Propagation
Place	Copenhagen, Denmark
Date	March, 2020
Original-URL	`https://ieeexplore.ieee.org/document/9136063`
DOI	10.23919/EuCAP48036.2020.9136063

Changenotes

- Notation
    - K-factor changed to $\mathcal{K}$-factor and K changed to $\mathcal{K}$
    - β_m changed to φ_m
    - $\mathcal{E}\{\cdot\}$ changed to $\mathbb{E}\{\cdot\}$
    - $\boldsymbol{H}^{\mathrm{S}}$ changed to $\bar{\boldsymbol{H}}$ and $\boldsymbol{H}^{\mathrm{D}}$ changed to $\tilde{\boldsymbol{H}}$
    - P^S changed to $\bar{P}$ and P^D changed to $\tilde{P}$
    - l changed to b and L changed to B
- Eqn. (6.1) lacked absolut value of $\boldsymbol{W}^{\mathrm{H}}\boldsymbol{H}$
- Eqns. (6.17) and (6.18) showed the maximum order statistic of $\left(\mathbf{B}^{\mathrm{H}}\boldsymbol{H}\right)_{L:L}$ in the published manuscript

6.1 Abstract

Large scale antenna systems are used to exploit spatial multiplexing gains in massive MIMO systems. To realise those gains, channel state information has to be acquired at a base station. However, an initial control channel has to be provided to synchronise time and frequency at the user. This control channel should be undirected to cover the base stations operational area and can therefore not exploit the coherent array gain without additional strategies. Beam sweeping has been proposed to provide increased spatial coverage. Its performance for large scale antenna systems in Rayleigh and Rician fading environments is analysed. Even an orthogonal basis of antenna weights for full spatial coverage can not provide the full array gain. The results quantify the gap between achievable synchronisation and full array gain for uncorrelated antennas. Closed form solutions for the distribution of the gain gap under Rayleigh fading conditions are derived.

6.2 Introduction

Large scale antenna systems are an integral part of massive MIMO base stations (BS). By scaling the number of BS antennas up, both channel hardening and favourable propagation can be exploited, leading to increased spectral efficiency and robustness of the radio channel [23].

Most massive MIMO studies assume at least implicitly that the BS receives some potentially noisy uplink pilots to estimate the radio channel. Relying on reciprocity, just the N users (UEs) of the system have to transmit pilots to allow the estimation of the full $N \times M$ radio channel matrix, where M is the number of BS antennas. This approach provides the possibility of scaling M without impact on the channel estimation process for a constant number of simultaneous UEs. Precoding with linear methods allows to exploit the array gain under favourable propagation conditions.

Unfortunately, each participating UE has to synchronise to a BS at some point to acquire at least frequency and timing information. Even random access protocols are relying on an initial synchronisation signal (e.g. [79]). This signal needs to be broadcast over the whole intended coverage area of the BS. There will be a gap between the *UE focused channel gain* with perfect channel state information (CSI) and the *synchronisation gain* of the broadcast channel without CSI. The gain gap is, for a fixed BS sum power, growing linearly with the number of antennas at the BS [55].

To overcome the gain gap, single high power beacon signals could be considered. Unfortunately, this solution is not scalable for large scale antenna systems as it would require M times the single element power. For spatially restricted measurements, synchronisation between BS and UEs can be provided by cable [17].

Real world deployments require over-the-air synchronisation. The Argos testbed implemented an open-loop beamforming strategy to increase the synchronisation gain [55]. This method employs multiple beam pattern to scan the full channel subspace spanned by the BS antennas. The scanning increases the probability that a UE is illuminated by at least one beam pattern to receive synchronisation information. Additional time for the subspace scan is traded for increased synchronisation gain.

The following manuscript provides a theoretical analysis of beam sweeping in large scale antenna systems for both Rayleigh and Rician fading channels with uncorrelated antenna elements. Section 6.3 introduces the radio channel, followed by the description of the statistical framework in section 6.4. A comparison of different numbers of BS antennas is provided in section 6.5 and the impact of array calibration is afterwards discussed in section 6.6.

6.3 Prerequisites

6.3.1 Performance Measures

Assuming a single carrier flat fading channel allows us to model the radio channel towards the M BS antenna elements as a complex vector $\boldsymbol{H}$ of length M. This channel is excited by the conjugate transpose of a transmit weights vector $\boldsymbol{W}$ of

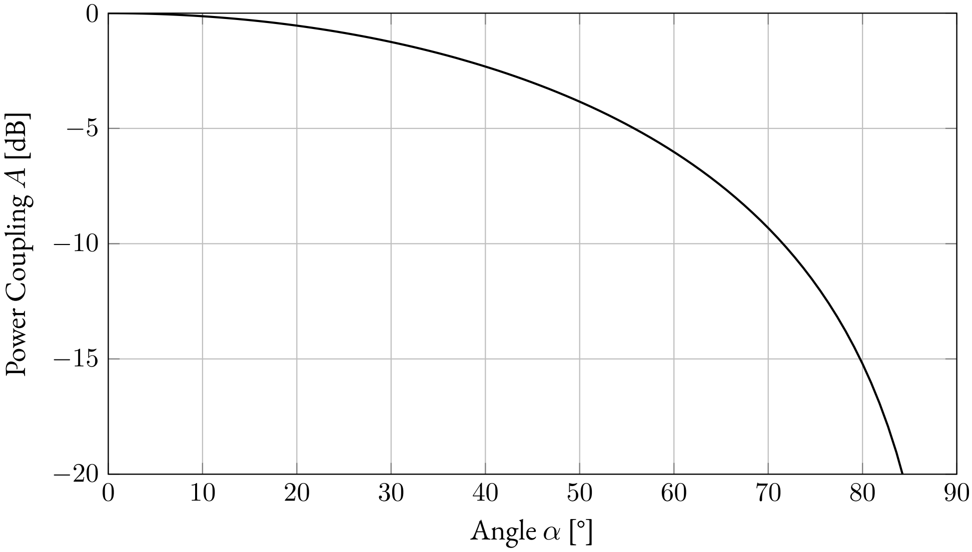

Figure 6.1: Power coupling for different angles between the antenna weight vector and the radio channel vector. 45° and 60° lead to −3 dB and −6 dB, respectively.

length M and the Hermitian angle [20] α between both vectors describes the coupling of the envelope signal:

$$\cos\alpha = \frac{|\boldsymbol{W}^{\mathrm{H}}\boldsymbol{H}|}{\|\boldsymbol{W}\|_2\,\|\boldsymbol{H}\|_2}. \tag{6.1}$$

The power coupling $A = \cos^2\alpha$ follows subsequently and describes the gap between the full array gain and the potentially mismatched excitation of the channel. Fig. 6.1 shows the power coupling as a function of the angle α.

6.3.2 Radio Channel Model

A Rician channel is used to model a broad class of radio environments. This channel model superimposes a specular and diffuse component. The specular component is a single, on the BS array impinging, deterministic plane wave with power $\bar{P}$. The diffuse component has an expected power $\tilde{P}$. Both powers are set into relationship by the $\mathcal{K}$-factor $\mathcal{K} = \bar{P}/\tilde{P}$ ranging from 0 (no specular component, Rayleigh case) to infinity (no diffuse component, single planar wave). The sum power $\bar{P} + \tilde{P}$ is set to unity without loss of generality. Thereby, the channel model is decoupled from large scale fading to highlight small scale fading properties.

The specular component with wave vector $\boldsymbol{k}$ leads to a deterministic phase change over the array with position matrix $\mathbf{r} = [\mathbf{r}_1, \mathbf{r}_2, \dots, \mathbf{r}_M]^{\mathrm{T}}$ where each $\mathbf{r}_m$ describes the position of one element. Hence the phase shifts for the specular component can be collected in the vector $\bar{\boldsymbol{H}}$ with elements:

$$\bar{\boldsymbol{H}}_m = \exp\left(-j\mathbf{r}_m\boldsymbol{k}\right). \tag{6.2}$$

The diffuse component is described by a complex normal distribution

$$\tilde{\boldsymbol{H}}_m \sim \mathcal{CN}\left(0, 1\right). \tag{6.3}$$

Furthermore, cabling and transmitter hardware might introduce an additional element dependent phase shift φ_m. Specifically, uncalibrated arrays will exhibit some random φ_m.

The resulting radio channel coefficient for each antenna m where the mixture between specular and diffuse component is controlled by the $\mathcal{K}$-factor follows:

$$\boldsymbol{H}_m = \left(\sqrt{\frac{\mathcal{K}}{1+\mathcal{K}}}\bar{\boldsymbol{H}}_m + \sqrt{\frac{1}{1+\mathcal{K}}}\tilde{\boldsymbol{H}}_m\right)\exp\left(-j\varphi_m\right). \tag{6.4}$$

The amplitude of each element in $\boldsymbol{H}$ is Rician distributed with probability density function (PDF) [13]:

$$f^{\mathrm{A}}(x) = \frac{2x}{\tilde{P}}\exp\left(-\frac{x^2+\bar{P}}{\tilde{P}}\right)I_0\left(\frac{2x\sqrt{\bar{P}}}{\tilde{P}}\right) \quad x >= 0 \tag{6.5}$$

where I_0 is the modified Bessel function of the first kind. The PDF of the power gain is accordingly:

$$f^{\mathrm{P}}(x) = \frac{1}{2\sqrt{x}}f_A(\sqrt{x}) \tag{6.6}$$

The Rayleigh case ($\mathcal{K} = 0 \Rightarrow \bar{P} = 0, \tilde{P} = 1$) leads to the simplified equations:

$$f^{\mathrm{A}}(x) = 2x \exp\left(-x^2\right), \quad f^{\mathrm{P}}(x) = \exp\left(-x\right) \tag{6.7}$$

with the latter taking the form of the PDF of a normalised exponential distribution. The corresponding cumulative density function (CDF) is:

$$F^{\mathrm{P}}(x) = 1 - \exp\left(-x\right) \tag{6.8}$$

Eventually, $\boldsymbol{H}$ can be seen as complex normal random vector with

$$\boldsymbol{H} \sim \mathcal{CN}\left(\sqrt{\frac{\mathcal{K}}{1+\mathcal{K}}} \exp\left(-j\left(\mathbf{r}\boldsymbol{k} + \boldsymbol{\varphi}\right)\right), \mathbf{C}\right) \tag{6.9}$$

where the matrix $\mathbf{r}$ collects all M antenna element positions and the matrix $\mathbf{C}$ describes their correlation. Taking $\mathbf{C} = \frac{1}{1+\mathcal{K}}\mathbf{I}$ where $\mathbf{I}$ is the $M \times M$ identity matrix describes a spatially uncorrelated diffuse component.

Considering a uniform linear array (ULA) with a progressive phase shift in dependence of the incidence angle θ and element spacing of $\lambda/2$ between the elements specialises Eqn. (6.2) to:

$$\bar{\boldsymbol{H}}_m = \exp\left(-j\pi m \sin\theta + \varphi_m\right) \tag{6.10}$$

where the element dependent phase shift is considered.

6.3.3 Beam Sweeping Strategies

Maximum BS output power can be achieved by setting each single transmitter to its maximum. This transmit strategy resembles the receive strategy of equal gain combining. To allow for comparison of different numbers of antennas $||\boldsymbol{W}||$ needs to be normalised to unity. Hence, $|\boldsymbol{W}_m| = 1/M$ and the phase of each weight remains as free variable.

The simplest case is one fixed set of weights corresponding to a single beam pattern. Better strategies involve B sets of weights to scan the M-dimensional subspace. A $M \times B$ beam sweeping matrix $\mathbf{B}$ can be constructed by stacking column vectors that represent a distinct beam pattern each. A full scan of the subspace is achieved with M orthogonal beam pattern. Having an orthogonal beam sweeping matrix gives a lower bound for the power coupling: min $A = 1/M$.[1]

Using the identity matrix $\mathbf{I}$ (one active antenna per weight vector) to construct a beam sweeping matrix would lead to $\mathbf{B} = 1/M\mathbf{I}$. Unfortunately, this naive strategy is sub-optimal since a singe element is power restricted to $1/M$ of the BS sum power.

As a second option, Hadamard matrices, being orthogonal, can be employed to scan the full subspace using the full BS sum power. This strategy has been used as part of the Faros control channel design in the Argos testbed [55]. The last considered option is weights based on the discrete Fourier transform matrix.

Fig. 6.2 demonstrates the effect of Hadamard and Fourier weights on the beam pattern of a 4 element ULA with $\lambda/2$ spacing. Both have the same broadside and end-fire beam pattern but have differences for the intermediate ones. Fourier weights sweep the intermediate beam pattern achieving the maximum array factor, since they correspond to progressive phase shifts over the array. In contrast, Hadamard weights generate symmetric beams with respect to broadside, thereby reducing the maximum gain of the main lobe.

6.4 Statistical Framework

The following section describes the framework to analyse the synchronisation gain of the best beam pattern for an uncorrelated Rayleigh and Rice channel. The beam sweeping matrix $\mathbf{B}$ can be evaluated column-wise against the channel vector $\boldsymbol{H}$ with

$$\boldsymbol{S}_b = \left| \frac{\mathbf{B}_b^{\mathrm{H}} \boldsymbol{H}}{\|\mathbf{B}_b\|_2 \ \mathbb{E}\{\|\boldsymbol{H}\|_2\}} \right|^2 = \left| \frac{\mathbf{B}_b^{\mathrm{H}} \boldsymbol{H}}{\sqrt{M}} \right|^2 . \tag{6.11}$$

---

[1] Consider a M-dimensional subspace where $\mathbf{I}$ spans an orthogonal basis and take a one vector. The one vector projected on any column vector of $\mathbf{I}$ gives the minimal angle for any point in that subspace, since its equal for all column vectors. Hence, min $A = |< [1, 0, \ldots, 0]^{\mathrm{T}}, \mathbf{1} > |^2 / (\|[1, 0, \ldots, 0]^{\mathrm{T}}\|_2^2 \ \|\mathbf{1}\|_2^2) = 1/M$.

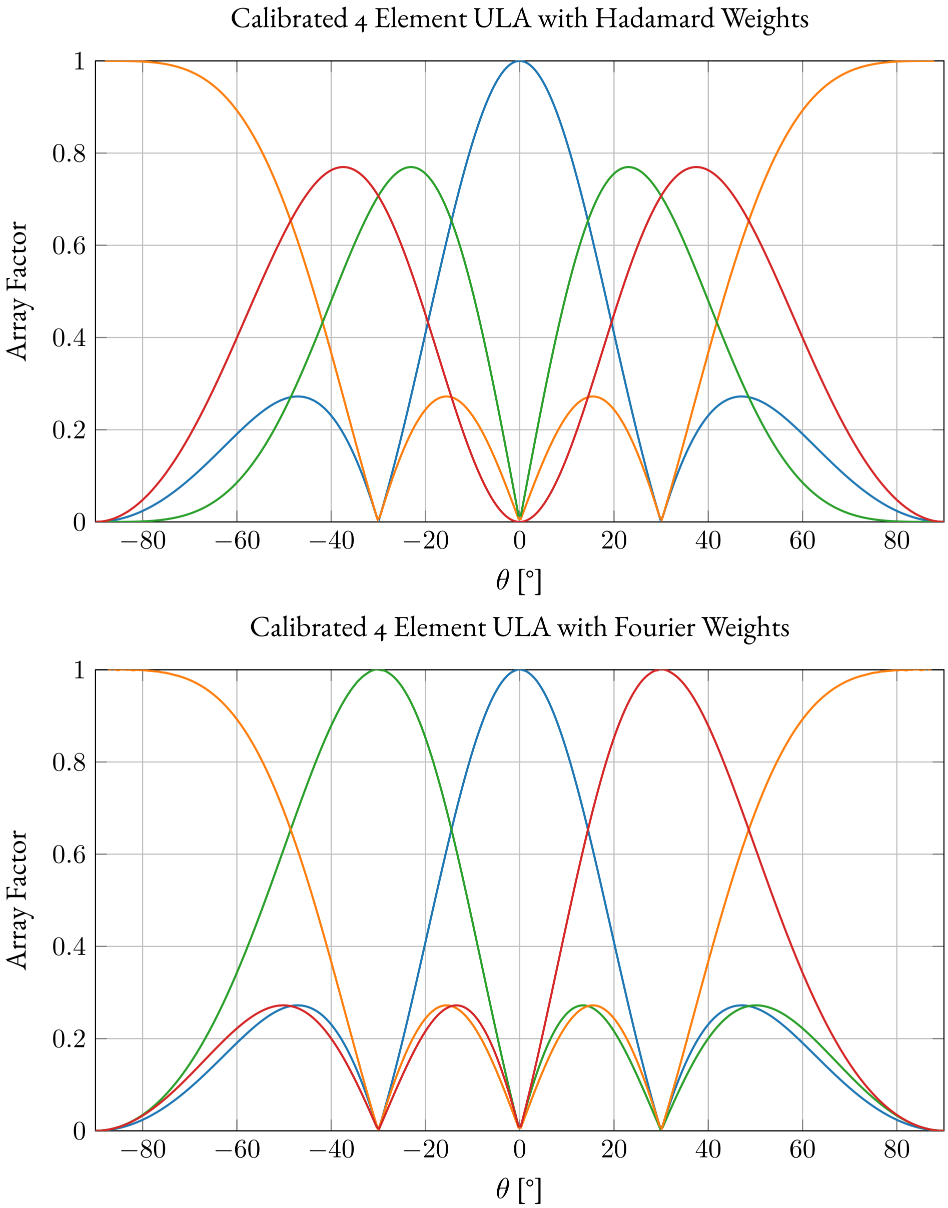

Calibrated 4 Element ULA with Hadamard Weights

Calibrated 4 Element ULA with Fourier Weights

Figure 6.2: Beam pattern for Hadamard and Fourier weights over a calibrated 4 element ULA with $\lambda/2$ spacing.

The expectation of the channel gain is $\mathbb{E}\{\|\boldsymbol{H}\|_2\} = \sqrt{M}$, because each element of $\boldsymbol{H}$ has unit expectation ($\bar{P} + \tilde{P} = 1$). Furthermore, $\|\mathbf{B}_b\|_2 = 1 \forall b$ for both Hadamard and Fourier weigths. The resulting synchronisation gain vector $\boldsymbol{S} = [\boldsymbol{S}_1, \boldsymbol{S}_2, \ldots, \boldsymbol{S}_b]^{\mathrm{T}}$ corresponds to the Hermitian angle α_b for the b-th beam pattern in Eqn. 6.1 as follows:

$$\boldsymbol{S}_b = \frac{\|\boldsymbol{H}\|_2^2}{M} \cos^2 \alpha_b = \frac{\|\boldsymbol{H}\|_2^2}{M} A_b. \tag{6.12}$$

Hence, $\boldsymbol{S}_b$ is influenced by the power coupling A_b and the in expectation normalised magnitude between a distinct beam pattern and the radio channel $\boldsymbol{H}$. Finding the distribution of the largest element in $\vec{S}$ allows characterisation of the statistical behaviour of the beam sweeping strategy for a given radio channel.

Describing the statistics of the best beam pattern for a specific channel resembles a selection combining problem where each branch corresponds to a column vector of $\mathbf{B}$. For selection combining, *order statistics* have been used to analyse the behaviour of the best branch [53], [54].

Order statistics describe random variables after a sorting process. Classically, independent draws from the same distribution are assumed, but the same principles can be applied to the elements of an independent and identically distributed (iid) random vector. Sorting all B elements in $\boldsymbol{S}$ by magnitude $\boldsymbol{S}_{1:B} \leq \boldsymbol{S}_{2:B} \leq \cdots \leq \boldsymbol{S}_{B:B}$ leads to $\boldsymbol{S}_{b:B}$ describing the synchronisation gain of the b-th best beam pattern. $\boldsymbol{S}_{B:B}$ is characterised by the maximum order statistic with PDF $f_{\boldsymbol{S}_{B:B}}$ and can be obtained from the PDF $f_{\boldsymbol{S}}$ and cumulative density function (CDF) $F_{\boldsymbol{S}}$ of the underlying iid element distributions [53]:

$$f_{\boldsymbol{S}_{B:B}}(x) = B \left[F_{\boldsymbol{S}}(x)\right]^{B-1} f_{\boldsymbol{S}}(x). \tag{6.13}$$

Eqn. (6.11) corresponds to an underlying matrix vector product that linearly transforms the random vector $\boldsymbol{H}$. Hence, the resulting vector is based on the following distribution [12, Theorem 2.8]:

$$\mathbf{B}^{\mathrm{H}} \boldsymbol{H} \sim \mathcal{CN}\left(\sqrt{\frac{\mathcal{K}}{1+\mathcal{K}}} \mathbf{B}^{\mathrm{H}} \exp\left(-j\left(\mathbf{r}\boldsymbol{k} + \boldsymbol{\varphi}\right)\right), \mathbf{BCB}^{\mathrm{H}}\right) \tag{6.14}$$

For the normalised Hadamard and discrete Fourier transform matrix, **B** is unitary. Therefore, the correlation of the uncorrelated diffuse component is unaffected under the linear transformation ($\mathbf{B}\frac{1}{1+\mathcal{K}}\mathbf{I}\mathbf{B}^{\mathrm{H}} = \frac{1}{1+\mathcal{K}}\mathbf{I}$) and leads to:

$$\mathbf{B}^{\mathrm{H}}\boldsymbol{H} \sim \mathcal{CN}\left(\sqrt{\frac{\mathcal{K}}{1+\mathcal{K}}}\mathbf{B}^{\mathrm{H}}\exp\left(-j\left(\mathbf{r}\boldsymbol{k}+\boldsymbol{\varphi}\right)\right), \frac{1}{1+\mathcal{K}}\mathbf{I}\right). \tag{6.15}$$

The last relation simplifies even further in Rayleigh fading conditions

$$\mathbf{B}^{\mathrm{H}}\boldsymbol{H} \sim \mathcal{CN}\left(0, \mathbf{I}\right) \tag{6.16}$$

and shows that the elements of $\boldsymbol{S}$ are still iid after transformation for the uncorrelated Rayleigh fading case. Taking Eqns. (6.7), (6.8) and applying Eqn. (6.13) leads to the corresponding PDF and CDF for the order statistic of $\boldsymbol{S}_{L:L}$:

$$f_{\boldsymbol{S}_{B:B}}(x) = B\left[1-\exp\left(-xM\right)\right]^{B-1}\exp\left(-xM\right) \tag{6.17}$$

$$F_{\boldsymbol{S}_{B:B}}(x) = \int_0^{xM} f_{\boldsymbol{S}_{B:B}}(x')dx' = \left[1-\exp\left(-xM\right)\right]^{B}. \tag{6.18}$$

The Rician case is more challenging from a distributional point of view. The non-zero nature of the mean of the complex normal random vector means that Eqn. (6.13) can only be applied if

$$\sqrt{\frac{\mathcal{K}}{1+\mathcal{K}}}\mathbf{B}^{\mathrm{H}}\exp\left(-j\left(\mathbf{r}\boldsymbol{k}+\boldsymbol{\varphi}\right)\right) = d\mathbf{1}. \tag{6.19}$$

The mean vector in Eqn. (6.15) needs to be a one vector scaled by a constant d. This is generally not the case and different means lead to $\boldsymbol{S}$ not fullfilling the iid condition for classic order statistics. The discussion of order statistics for non-iid distributed random variables is out of scope for this study and needs to be considered for the theoretical treatment of radio channels with spatial correlation. Nonetheless, to show the behaviour of beam sweeping strategies in uncorrelated Rician fading, empirical CDFs are generated with Monte Carlo simulations. The incidence angle θ is uniformly distributed between zero and 2π, such that it is equally probable for a plane wave to arrive from all directions. Additionally, for the uncalibrated array all φ_m are assumed to be uniformly distributed between zero and 2π, whilst the calibrated array sets φ_m to 0.

6.5 Results

Having established that the synchronisation gain can be described by order statistics, opens up for analysis of Rayleigh as well as Rice fading in both uncalibrated and calibrated BS arrays.

6.5.1 Rayleigh Fading

Interpretion of Eqn. (6.16) allows insight into orthogonal beam sweeping in the uncorrelated Rayleigh fading case. The specific choice of the beam sweeping matrix is irrelevant as long as $\mathbf{B}$ is unitary. Furthermore, there is no difference between the calibrated and uncalibrated array case, as only diffuse scattering contributes to the synchronisation channel.

Plotting Eqn. (6.18) for different BS sizes in Fig. 6.3 displays the behaviour of the synchronisation gain for a growing number of antenna elements. In the upper plot is the array factor the same as 0 dB. Hence, the gain gap between the UE directed and the broadcast channel is highlighted. Even for a moderately sized 8 antenna BS, the expectation of the gain gap increases to about 4.7 dB. Furthermore, the gain gap is increasing with a growing number of BS antennas.

The lower plot uses the element factor as 0 dB reference. Hence, an 8 element BS will be illuminating the cell with about 4.3 dB gain over a single element BS if an orthogonal beam sweeping scheme is employed. This gain is diminishing fast and about 12500 BS antennas would lead to an expected gain of about 10 dB, if 12500 orthogonal beam pattern are illuminated.

Uncorrelated Rayleigh fading could arise in industrial internet of things environments. Here, the synchronisation gain is not of high importance since cell size

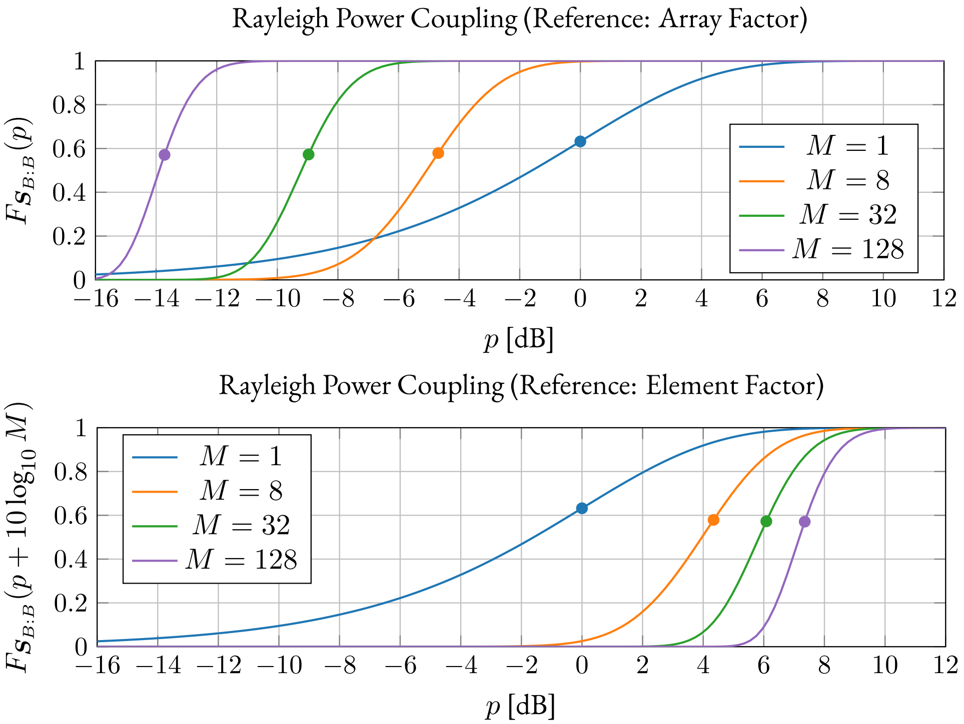
Rayleigh Power Coupling (Reference: Array Factor)

Rayleigh Power Coupling (Reference: Element Factor)

Figure 6.3: CDFs of the best beam power coupling under Rayleigh fading conditions for an orthogonal beam sweeping strategy. The upper plot shows the coupling with reference to the maximum array factor and the lower plot includes the array factor to reference the result to the element factor. The dot in the CDFs indicates the expectation.

stays constant and the spatial multiplexing gain of large scale antenna systems is paramount. Furthermore, the lacking necessity of array calibration could reduce the BS implementation costs.

6.5.2 Rician Fading

Resorting to Monte Carlo simulations for a 32 antenna BS with 100000 realisations gives insight into the gain gap behaviour for different $\mathcal{K}$-factors. The simulated $\mathcal{K}$-factor of −100 dB links the results back to the Rayleigh case.

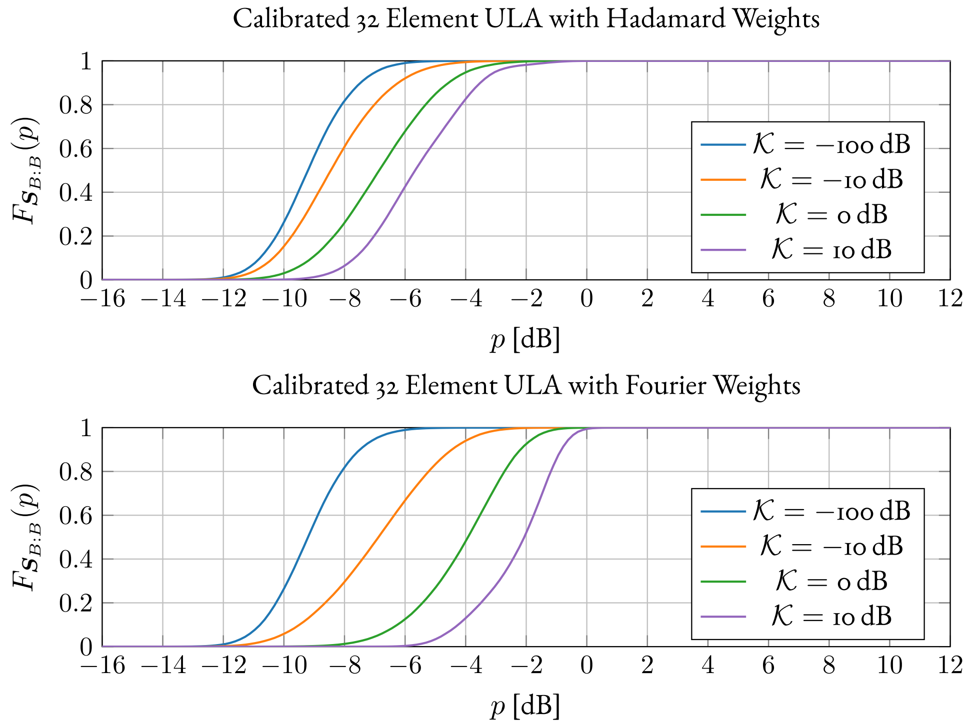

Figure 6.4: Simulated empirical CDFs of the best beam power coupling under Rician fading conditions for an orthogonal beam sweeping strategy and a calibrated antenna array. The upper and lower plots the coupling with reference to the maximum array factor for Hadamard and Fourier weights, respectively.

Calibrated Arrays

Having a calibrated array allows to steer the beam towards the direction of the specular component, thereby reducing the gain gap. Fig. 6.4 shows that Fourier weights are better suited to illuminate the Rician channel efficiently. Even for a specular component being 10 dB weaker than the diffuse component, the gain gap is reduced.

Hadamard weights for beam sweeping are a suboptimal choice for the Rician channel, since most beam pattern have multiple coherent beams whereas for Fourier weights all beam patterns keep at least one beam with maximum array factor.

Uncalibrated Arrays

Considering uncalibrated arrays, it becomes impossible to illuminate the direction of the specular component, since the phases for coherent superposition are unknown. Hence, the maximum order statistic approaches, without dependence on the $\mathcal{K}$-factor, the Rayleigh solution depicted in Fig. 6.3. Fig. 6.5 shows the simulation results for both Hadamard and Fourier weights. All of them coincide with the result of the uncorrelated Rayleigh channel ($\mathcal{K} = -100$ dB in Fig. 6.5). Again, the specific choice of the orthogonal beam matrix has no impact any longer, since the coherent sums are broken up by the random phases.

Small angular spread and Rician fading is more likely to appear in outdoor scenarios when the BS antenna is high above the ground. If the cell size is supposed to grow due to the usage of large scale antenna systems, calibration of the array becomes necessary and Fourier weights, offering improved pointing in space, give better results. Otherwise, the gain gap grows equally fast as in an uncorrelated Rayleigh fading environment.

6.6 Discussion

UEs need to acquire some synchronisation information from the BS before they can transmit uplink pilots. This synchronisation channel will naturally diverge from the channel that is subsequently estimated in the uplink. The resulting gain gap increases with a growing number of BS antennas and limits the service area of a cell.

Still, the synchronisation gain can grow slightly if a full subspace scan is performed. In Rayleigh fading environments, array calibration is unnecessary as long as the diffuse power is undergoing a large angular spread with low antenna correlation. In Rician environments, the gain gap can be reduced by traditional beamforming

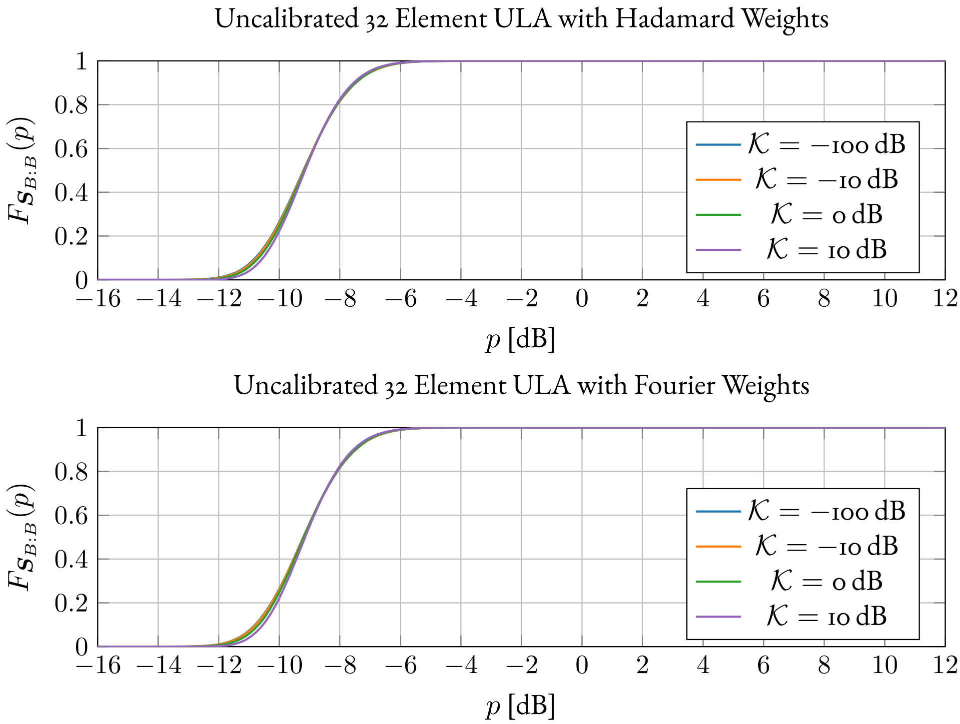

Figure 6.5: Simulated empirical CDFs of the best beam power coupling under Rician fading conditions for an orthogonal beam sweeping strategy and an uncalibrated antenna array. The upper and lower plots the coupling with reference to the maximum array factor for Hadamard and Fourier weights, respectively.

using Fourier weights. The penalty for an uncalibrated array is the unability to exploit the specular component to increase the synchronisation gain. The specular component is mixed by the random phases and contributes as additional diffuse Gaussian component for a large enough array size. Hence, the calculations for the Rayleigh environment become valid again.

A correlated diffuse component of the radio channel correspond to some directionality. It is expected that a calibrated array becomes necessary to direct the synchronisation signal controlled into the right direction. Fourier weights might lose their advantage over Hadamard weights if multiple directions are necessary to optimally illuminate a UE position.

6.7 Conclusion

The gap between the synchronisation gain in a broadcast channel and the optimally available array gain for a UE directed channel is growing with the number of BS antennas. To alleviate the gain gap, beam sweeping can be used. In this study, Hadamard and Fourier antenna weights have been considered for an ULA to analyse the effect of BS antenna scaling.

The derived analytical PDF and CDF of the synchronisation gain for uncorrelated Rayleigh fading for any orthogonal beam sweeping matrix can be directly used to quantify the severity of the gain gap.

The gain gap in uncorrelated Rician fading can be reduced by usage of Fourier weights if a calibrated array is available. Hadamard weights are less useful, since they lead to beam pattern that do not realise the full array factor.

The synchronisation gain has been neglected in most massive MIMO considerations and restricts the service area of a BS and subsequently the size of the BS antenna array. Even for moderately sized systems, more thought should be spend on the spatial coverage of the broadcast channel.

7 Paper C3: Fading Margins for Large-Scale Antenna Systems

Authors	J. Abraham and T. Ekman
Conference	IEEE International Conference on Communications
Place	Montreal, Canada
Date	June, 2021
Original-URL	`https://ieeexplore.ieee.org/document/9500328`
DOI	10.1109/ICC42927.2021.9500328
arXiv	2102.09903

Changenotes

- Notation
    - $\mathcal{E}\left\{\cdot\right\}$ changed to $\mathbb{E}\{\cdot\}$
    - $\mathcal{V}\left\{\cdot\right\}$ changed to $\mathbb{V}\{\cdot\}$
- clarification of the median gain as reference in (7.1)
- normalisation enforces unit gain of the BS output power

7.1 Abstract

Mobile phone operators have begun the roll-out of 5G networks, deploying massive MIMO base stations. Commercial product ranges start with 16 independent radio chains connected to a large-scale antenna system to exploit both channel hardening and favourable propagation in order to obtain increased spectral efficiency. In this work, the cumulative distribution function describing the gain for large-scale antenna systems considering spatial and spectral diversity is evaluated empirically in terms of a fading margin and compared to an analytical maximum

diversity reference system. This allows for a simple investigation of the trade-off between deployment size and exploitation of channel hardening. For the considered site-specific measurement data, little additional diversity is harvested with systems larger than 32 antenna elements.

7.2 Introduction

Massive MIMO has seen a lot of development since its conceptual advent in 2010 [16]. During the last decade, both theoretical and experimental work have explored the limits of the approach. Nowadays, operators can acquire commercially available base stations that implement some version of massive MIMO.

A more contemporary view of massive MIMO including a proper definition of a massive MIMO cellular network is provided in [8]. Additionally, the authors highlight the fact that most literature has only considered spatially uncorrelated radio channels due to mathematical tractability. Unfortunately, this approach neglects important aspects of the physical reality, which can lead to misleading conclusions.

Some attempts at building and using channel sounders and testbeds have been made to measure radio channels in some specific environments, e.g. [61], [80]. This work uses datasets of a large measurement campaign from 2016 [44] for practical demonstration.

In the following manuscript, we will present the connection between a link budget fading margin and channel hardening for an increasing number of antennas. Only a single user is considered[1] to investigate the best case without complication caused by MUI. This explores an additional way of determining the scaling for large-scale antenna systems in addition to the work in [C1], [19], [40].

First, an ECDF based fading margin is introduced, giving a measurement-based figure of merit in standard radio engineering terms. Second, a maximum diversity

---

[1] A single user implies a reduction to a MISO / single-input multiple-output (SIMO) system.

reference channel is formed with an N-tap PDP for independent base station antennas in a single user setting. The final section presents an empirical procedure to evaluate the obtained channel hardening (spatial and spectral diversity) which both shows the actual scaling and highlights the difference to the uncorrelated reference channel. Since the procedure shows the diminishing returns explicitly, it allows to assess the useful amount of antenna elements from a diversity perspective at a specific site.

7.3 Fading Margin

The fading margin describes the excess amount of power that a link budget has to provide to counteract fading events due to multipath propagation. It is in the interest of the radio engineer to reduce the required excess power to optimise a radio link. This reduction is beneficial due to energy savings and reduced system interference.

Large-scale antenna systems with phase steered beams, as used by massive MIMO systems, have multiple advantages compared to single antenna systems. The directional gain is increased due to the array factor, whereas fading is less severe due to low probability that all antenna elements experience fading at the same time (channel hardening). Moreover, inter-system interference (favourable propagation) as well as interference with other systems is reduced due to spatio-temporal focusing of power.

To study the channel hardening scaling behaviour, we use a fading margin $F_M(p)$ in logarithmic units for probability p, defined by

$$F_M(p) = 10 \log_{10} \left(\frac{Q(0.5)}{Q(p)} \right), \tag{7.1}$$

where $Q(p)$ is the quantile function or inverse CDF with corresponding CDF $F(x)$ such that:

$$Q(F(x)) = x. \tag{7.2}$$

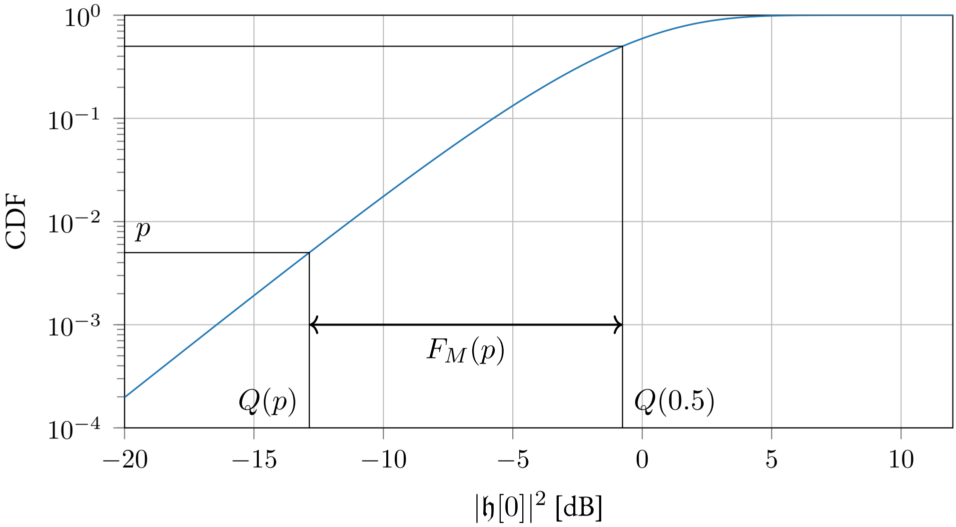

Figure 7.1: The fading margin $F_M(p)$ is defined with help of the CDF of the channel gain. This example visualises $F_M(p = 5 \times 10^{-3}) = 12.1$ dB covering the fading between the median effective channel gain at $Q(0.5)$ and the target outage channel gain at $Q(p = 5 \times 10^{-3})$.

Furthermore, this fading margin is invariant to the array factor, which allows for comparison between different numbers of antenna elements. The connection between this fading margin and the CDF of the gain is visualised in Fig. 7.1. The steeper the CDF the smaller becomes the fading margin.

Other definitions of a fading margin have been used in the literature. The author of [81] motivates a fading margin as the difference between a fading channel and an additive white Gaussian noise channel, whereas [82] exchanges the median in (7.1) with the expected value of the channel gain as reference to calculate the fading margin. By using the median gain as reference in (7.1), a fading margin $F_M(p = 0.5) = 0$ dB leads to half of the realisations falling short of and the other half exceeding it. Furthermore, this fading margin can easily be extracted from ECDFs and does not require any channel model. In case of a symmetrical underlying fading distribution, both median and mean coincide.

7.4 Channel Hardening

After showing the fading margin, this section uses a tapped delay line model for the channel to explore channel hardening in both the spectral and spatial domain. Time-reversal precoding [11] is applied to a maximum diversity reference channel.

Following an input-output description of a massive MIMO system in the downlink [C1] and specialising it to the single user case gives:

$$y[n] = \sqrt{\beta}\,\mathfrak{h}[n] \star x[n] + e[n] \tag{7.3}$$

with symbols representing:

- $\sqrt{\beta}$ - large-scale fading,
- $\mathfrak{h}[n]$ - effective downlink channel,
- $x[n]$ - transmitted signal,
- $y[n]$ - received signal,
- $e[n]$ - additive noise,
- n - time index.

The large-scale fading coefficient can be estimated with the sample mean from raw channel measurements over a coherent block of base station antennas, channel taps and timestamps. The effective channel $\mathfrak{h}[n]$ is constituted by the sum of contributions from each antenna:

$$\mathfrak{h}[n] = \sum_{m=1}^{M} h_m[n] \star w_m[n] \tag{7.4}$$

convolving $h_m[n]$ and $w_m[n]$, being the uplink channel taps and precoding filter for antenna m, respectively. In this paper we consider the commonly used time reversal weights for precoding, normalized to enforce unit gain of the base station output power :

$$w_m[n] = \frac{h_m^*[-n]}{\sqrt{\sum_{m=1}^{M} \sum_{n=1}^{N} |h_m[n]|^2}}, \tag{7.5}$$

where M and N are the number of base station antennas and the number of taps of the tapped delay line model, respectively.

Under the assumption of uncorrelated effective channel taps, the instantaneous SINR is:

$$\gamma[n] = \frac{|\mathfrak{h}[0]|^2}{\sum_{l=-N,l\neq 0}^{N} |\mathfrak{h}[l]|^2 + \frac{1}{\Gamma}} \tag{7.6}$$

where $\Gamma = \beta P_x / P_e$ is the mean SNR for transmit power P_x and noise power P_e. The interference term consists only of ISI (derivation see appendix 7.A). For a multiuser MIMO discussion, the MUI would need to be added to the denominator.

The instantaneous SINR is proportional with the numerator, showing the central role of the zero-delay tap $\mathfrak{h}[0]$ of the effective channel. The ISI is captured in the off-centre taps of the effective channel in the denominator, as well as the noise influencing the mean SNR. As expected, low SNR will lead to the noise limitation of the SINR, whilst high SNR gives the interference limited regime.

It should be noted that the off-centre taps add up non-coherently, whilst $\mathfrak{h}[0]$ results from a coherent addition. Hence, the offset between them is growing with an increasing number of independent base station antennas [J1].

Solving the convolution in (7.4) for the zero-delay results in

$$\mathfrak{h}[0] = \sqrt{\sum_{m=1}^{M} \sum_{n=1}^{N} |h_m[n]|^2}. \tag{7.7}$$

Hence, both independent taps and antennas are increasing the instantaneous SINR, where the number of taps is given by the propagation environment and bandwidth, whereas the number of antennas can be adjusted to improve the link.

To explore the scaling of the fading margin with respect to the number of antennas, an artificial reference channel can be considered. The best case from a diversity perspective would be an N independent tap channel with equal mean tap power $(1/N)$. This ensures unit gain and is in line with $\sqrt{\beta}$ capturing large-scale fading. For a rich scattering environment, these channel taps can be modelled by complex normal random variables with Rayleigh distributed amplitudes. Note, that N represents the spectral diversity of the radio environment.

Both independent taps and independent antennas contribute in the same manner to $\mathfrak{h}[0]$. The power gain $|\mathfrak{h}[0]|^2$ of the zero-delay effective channel tap is a sum over independent squared Rayleigh variables. Squared Rayleigh distributed random variables are exponentially distributed and their sum is Gamma distributed [77] with shape MN (as each tap per antenna contributes) and scale $1/N$:

$$|\mathfrak{h}[0]|^2 \sim \Gamma(MN, 1/N). \tag{7.8}$$

It follows that the squared zero-delay tap of the effective channel has mean M and variance M/N:

$$\mathbb{E}\{|\mathfrak{h}[0]|^2\} = M \tag{7.9}$$

$$\mathbb{V}\{|\mathfrak{h}[0]|^2\} = \frac{M}{N}. \tag{7.10}$$

We can show that the Gamma distribution fulfils the condition for channel hardening by inserting it into [19, Eqn. (2.17)]. Evaluation of this squared coefficient of variation:

$$\frac{\mathbb{V}\{|\mathfrak{h}[0]|^2\}}{\left(\mathbb{E}\{|\mathfrak{h}[0]|^2\}\right)^2} = \frac{1}{NM} \tag{7.11}$$

shows convergence towards zero for a growing number of antennas or channel taps. The authors of [19] state that a squared coefficient of variation order of 10^{-2} or smaller is enough to obtain hardening in an uncorrelated setting. Hence, the effective channel can exhibit channel hardening with 4 taps and 32 antenna elements at the base station. Unfortunately, (7.11) is not offering an easily interpretable quantification of channel hardening. This gap can be filled with the fading margin approach, as shown in the rest of the manuscript.

Fig. 7.2 shows a few CDFs demonstrating the increasing steepness, giving a reduced fading margin, for growing number of antennas and taps. The two lines corresponding to $MN = 4$ exhibit the same steepness and diversity.

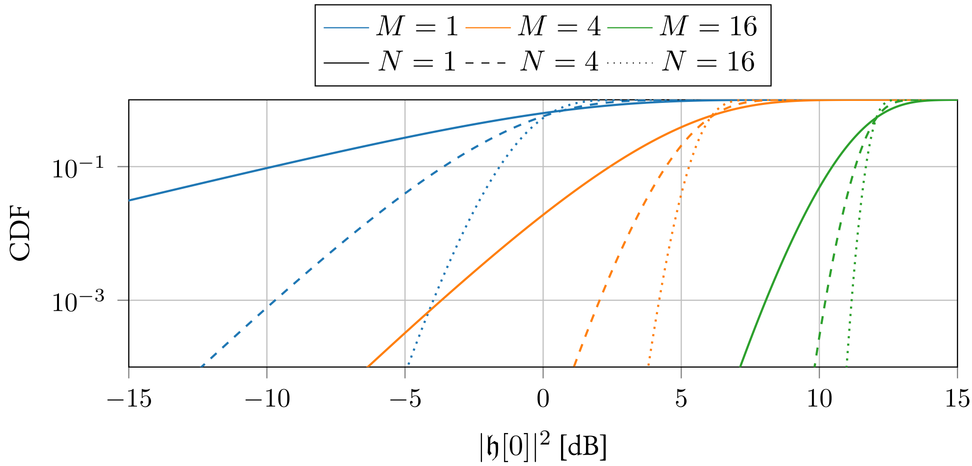

Figure 7.2: Analytical CDFs for a few configurations of the N-tap reference channel and an uncorrelated M element antenna array. The colour indicates the number of antennas and the line style the number of channel taps. Both spectral and spatial aspects contribute to the steepness of the curve (diversity), but only antenna elements improve the array gain. E.g. the $M = 4$, $N = 1$ configuration shows the same outage probability as the $M = 1$, $N = 4$ configuration offset by the array gain.

Returning to the question how additional antennas in a large-scale antenna system can improve the fading margin, Fig. 7.3 shows the fading margin (7.1) versus degrees of freedom (MN) for different probabilities. Taking a two tap channel for a single antenna system as a reference, gives a fading margin of about 30.7 dB to achieve an ultra-reliable outage probability of 10^{-6}. Exploitation of channel hardening with 10 and 30 independent antennas would reduce the required fading margin ideally to 5.6 dB and 3.0 dB, respectively. For later comparison to measurement data, fading margins for 10^{-3} are tabulated in Table 7.1. It is obvious that the addition of more antennas has diminishing effects on the fading margin, whilst the array gain grows linearly. The latter comes at the price of increased complexity for broadcast applications and user synchronisation, as we recently discussed in [C2]. The presented improvement of the fading margin is the best case result, since the model is based on independent antennas and uncorrelated channel taps for each antenna. Real world systems would not see those improvements to the full extent. Nonetheless, the qualitative behaviour helps to assess how many antennas are needed to improve the fading margin at a specific site.

To summarise, the behaviour of the fading margin caused by channel hardening for a changing number of base station antennas can be modelled for a tapped delay line massive MIMO channel. Applying time-reversal precoding and relating the effective zero-delay channel coefficient to the instantaneous SINR in the low average SNR regime under consideration of a rectangular reference channel, gives the best case for the evolution of the fading margin. The actual fading margin in real world systems needs to be higher than the best case, due to spatial correlation, ISI and the reduced frequency diversity of non-rectangular non-Rayleigh channels. Still, the system designer gets valuable insight into the scaling behaviour for base station antennas with respect to channel hardening.

7.5 Case Study

Considering that a large-scale antenna system at a specific site is supposed to be optimised, how to analyse the potential impact on the fading margin based on single antenna element measurements? Ultimately, how many independent radio chains should the system support before the advantages are diminishing? The general procedure for uncorrelated antennas is the following:

1. Take single antenna multi carrier measurements over the array, spanning the largest deployable system on that site.
2. Estimate a large-scale fading coefficient $\sqrt{\beta}$ for the base station and normalise the measurement data accordingly.
3. Form an effective channel zero-delay tap $\mathfrak{h}[0]$ for each antenna position to determine the single element reference ECDF.
4. Form the effective channel for the array configurations in question.
5. Evaluate the different fading margins for the sub-arrays to get an indication how large the optimised antenna array needs to be for a certain reliability requirement.

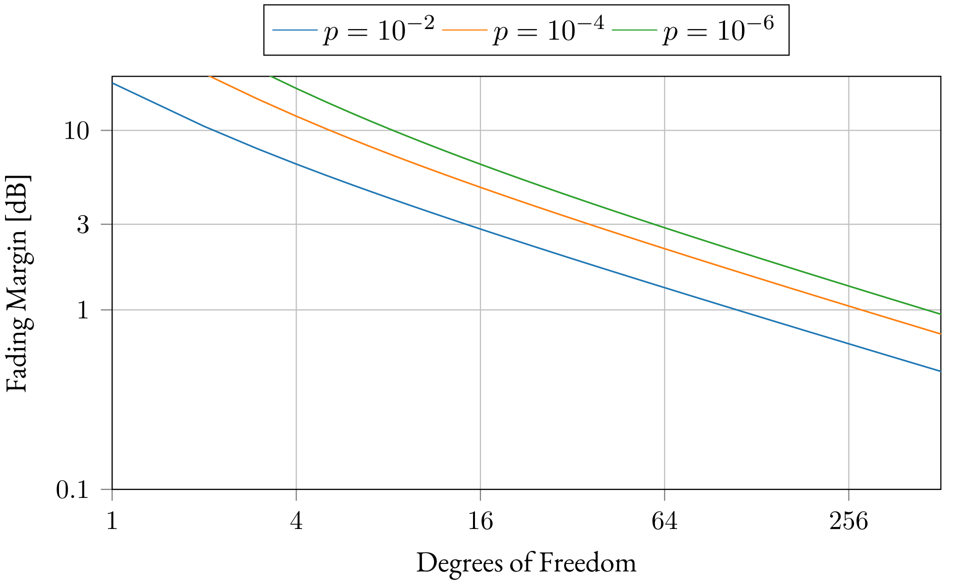

Figure 7.3: Analytical fading margins for three different probabilities for the rectangular N-tap Rayleigh channel and M independent antenna elements with MN degrees of freedom. Qualitatively, the first few degrees of freedom improve the fading margin massively while additional ones have a reduced impact.

Table 7.1: Analytical fading margins at a probability of 10^{-3} for the rectangular independent N-tap Rayleigh channel and M independent antenna elements. Increasing the degrees of freedom has diminishing returns.

$F_M(10^{-3})$	$M = 1$	$M = 2$	$M = 4$	$M = 8$
$N = 1$	28.41 dB	15.68 dB	9.33 dB	5.9 dB
$N = 2$	15.68 dB	9.33 dB	5.9 dB	3.88 dB
$N = 3$	11.47 dB	7.09 dB	4.6 dB	3.08 dB
$N = 4$	9.33 dB	5.9 dB	3.88 dB	2.62 dB

Table 7.2: Empirical fading margins for four different datasets [44] and different array configurations. The improvement of the fading margin, due to usage of spectral diversity, is diminishing for a growing antenna array.

	Fading Margin $F_M(10^{-3})$							
	Single Element		Array (8 ele.)		Array (32 ele.)		Array (93 ele.)	
Bandwidth Dataset	narrow	wide	narrow	wide	narrow	wide	narrow	wide
RICE A	28.75 dB	9.97 dB	7.77 dB	5.21 dB	5.58 dB	4.67 dB	4.99 dB	4.4 dB
RICE B	29.27 dB	13.39 dB	10.39 dB	7.91 dB	8.84 dB	7.66 dB	7.54 dB	5.84 dB
RICE C	28.88 dB	10.46 dB	7.81 dB	5.17 dB	5.29 dB	4.05 dB	4.42 dB	3.61 dB
RICE D	28.97 dB	12.71 dB	8.85 dB	7.07 dB	6.20 dB	5.25 dB	5.79 dB	4.84 dB

Four datasets from [44] are used to showcase the outlined investigation in both LOS and NLOS indoor environments, namely:

- RICE A[2] - 2.4 GHz - LOS environment,
- RICE B[3] - 2.4 GHz - NLOS environment,
- RICE C[4] - 5 GHz - LOS environment,
- RICE D[5] - 5 GHz - NLOS environment.

For each dataset, a channel trace for user one is extracted, considering 14000 timestamps and 52 subcarriers over 20 MHz bandwidth. A maximum of 93 antenna elements is used, since antennas 17, 33 and 68 were providing much lower average signals in some datasets.

Fig. 7.4 shows the ECDFs for the RICE A dataset. Considering single antenna elements on single subcarriers, shows that the ECDF has the same slope and diversity as a single Rayleigh tap channel ($\Gamma(1,1)$). The small offset in amplitude

---

[2] Dataset: `ArgosCSI-96x8-2016-11-04-04-18-58_2.4GHz_continuous_mob_LOS`

[3] Dataset: `ArgosCSI-96x8-2016-11-04-05-57-41_2.4GHz_continuous_mob_NLOS`

[4] Dataset: `ArgosCSI-96x8-2016-11-03-06-10-35_5GHz_continuous_mobile_LOS`

[5] Dataset: `ArgosCSI-96x8-2016-11-03-04-36-53_5GHz_continuous_mob`

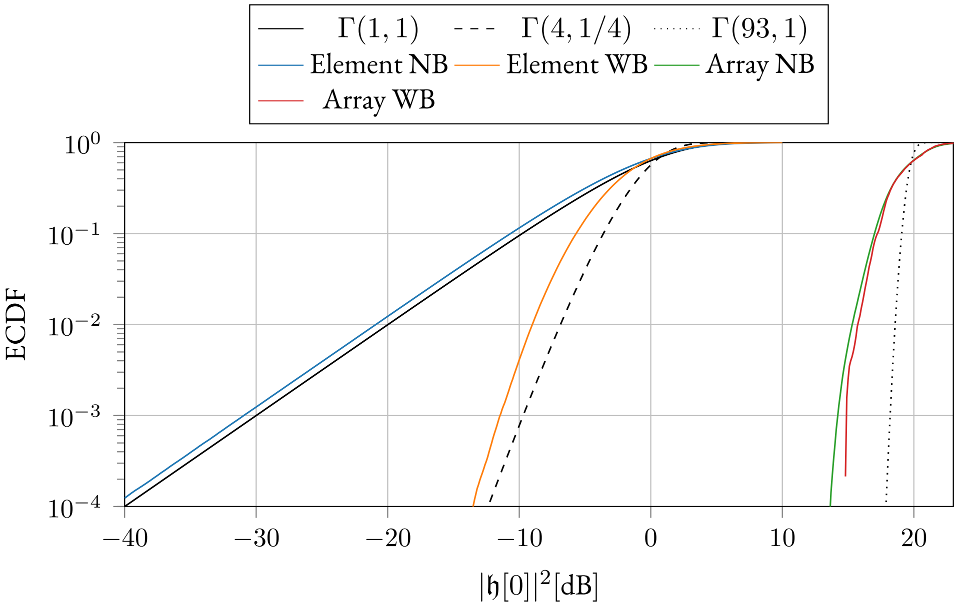

Figure 7.4: The ECDFs for the 'RICE A' dataset (2.4 GHz, continuous mobility of user 1, 14000 timestamps) show the probabilities of the coherent channel gain for four different configurations. The single antenna narrowband configuration follows the behaviour of a single tap Rayleigh channel very closely, whilst both full array configurations with 93 antennas fall even short of the single tap 93 antenna element model. This can be caused by spatial correlation reducing the harvested spatial diversity.

for the lower tail might arise from the assumption that all timestamps for each antenna and subcarrier belong to the same large-scale fading region.

Considering the wideband channel over single elements improves the fading margin and shows a steeper slope for the lower tail of the distribution. Here, only spectral diversity is exploited and the offset between narrow- and wideband shows a large improvement of 18.78 dB at a probability of 10^{-3}. The wideband channel behaves similar to a reference channel with 4 taps ($\Gamma(4, 1/4)$) with a slightly larger offset.

Investigation of the full array for both cases shows that the spectral degrees of freedom play a reduced role as the spatial degrees of freedom kick in. The full array wideband and narrowband cases exhibit almost equally steep ECDFs. Hence, the spectral diversity is consumed by the usage of spatial diversity. The ECDFs fall short of the fading margin behaviour for a 93 degrees of freedom reference channel and are closer to 12 degrees of freedom. The loss in fading margin at probability 10^{-3} of 2.9 dB could be due to correlated antennas.

Table 7.2 tabulates the fading margins for the named cases and intermediate array sizes. For the RICE A dataset, there is almost no improvement between 32 element antenna arrays and the full 93 antenna array. (NB, the larger arrays provide fewer realisations for the ECDFs and should be interpreted carefully.)

None of the four datasets are achieving the theoretical fading margin of 1.47 dB at 10^{-3} probability for 93 independent antenna elements and a single tap reference channel. This indicates that the employed array is subject to non-diminishing spatial correlation. The 5 GHz traces show slightly better fading margins, most likely due to the increased antenna element distance of about one wavelength and lower antenna correlation.

The system improvements for a 93 element array over the 32 element arrays are mainly due to an increased array gain and less due to increased channel hardening. The trade-off between base station complexity and performance should take this observation into account. For the particularly highlighted measurements, distributing 32 antenna elements over the available array size appears to be a good compromise between the number of radio chains and the exploitation of channel hardening. A potential extension to the current work is the analysis of permutations over the available antenna elements to give better performance than the usage of smaller and dense sub-arrays.

7.6 Conclusion

This paper has provided a definition of an alternative fading margin and used it to evaluate channel hardening in large-scale antenna systems. A reference channel based on a rectangular N-tap Rayleigh PDP demonstrates the ideal scaling behaviour for independent antenna elements under the most diverse channel conditions. Measured channels of arrays can be easily used to evaluate site-specific diversity in both the spatial and spectral domain. This gives system designers a tool to trade available diversity with system complexity by accounting for the number of independent radio chains.

The 20 MHz indoor channel measurements at 2.4 GHz and 5 GHz show little difference in the fading margin between narrow- and wideband channels for large-scale antenna arrays. An analysis of channel hardening in a system with 32 (correlated) antenna elements shows almost the same performance as that of a 93 element array. The fading margin shows diminishing returns with increasing number of antennas.

The investigation highlights that the diversity gains, measured using the fading margin at specific sites, can be evaluated with a relatively simple protocol.

7.A Instantaneous Effective Channel SINR

The instantaneous SINR for the effective channel $\gamma[n]$ with respect to the average SNR $\Gamma = \beta\frac{P_x}{P_e}$ for powers $P_x = \mathbb{V}\{x[n]\}$ and $P_e = \mathbb{V}\{e[n]\}$ as variance of the transmit signal and noise signal, respectively, can be derived from (7.3) by taking the expectation over both signals as in (7.12). Here, intended signal, ISI and noise have been isolated for uncorrelated effective channel taps allowing to define the SINR as in (7.13).

$$\begin{aligned}\mathbb{E}\{|y[n]|^2\} &= \mathbb{E}\Big\{\Big|\sqrt{\beta}\,\mathfrak{h}[n] \star x[n] + e[n]\Big|^2\Big\} \\ &= \beta\,|\mathfrak{h}[0]|^2\,P_x + \beta\sum_{l=-N,l\neq 0}^{N}|\mathfrak{h}[l]|^2\,P_x + P_e \qquad (7.12)\end{aligned}$$

$$\begin{aligned}\gamma[n] &= \frac{\beta\,|\mathfrak{h}[0]|^2\,P_x}{\beta\sum_{l=-N,l\neq 0}^{N}|\mathfrak{h}[l]|^2\,P_x + P_e}\\ &= \frac{\Gamma\,|\mathfrak{h}[0]|^2}{\Gamma\sum_{l=-N,l\neq 0}^{N}|\mathfrak{h}[l]|^2 + 1}\\ &= \frac{|\mathfrak{h}[0]|^2}{\sum_{l=-N,l\neq 0}^{N}|\mathfrak{h}[l]|^2 + \frac{1}{\Gamma}}. \qquad (7.13)\end{aligned}$$

8 Paper C4: Local Diversity and Ultra-Reliable Antenna Arrays

Authors	J. Abraham and T. Ekman
Conference	55th Asilomar Conference on Signals, Systems and Computers
Place	Pacific Grove, United States
Date	November, 2021
arXiv	`https://arxiv.org/abs/2108.00712`

8.1 Abstract

Ultra-reliable low-latency communication enables new use cases for mobile radio networks. The ultra-reliability (UR) regime covers outage probabilities between 10^{-9} and 10^{-5}, obtained under stringent latency requirements. Characterisation of the UR-relevant statistics is difficult due to the rare nature of outage events, but diversity defines the asymptotic behaviour of the small-scale fading distributions' lower tail. The UR-relevant regime in large-scale antenna systems behaves differently from the tail. We present the generalising *local diversity* at a certain outage probability to show this difference clearly. For more than four independent antenna elements, the classic diversity overestimates and underestimates the slope of the cumulative density function for weak and strong deterministic channel components, respectively.

8.2 Introduction

One of the reoccurring promises in both 5G and sixth generation mobile networks (6G) specifications is URLLC. The URLLC requires an outage probability of 10^{-5} or better within a 1 ms transmission period in 5G [83]. The authors of [56] introduce the terminology of *UR-relevant statistics* for outage probabilities below 10^{-5}. It can be expected that the requirements for 6G will be even more stringent. Hence, we will consider outage probabilities between 10^{-9} and 10^{-5} as the *UR-relevant regime*.

Generally, the allowed latency can be used to retransmit a packet, if the original message did not reach its destination. By decreasing the permitted latency, only one-shot transmissions can ultimately fulfil the requirement because a retransmission would take too long. This type of requirement is typical in control-loop or event based applications, where the timing is critical. Alternatively, the age of information [84] can used as a design metric, where the state of a system is observed. Here, a non-successful transmission every now and then might be acceptable, since the system can cope with intermittent link failure.

Small-scale fading is one of the main reasons for link-loss in rich scattering environments. It can be counteracted with forward error correction (FEC), relying on the assumption that fading events are short enough with respect to the coded packet length. If the coherence time of the channel is longer than the latency requirement, alternative measures have to be used to overcome small-scale fading. Exploiting spatial diversity through massive MIMO can improve the link robustness due to channel hardening. This approach reduces the variation of the channel gain around its mean and hereby the outage probability. Recenctly, we have suggested to use a fading margin to characterise channel hardening [C3]. It describes the required excess gain to provide a certain outage probability at a chosen rate. Hence, the performance of an UR antenna array with varying number of antenna elements can be quantified clearly.

An additional caveat for URLLC is power limitation of users. Especially battery powered sensors in WSN should avoid retransmissions. In those cases, minimising the fading margin improves the energy efficiency and allows to meet UR target outage probabilities. Moreover, smaller fading margins reduce the interference levels for users of the same system and systems that share the same spectrum resource.

This outlines why large antenna arrays are a technically viable solution for narrowband URLLC without retransmission of packets. System level simulations based on a 3GPP channel model for a specific cell show promising results for a coherence interval based pilot strategy [85].

A fundamental question remains, how can we infer the system behaviour of events that barely ever happen? A neat approach is the characterisation of the lower tail of the CDF as an intermediate solution between parametric channel models and non-parametric models [86]. The lower tail of multiple common fading distributions follows a power law [56], which gives the possibility to relax the model assumption from a single distribution to a class of distributions. The power law approximation requires two parameters: an offset and the log-log slope of the CDF. E.g. the classic Rayleigh channel shows a well known slope of 10 dB per decade in the lower tail.

Furthermore, the outage probability in detection problems [87] for high SNR corresponds to the lower tail of the channel gain. Using the SNR emphasises the variation introduced due to the small-scale fading channel and avoids a dependency on a specific modulator and detector. Due to that correspondence, the log-log slope in the asymptotic lower tail reveals the diversity of the radio channel. We propose to evaluate the log-log slope at a specific probability, generalising it to the *local diversity*. Hence, for outage probabilities converging to zero it attains the classic diversity measure.

A dual slope behaviour in single antenna Rician fading channels with larger $\mathcal{K}$-factors has already been shown in [88]. For multi-antenna systems in both Rayleigh and Rician fading, the outage probability slope in the UR-relevant regime deviates from the classic diversity. Therefore, a power law approximation of the lower tail can not provide an accurate description of the CDF for massive MIMO systems.

Our main contribution is the local diversity to highlight that lower tail approximations do not cover the actual system behaviour in the UR-relevant regime. We motivate the usage of analytical tools to get insight into UR-relevant statistics in the next section, because the number of necessary observations for a reliable empirical approach is prohibitive for real world scenarios. An uncorrelated Rician multi-antenna fading environment is introduced in section 8.4. It's local diversity is derived to relate the classical diversity to the UR-relevant regime. This measure can be seen as the relative error of a power law approximation based on the asymptotic behaviour of the lower tail. New compact expressions for the CDF, PDF and local diversity in terms of the complementary Marcum-Q function are used to evaluate them for large scale antenna systems. We provide a comparison of multi-antenna systems in different Rician fading environments with respect to the fading margin in section 8.5, to discuss the scaling behaviour. Furthermore, sampling strategies to analyse the UR-relevant regime are outlined.

8.3 Predicting the Unpredictable?

Let us investigate ECDFs as non-parameteric model, to understand the value of parametric analytical models for UR-relevant statistics. Basically, the UR-relevant regime covers the behaviour of rare events that barely ever happen and the fewer assumptions necessary the more general is the solution. How many observations are necessary to reliably estimate the UR-relevant statistics without prior knowledge?

The Dvoretzky-Kiefer-Wolfowitz (DKW) inequality [89], [90] can be used to bound an R-sample ECDF with respect to the true underlying CDF leading to the error term ϵ with confidence ξ:

$$\epsilon = \sqrt{\frac{\ln \frac{2}{1-\xi}}{2R}}. \tag{8.1}$$

This error term is characterising an error floor for the ECDF at low probabilities. Taking $R = 10^6$ observations as example and aiming at a confidence of $\xi = 99\,\%$ gives an error term of 1.6×10^{-3}. The resulting upper bound of the ECDF for a true single-antenna Rayleigh fading channel is shown in Fig. 8.1. It can be seen that the ECDF in the UR-relevant regime would be much smaller than the error floor, rendering empirical estimation of outage probabilities below 1.6×10^{-3} practically useless.

The number of antenna elements in massive MIMO ranges from a few ten to a few hundred, that can provide potentially correlated parallel observations of the

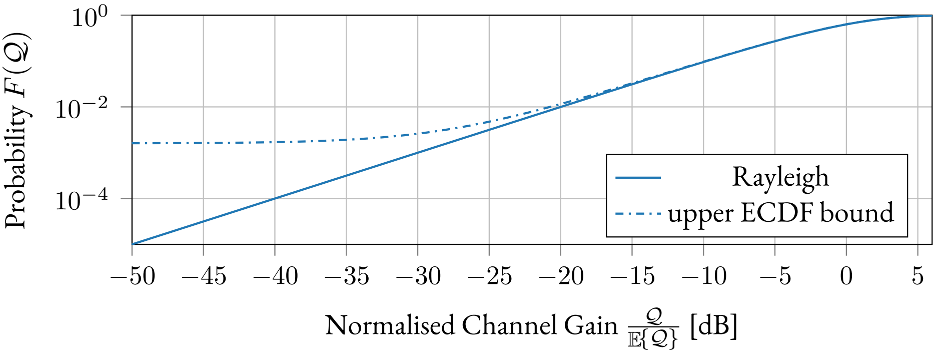

Figure 8.1: The CDF of a Rayleigh fading channel and an upper bound for an ECDF is shown. The error term in Eqn. (8.1) for a million observations and a confidence interval of 99 % is used as example, showing that the estimation of outage probabilities below 1.6×10^{-3} is unreliable.

radio channel. The remaining observations have to be gathered in a stationary time-frequency window to belong to the same underlying CDF. This is very unlikely in realistic scenarios, especially for high (environmental) mobility with limited temporal stationarity. Eventually, the characterisation of UR-relevant statistics in the lower tail is prone to large estimation errors for non-parametric models. Additionally, if energy efficient users are required, less spectrum may be used, reducing the number of samples in the spectral domain. Hence, the spatial domain sampling provided by an antenna array has to provide both the robustness of the system as well as a number of observations to estimate the CDF.

The large number of observations an obstacle even for simulations. Assuming that outage probabilities of 10^{-6} with confidence of 99.9999 % are of interest, on the order of 10^{13} observations have to be collected. Both, runtime and memory requirements of Monte Carlo simulations become cumbersome to get reliable results for the ECDF. Hence, only the analytic study of the UR-relevant regime has the possibility to give insight into trade-offs, as long as the model assumptions are not violated.

8.4 Rician Fading Channel Revisited

We will consider Rician fading channels with a Rician $\mathcal{K}$-factor and a diffuse power (gain) P_{dif}, following the parametrisation in [13]. The $\mathcal{K}$-factor describes the ratio between a deterministic component and the diffuse power of the radio channel. Hence, the mean power gain is $(\mathcal{K}+1)P_{\text{dif}}$.

To take M uncorrelated antennas at the base station into account, a complex random vector with mean $\sqrt{\mathcal{K}P_{\text{dif}}}\,[e^{j\varphi_1}, e^{j\varphi_2}, \cdots, e^{j\varphi_M}]^T$ and covariance $P_{\text{dif}}\mathbf{I}$ is constructed:

$$\boldsymbol{h} \in \mathbb{C}^M \sim \mathcal{CN}\left(\sqrt{\mathcal{K}P_{\text{dif}}}\left[e^{j\varphi_1}, e^{j\varphi_2}, \cdots, e^{j\varphi_M}\right]^T, P_{\text{dif}}\mathbf{I}\right). \tag{8.2}$$

The phases φ_m represent the phase front of the deterministic component with respect to the antennas and $\mathbf{I}$ is the $M \times M$ identity matrix. For Rayleigh fading ($\mathcal{K} = 0$), $\boldsymbol{h}$ is a circular-symmetric complex normal random vector $\boldsymbol{h} \sim \mathcal{CN}(0, P_{\text{dif}}\mathbf{I})$.

The effective channel $\mathcal{H}$ for a MRC weight vector $\boldsymbol{w}$ at the receiver results in:

$$\mathcal{H} = \boldsymbol{w}^{\mathrm{T}}\boldsymbol{h} = \frac{\boldsymbol{h}^{\mathrm{H}}\boldsymbol{h}}{\sqrt{\|\boldsymbol{h}\|_2^2}} = \sqrt{\sum_{m=1}^{M} |h_m|^2}. \tag{8.3}$$

The CDF $F(\mathcal{Q}; P_{\text{dif}}, \mathcal{K}, M)$ of the effective power gain $\mathcal{Q} = |\mathcal{H}|^2$ of this multi-antenna Rician channel is compactly given by:

$$F(\mathcal{Q}; P_{\text{dif}}, \mathcal{K}, M) = P_M\left(\mathcal{K}M, \frac{\mathcal{Q}}{P_{\text{dif}}}\right), \tag{8.4}$$

where $P_M(\cdot)$ is the complementary Marcum Q-function [14] with definition[1]:

$$P_\mu(x, y) = x^{\frac{1}{2}(1-\mu)} \int_0^y t^{\frac{1}{2}(\mu-1)} e^{-t-x}\, \mathrm{I}_{\mu-1}\left(2\sqrt{xt}\right) dt. \tag{8.5}$$

---

[1] Note that this definition is a different variant of the implementation found in major numeric computing environments, but the reference [14] provides a Fortran implementation together with the numerical algorithm description.

This power gain CDF is a generalised [78] or non-central gamma distribution [15] arising from a sum over squared per-antenna channel coefficients in Eqn. (8.3).

The distribution relates to a κ-μ envelope distribution [91], where the number of independent antenna elements corresponds to μ clusters and the $\mathcal{K}$-factor relates to the ratio κ between dominant and scattered channel components for a mean normalised to unity. The connection between a single antenna Rayleigh channel, the complementary Marcum Q-function and the effective gain CDF to arrive at a non-central gamma distribution is described in detail in the appendix 8.A and the connection to the κ-μ envelope distribution follows directly from comparison of the CDFs.

The mean effective power gain is:

$$\mathbb{E}\{\mathcal{Q}\} = M(\mathcal{K} + 1)P_{\text{dif}}, \tag{8.6}$$

which follows from adding M independent Rician channels with the same $\mathcal{K}$-factor and power in the diffuse component. Varying $\mathcal{K}$-factors for different antenna elements could be accounted for, by using the mean $\mathcal{K}$-factor in the above formulation. Both the $\mathcal{K}$-factor and the number of antenna elements M, have similar influence on the mean of the distribution.

Fig. 8.2a shows a selection of CDFs that describe the behaviour of a single antenna Rice channel. The channel gain is normalised with its mean to allow easier comparison of the small-scale fading aspects for different $\mathcal{K}$-factors. A stronger deterministic component leads to a dual slope behaviour with a steeper gradient closer to the median of the distribution. Nonetheless, the gradient converges to 10 dB per decade in the lower tail and is independent of the $\mathcal{K}$-factor. The very seldom cases occur only when the diffuse components can cancel the deterministic component almost perfectly. For a $\mathcal{K}$-factor of 10 dB, the gradient is steepest in the region between −15 dB and 0 dB with respect to the mean. This indicates that the lower tail approximation underestimates the channel behaviour for outage probabilities ranging from 10^{-4} to 0.5.

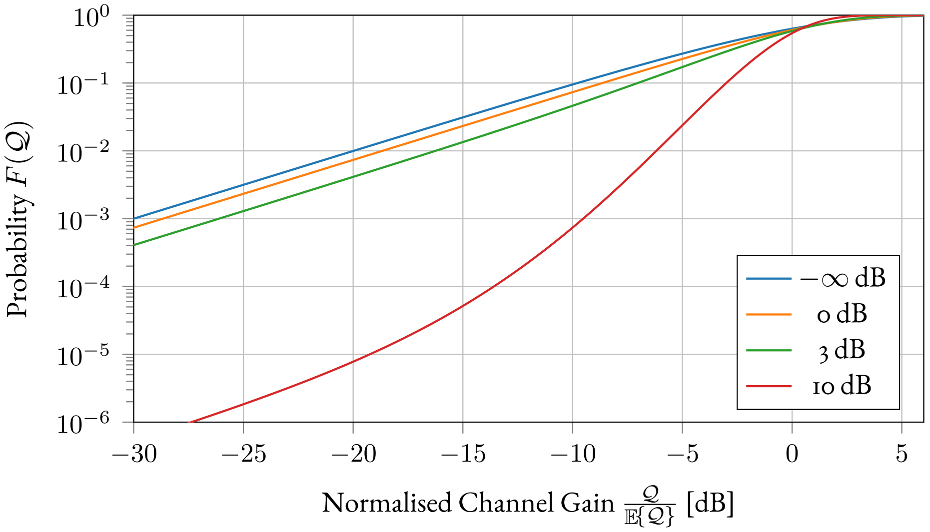

(a) CDFs

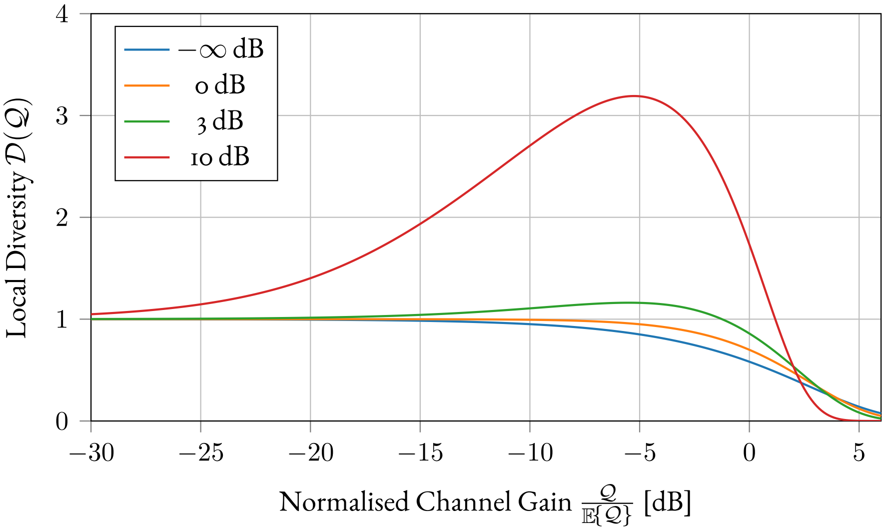

(b) local diversity

Figure 8.2: The normalised single antenna Rician channel is displayed for different $\mathcal{K}$-factors. The normalisation enforces unit mean. Larger $\mathcal{K}$-factors lead to a dual slope CDF. The steeper slope corresponds to the superelevation of the local diversity.

For sake of completeness is the corresponding PDF $f(\mathcal{Q})$ of the effective power gain given in the following equation.

$$f(\mathcal{Q}; P_{\text{dif}}, \mathcal{K}, M) \\ = \begin{cases} \frac{1}{P_{\text{dif}}} e^{-\frac{\mathcal{Q}}{P_{\text{dif}}} - \mathcal{K}} \mathrm{I}_0 \left(2\sqrt{\mathcal{K}\frac{\mathcal{Q}}{P_{\text{dif}}}} \right) & M = 1 \\ \frac{1}{P_{\text{dif}}} \left(P_{M-1}(\mathcal{K}M, \frac{\mathcal{Q}}{P_{\text{dif}}}) - P_M(\mathcal{K}M, \frac{\mathcal{Q}}{P_{\text{dif}}}) \right) & M > 1. \end{cases} \tag{8.7}$$

Here, $I_0(\cdot)$ is the zero-order modified Bessel function of the first kind. For the multi-antenna case, we can exploit the relation for derivatives of the complementary Marcum-Q function [14, Sec. 2.3].

8.4.1 Local Diversity

So far, the local diversity has only been introduced conceptually. Let us recall a common rule of thumb: the outage probability of a single antenna Rayleigh fading channel scales with 10 dB per decade in the lower tail. Furthermore, we have observed that a single antenna in narrowband Rician fading provides a diversity of one, too.

Therefore, a slope of 10 dB per decade outage probability is used as reference and we define the local diversity as derivative of the scaled logarithmic CDF of the channel power gain $\mathcal{Q}$ in dB:

$$\mathcal{D}(\mathcal{Q}) = \frac{\partial}{\partial 10^{\mathcal{Q}/10}} 10 \log_{10}\left(F(\mathcal{Q})\right) = \mathcal{Q}\frac{f(\mathcal{Q})}{F(\mathcal{Q})}. \tag{8.8}$$

This ensures a scaling of $10/D$ dB per decade outage probability locally at $\mathcal{Q}$. E.g. a local diversity of 10, 33 and 100 describes a slope of 1 dB, 0.3 dB and 0.1 dB per decade outage probability, respectively. The classic diversity is attained by evaluating the local diversity for $\mathcal{Q} \to -\infty$ dB.

Resolving the differentiation in Eqn. (8.8) reveals the quotient between PDF $f(\mathcal{Q})$ and CDF $F(\mathcal{Q})$, also known as inverse Mills' ratio, multiplied with $\mathcal{Q}$. To study how well a lower tail approximation represents the behaviour of the radio channel in the UR-relevant region for Rician channels, we use Eqns. (8.7)

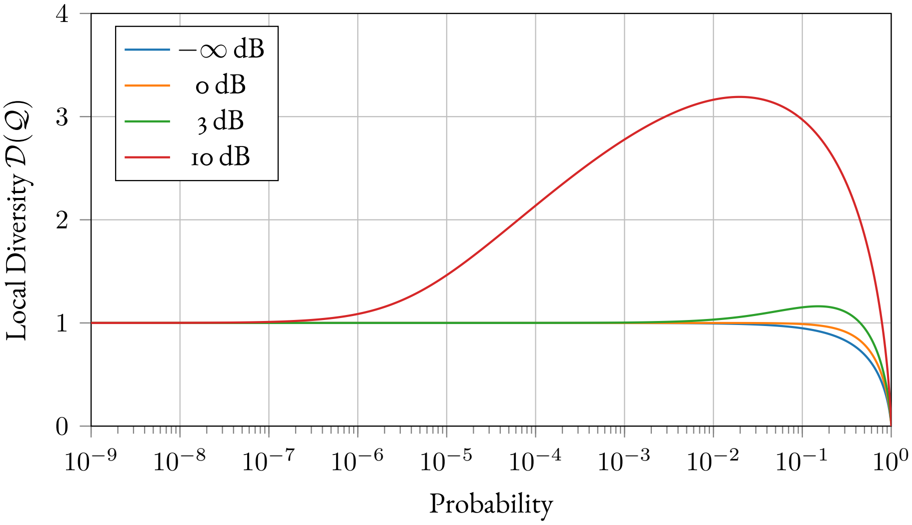

Figure 8.3: The local diversity with respect to the probability of a single antenna Rician channel for different $\mathcal{K}$-factors.

and (8.4) for the PDF and CDF of the effective power gain, respectively. The local diversity for antenna arrays can be expressed in terms of the complementary Marcum-Q function for $M > 2$:

$$\mathcal{D}(\mathcal{Q}; P_{\text{dif}}, \mathcal{K}, M) = \frac{\mathcal{Q}}{P_{\text{dif}}} \left(\frac{P_{M-1}(\mathcal{K}M, \frac{\mathcal{Q}}{P_{\text{dif}}})}{P_M(\mathcal{K}M, \frac{\mathcal{Q}}{P_{\text{dif}}})} - 1 \right). \tag{8.9}$$

Fig. 8.2b presents the local diversity for a single antenna Rician channel ($M = 1$). Larger $\mathcal{K}$-factors lead to a superelevated region before convergence to unity. The local diversity quantifies the increased steepness of the CDFs in Fig. 8.2a. Fig. 8.3 plots the local diversity with respect to probability to interpret its behaviour in the UR-relevant regime. The superelevation is pronounced in the region from 10^{-6} to 0.5 for a $\mathcal{K}$-factor of 10 dB. All other $\mathcal{K}$-factors have converged to a local diversity of unity for probabilities smaller than 10^{-3}.

This behaviour changes for larger arrays and is exemplified by the normalised local diversity in Figs. 8.4a and 8.4b for a Rayleigh and Rician channel with $\mathcal{K}$-factor

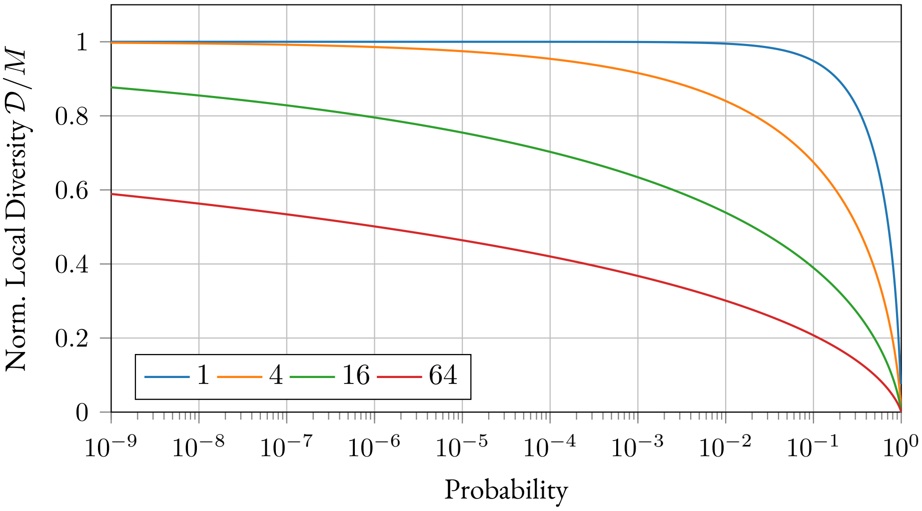

(a) Rayleigh Fading

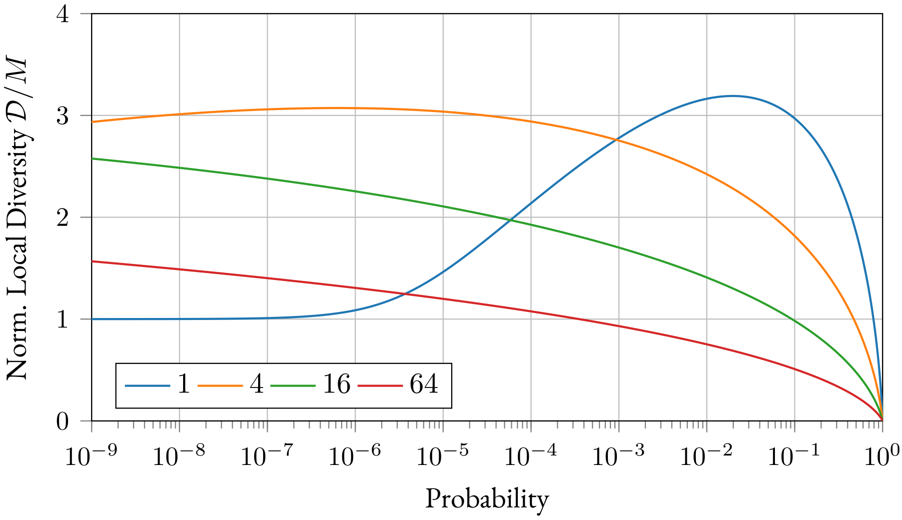

(b) Rician Fading ($\mathcal{K} =$ 10 dB)

Figure 8.4: Normalised local diversity for an M-antenna array with 1, 4, 16 or 64 elements. A tail approximation would underestimate the outage behaviour of the system for larger arrays in Rayleigh fading and overestimate it in Rician fading.

Table 8.1: Normalised local diversity $\mathcal{D}/M$ evaluated at 10^{-6} probability. The different coloured regions show where the asymptotic tail approximation holds (green), underestimates (red) or overestimates (blue) the slope in the UR-relevant regime.

$\mathcal{K}$	Number of Antennas (M)							
[dB]	1	2	4	8	16	32	64	128
$-\infty$	1.00	1.00	0.99	0.92	0.80	0.65	0.50	0.38
0.0	1.00	1.00	1.00	0.97	0.87	0.72	0.57	0.43
3.0	1.00	1.00	1.07	1.13	1.03	0.86	0.67	0.51
6.0	1.00	1.07	1.48	1.56	1.38	1.12	0.86	0.64
10.0	1.09	2.66	3.07	2.77	2.25	1.74	1.31	0.96
20.0	23.39	19.02	14.68	10.99	8.08	5.86	4.22	3.02

10 dB, respectively. Tab. 8.1 summarises the results for a probability of 10^{-6} over different $\mathcal{K}$-factors and number of antennas M. The normalisation is achieved by dividing the local diversity with the number of antennas. Hence, once the normalised local diversity attains unity, the classic diversity of M for large SNR is achieved. Therefore, the normalised local diversity can be interpreted as relative error between a lower tail approximation and the actual steepness of the effective gain CDF at the chosen probability.

8.5 Discussion

8.5.1 Validity of Lower Tail Approximations

The relative error of diversity is provided in Tab. 8.1, revealing three different connected regions. The first region (green) is covering small $\mathcal{K}$-factors for small systems, where the normalised local diversity is close to unity. A lower tail approximation will give reasonable results for UR-relevant statistics.

The second region (blue) belongs to Rayleigh fading and smaller $\mathcal{K}$-factors for an increasing number of antennas. In this case, the local diversity has not yet con-

Table 8.2: Analytic fading margins in dB at 10^{-6} probability.

$\mathcal{K}$ [dB]	1	2	4	8	16	32	64	128
$-\infty$	58.4	30.7	17.1	10.2	6.5	4.3	2.9	2.0
0.0	57.6	29.7	16.0	9.3	5.7	3.7	2.5	1.7
3.0	55.3	27.3	13.9	7.8	4.9	3.2	2.1	1.5
6.0	49.2	21.3	10.2	6.0	3.8	2.5	1.7	1.2
10.0	27.2	10.4	5.9	3.7	2.5	1.7	1.2	0.8
20.0	3.5	2.3	1.6	1.1	0.8	0.5	0.4	0.3

verged to unity and a lower tail approximation will overestimate the performance accordingly. E.g. a 64 antenna element array in Rayleigh fading at a probability of 10^{-6} will only provide the performance predicted by the asymptotic regime of a 32 antenna system. For large systems, only significant deterministic components will provide superelevation in the region of interest.

The last region (red) belongs to large $\mathcal{K}$-factors, where the local diversity is larger than the diversity, e.g. an environment with a $\mathcal{K}$-factor of 10 dB and 4 antennas presents a local diversity of $4 \cdot 3.07 \approx 12$ in the superelevated probability region. The superelevation moves towards smaller probabilities for an increasing number of antennas. Overall, the deterministic component of a Rician fading environment plays a role for every $\mathcal{K}$-factor for large antenna systems and a growing $\mathcal{K}$-factor increases the local diversity.

Tab. 8.1 demonstrates clearly that a low tail approximation is giving misleading results for the effective channel gain of massive MIMO systems in Rayleigh and Rician fading.

8.5.2 Array Deployment Strategies

In the following the impact of some array deployment strategies for URLLC applications is discussed. We relate the local diversity to the fading margin, another

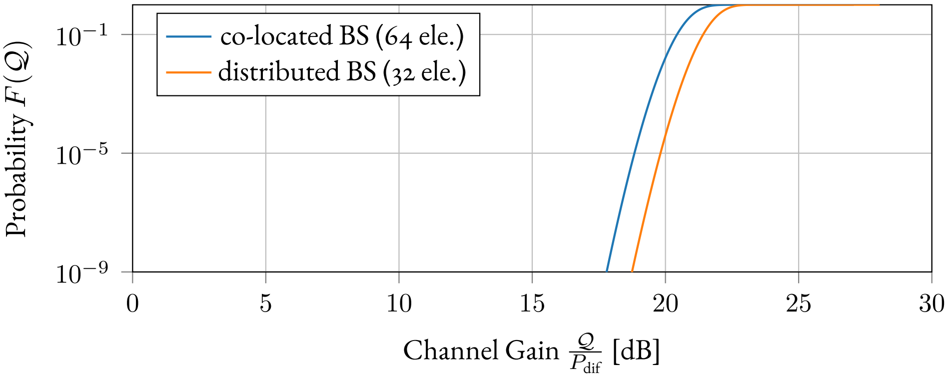

Figure 8.5: CDFs of a co-located 64 antenna base station with $\mathcal{K}$-factor 0 dB (blue) and the closest distributed 32 antenna base station (orange) with $\mathcal{K}$-factor 6 dB. The stronger deterministic component of the channel in the distributed base station case compensates for the reduced number of antennas, resulting in a similar local diversity at 10^{-6}, giving a slight advantage with respect to the mean of the channel gain.

tangible figure of merit. The fading margin is describing the gap between the median of the effective channel gain distribution and a target outage probability [C3]. It has been evaluated for the same parameters as the normalised local diversity and the result is presented in Tab. 8.2. This complementary perspective highlights the return on investment of extra power or antenna gain, to improve the reliability of a system.

Regarding each column in the table shows, that every increase of the deterministic component will reduce the margin, thereby improving the robustness of the system. Hence, it is worthwhile to compare a larger co-located system with a smaller $\mathcal{K}$-factor to smaller spatially distributed deployments.

It can be assumed that a distributed deployment will have at least one subarray closer to a user, giving a larger $\mathcal{K}$-factor. As an example: a co-located uncorrelated 64 antenna base station in a Rician fading environment with $\mathcal{K} = 0\,\text{dB} = 1$ would require a fading margin of 2.5 dB at an outage probability for 10^{-6}. The mean of the effective channel gain is $64 * (1+1) P_{\text{dif}} = 128 P_{\text{dif}}$. Instead, placing two non-cooperating uncorrelated 32 antenna BSs into that environment, which reduces the length of the deterministic path to a half for a user, could increase the $\mathcal{K}$-factor by 6 dB. The closer base stations would then require a fading margin of 2.5 dB at an outage probability for 10^{-6}. For this setting the mean gain would be $32 * (4+1)P_{\text{dif}} = 160P_{\text{dif}}$.

The CDFs of both deployments are shown in Fig. 8.5, where both slopes of have not yet converged to the asymptotic behaviour of the lower tail in the UR-relevant regime. In this toy example, distributed base stations requiring the same amount of hardware would give equal fading margins and increase the mean effective gain compared to the co-located case. Hence, not only capacity improvements can be achieved by densification of base stations, but UR-relevant statistics can improve too without increasing the amount of deployed hardware.

In a more general situation, for fading environments with deterministic propagation components, the number of antenna elements per base station influences where the normalised local diversity shows superelevation. We notice further, in a pure Rayleigh fading environment, increasing the number of base station antennas gives diminishing returns (see Fig. 8.4a).

8.5.3 Inferring UR-relevant Statistics?

So, how can we infer the system behaviour of events that barely ever happen? Given a limited number of measurable samples from each antenna element, how could the UR-relevant statistics be analysed in real world systems?

There are two basic approaches for UR antenna arrays:

Element Statistics

The first is based on collection of antenna element observations, estimation of each distribution and careful modeling of correlation properties. Antenna elements that belong to the same local area could be lumped into a single distribution to make more samples available. Post-processing of the resulting distributions with combination strategies like selection combining (SC) or MRC result in a CDF to be evaluated in the UR-relevant regime. In case of SC, it is not necessary to have a reliable estimate of the antenna element CDFs in that regime, but rather in the regime resulting from the M-th root of the target outage probability. This follows from the maximum order statistic [54] for the strongest constituent, being the M-th power of the element CDF. Since MRC will give a better combined gain than SC, using a SC result allows to bound the system behaviour in the UR-relevant regime based on reliable estimates of the element CDFs.

Combined Statistics

The second approach implements a specific combination strategy, evaluating the UR-relevant statistics directly. This includes intrinsically antenna correlation, avoiding the necessity of explicit characterisation. Unfortunately, this strategy requires prohibitively many observations. Even for the first approach a lot of samples are necessary, but the antenna element observations do not need to be observed in the UR-relevant regime directly, since this regime only matters for the effective channel gain! Furthermore, the correlation is expected to depend to a lesser extent on the combined channel stationarity, allowing them to be studied in more detail with help of all antenna element observations.

8.5.4 Correlated Channels

Even though this manuscript demonstrated a local diversity based analysis for uncorrelated systems, the same ideas can be transferred to correlated antenna arrays. Analytic results can be derived from the effective channel gain PDF and CDF of the correlated system, to avoid Monte Carlo simulations that depend on a large amount of observations to provide reasonable insight.

8.6 Conclusion

Acquisition of UR-relevant channel statistics is difficult to achieve in practical situations, because the number of required observations is tremendous. Ultimately, the spatial, spectral and temporal stationarity of the radio channel restricts the collection of a sufficient number of observations. The approach of using the asymptotic lower tail behaviour, to avoid determination of a specific fading distribution, can be used for small arrays up to four antennas in low $\mathcal{K}$-factor Rician fading. Systems that provide large diversity, require consideration of the local diversity in the UR-relevant regime. There, the asymptotic behaviour applies to probabilities beyond the UR-relevant regime only. Normalisation of the local diversity with the number of antenna elements in an array gives a relative deviation from the classic diversity. Furthermore, the local diversity opens up for performance evaluation, where measurements of correlated antenna systems can be compared to an uncorrelated optimum.

For fast and numerically stable calculations, the distribution functions and local diversity of the effective gain of an uncorrelated antenna array in Rician fading can be formulated on the basis of the complementary Marcum-Q function. Evaluation of the fading margin and distribution mean reinforces that a dense deployment of smaller base stations with the potential for increased deterministic radio channels is preferable over very large co-located systems, not only improving system capacity but also robustness.

8.A CDF of the Effective Power Gain

The *non-central gamma distribution* has PDF $w_\rho(x;\alpha,\mu)$ for index ρ, scale α, and non-centrality μ [15, (1.47')] for $x \geq 0$:

$$w_\rho(x;\alpha,\mu) = \frac{1}{\alpha} e^{-\frac{x}{\alpha}-\mu} \left(\frac{x}{\alpha\mu}\right)^{\frac{1}{2}(\rho-1)} I_{\rho-1}\left(2\sqrt{\frac{\mu x}{\alpha}}\right). \tag{8.10}$$

The corresponding CDF $W_\rho(x;\alpha,\mu)$ can be directly related to the definition of the complementary Marcum Q-function in Eqn. (8.5) by substitution of $t = \frac{x'}{\alpha}$ in the integral relation between CDF and PDF:

$$W_\rho(x;\alpha,\mu) = \int_0^x w_\rho(x';\alpha,\mu)dx' = P_\rho(\mu, \frac{x}{\alpha}). \tag{8.11}$$

The gain PDF $f(\mathcal{Q}; P_{\text{dif}}, \mathcal{K}, M = 1)$ of a single antenna Rician channel is readily available by using the Rician envelope PDF from [13, (5.3.7)] applying the transformation to the power PDF [13, (5.2.1)] and replacing the power term of the deterministic component [13, (5.3.8)], resulting in:

$$\begin{aligned} f(\mathcal{Q};& P_{\text{dif}}, \mathcal{K}, M = 1) \\ &= \frac{1}{P_{\text{dif}}} \exp\left(-\frac{\mathcal{Q}}{P_{\text{dif}}} - \mathcal{K}\right) I_0\left(2\sqrt{\mathcal{K}\frac{\mathcal{Q}}{P_{\text{dif}}}}\right) \\ &= w_1(\mathcal{Q}; P_{\text{dif}}, \mathcal{K}). \end{aligned} \tag{8.12}$$

This PDF is a special case of the non-central gamma distribution PDF in Eqn. (8.10) for index one, scale P_{dif} with non-centrality $\mathcal{K}$.

For M independent single antenna Rician channels with potentially differing $\mathcal{K}$-factors $\mathcal{K}_m \forall m \in [1, \cdots, M]$ the additive property of non-central gamma distributions can be used to get the PDF of the effective channel gain. The addition property allows to represent the sum of independent random variables with the same scale, potentially varying index and non-centrality as non-central gamma distribution [15, (1.51)]. The generalisation of Eqn. (8.12) for an M antenna array follows a non-central gamma distribution of index M and non-centrality $\sum_{m=1}^{M} \mathcal{K}_m$:

$$f(\mathcal{Q}; P_{\text{dif}}, \mathcal{K}, M) = w_M\left(\mathcal{Q}; P_{\text{dif}}, \sum_{m=1}^{M} \mathcal{K}_m\right). \tag{8.13}$$

Using Eqn. (8.11) gives the CDF of the effective channel gain based on the inverse Marcum Q-function:

$$F(\mathcal{Q}; P_{\text{dif}}, \mathcal{K}, M) = P_M\left(\sum_{m=1}^{M} \mathcal{K}_m, \frac{\mathcal{Q}}{P_{\text{dif}}}\right). \tag{8.14}$$

9 Paper J2: Statistics of Correlated Rician Massive MIMO Channels

Authors	J. Abraham, P. Ramírez-Espinosa and T. Ekman
Journal	IEEE Open Journal of Antennas and Propagation
Date	January, 2022
Original-URL	`https://ieeexplore.ieee.org/document/9695960`
DOI	10.1109/OJAP.2022.3147015
arXiv	2112.06692

9.1 Abstract

Massive multiple-input multiple-output base stations use multiple spatial diversity branches, which are often assumed to be uncorrelated in theoretical work. Correlated branches are seldom considered since they are mathematically less tractable. For correlated Rician fading, only the first- and second-order moments have been explored. To describe propagation environments more accurately, full distribution functions are needed.

This manuscript provides distribution functions for the maximum ratio combining effective channel, a quadratic form of a random complex normal channel vector. Its mean vector and covariance matrix are based on a plane wave model incorporating array geometry, antenna element pattern, power angular spectra and power delay profiles. Closed-form approximations of the distribution functions are presented, to allow the fast evaluation of many real-world scenarios.

The statistical framework is used to show that low-directivity antenna elements provide better performance in angular constricted Rician fading with off-axis incidence than high-directivity elements. Moreover, two base station array layouts are compared, showing that a half-circle array illuminates a cell more evenly than a

uniform linear array. With the full distribution functions available, performance can be compared over the full range of received powers and not only based on the average signal-to-noise ratio.

9.2 Introduction

In many massive MIMO systems, users are communicating over multiple subcarriers with a BS equipped with a LSAS. These systems provide not only better performance for conventional cellular networks [18], but have benefits in internet of things applications too [6], [92]. Time division duplex transmission is necessary, if channel reciprocity should allow for simplified channel state information acquisition. On one hand, the radio channel is often modeled with uncorrelated antennas subject to narrow-band Rayleigh or Rician fading. On the other hand, measurement campaigns provide evidence that the radio channel is correlated in space, time and frequency. For massive MIMO systems, correlated Rician fading has been considered in context of the spectral efficiency [93] and cell-free systems [94], [95]. Those contexts only evaluate the first- and/or second-order behaviour of correlated narrow-band Rician fading channels.

To fully cover wide-band correlated Rician fading in LSAS, this work describes a $\mathcal{CN}$-RV model with a non-trivial covariance matrix. The vector elements are representing channel coefficients for antennas and delay taps, to allow the joint consideration of the spatial and the delay domain. The covariance matrix allows to model correlation between antenna elements for the same delay tap, different delay taps of the same antenna element and mixtures where necessary. The spatial domain is parameterised by antenna element positions and corresponding PASs, whilst the delay domain is covered by PDPs. The model allows to consider correlation between antennas as well as delay taps. Hence it incorporates aspects needed to derive a physically motivated distribution for the effective channel power gain arising from MRC. To that extent, the influence of incidence of a deterministic channel component[1], its magnitude and correlation of the diffuse channel on

---

[1] The deterministic channel component can originate from a line of sight component or a specular component.

single user performance is presented. We provide (accurate approximate) PDFs and CDFs for the effective channel gain. Moreover, the steepness of the effective channel CDF is evaluated to investigate the local diversity [C4] in closed-form for different outage probabilities.

Related to this work is the effective channel with selection combining for several equally correlated fading distributions given in [96]. The capacity for correlated Rayleigh MIMO channels has been derived by characterising distributions of eigenvalues of the propagation environment [97]. For correlated Rician channels, the eigenvalue spread of the covariance matrix and the angle of the deterministic component vector with respect to the range space of the covariance matrix are key quantities of performance metrics in [98]. Furthermore, they provide a power and a Laguerre series expansion of the effective channel. Another power series approximation of the narrow-band MRC effective channel signal-to-noise ratio for antennas in a linear array is given in [88]. The ergodic capacity of MRC for correlated Rician channels has been evaluated in [99], showing that a correlated Rician fading channel can improve over an uncorrelated channel under very specific circumstances. For uncorrelated Rician fading, massive MIMO systems have been analysed based on asymptotic expressions for the signal-to-interference-plus-noise ratio in a multi-cell system [100]. For correlated Rician fading of a multi-cell massive MIMO scenario, different channel estimators and their resulting $\mathcal{CN}$-RV parameters have been derived in [93]. Channel hardening and spectral efficiency in correlated Rician fading for cell-free massive MIMO has been discussed in [94], [95]. A more generalised complex normal channel has been considering a Weichselberger correlation model and was analysed with focus on channel hardening and favourable propagation [101]. We observe, that the full statistics of correlated Rician fading channels for LSAS have not been presented so far, since they go beyond the first- and second-order statistic of the effective channel gain.

Other correlation matrix models than the Weichselberger model have been proposed in the literature. A *constant correlation matrix*, where each pair of antennas is equally correlated [102], provides a simplistic approximation. An *exponential correlation matrix*, where the difference of antenna indices determines the correlation coefficient [103], is a more realistic approximation for ULAs. A *generalised* *correlation matrix* model, where the correlation coefficient is a function of the euclidean distance between antenna elements, has been recently discussed in [104] and can provide approximations for more general array configurations like an uniform rectangular array. A more propagation motivated *3D local scattering model* with arbitrary geometry, considering the position of array elements and the angle of arrival distribution of the diffuse radio channel, has been presented [19, sec. 7.3.2].

In this work, we add antenna element pattern explicitly to the 3D local scattering model, to analyse the effect of low or high directivity elements, that not necessarily point into the same direction. The result is a physically meaningful parametrisation of the correlation matrix elements, whereas the aforementioned general Weichselberger model has a higher abstraction level based on eigenvalues and eigenbases. Moreover, this manuscript extends our work on the effective channel in uncorrelated Rayleigh fading [J1]. *Our main contribution is a method to obtain the statistics of the effective massive MIMO channel in correlated Rician fading.* This is achieved by describing a wide-band massive MIMO system as a non-central $\mathcal{CN}$-RV (sec. 9.3). The effective channel gain is a CGQF for which an improved accurate approximation of the PDF and CDF is provided via a confluent CGQF (sec. 9.4). To utilise the $\mathcal{CN}$-RV model, mean and covariance are characterised considering physical properties of the propagation environment (sec. 9.5):

- a 3D local scattering model under consideration of PASs,
- antenna pattern of arbitrarily positioned and oriented BS array elements and
- PDPs with Rician fading taps.

The findings are used to compare BSs with a ULA or a half circle array for antenna elements with varying directivity after verification of the CGQF method with simulations (sec. 9.6).

The manuscript is structured as follows: it introduces the correlated complex normal channel in sec. 9.3; provides the distribution functions of the effective channel gain in sec. 9.4; shows some examples for the spatial correlation in sec. 9.5;

continues with simulations for different scenarios in sec. 9.6 and closes with discussion and conclusion in sec. 9.7 and sec. 9.8, respectively.

9.2.1 Notation

A variable is represented as a scalar a, a vector $\boldsymbol{a}$ or a matrix $\mathbf{A}$. Square brackets are picking an element from a structure according to the subscript, e.g. $[\boldsymbol{a}]_i$ is the i-th element of vector $\boldsymbol{a}$. The transpose and hermitian operator are $(\cdot)^{\mathrm{T}}$ and $(\cdot)^{\mathrm{H}}$. The expectation and variance of random variables are denoted with $\mathbb{E}\{\cdot\}$ and $\mathbb{V}\{\cdot\}$, respectively. The symbols $\mathcal{CN}$, χ^2 and χ'^2 designate the complex normal, central χ-squared and non-central χ-squared distribution, where e.g. $a \sim \mathcal{CN}(0,1)$ means that a is distributed according to a central standard complex normal distribution. The angles of the spherical coordinate system are θ for the azimuth ($\theta \in [0, 2\pi]$) and ϕ the polar angle ($\phi \in [0, \pi]$).

9.3 Correlated Complex Normal Channel

In this section, a correlated $\mathcal{CN}$-RV $\boldsymbol{h} \in \mathbb{C}^{MN} \sim \mathcal{CN}(\boldsymbol{\mu}, \boldsymbol{\Sigma})$ is introduced to model the end-to-end propagation between a user terminal and a BS with M antenna elements observing a N-tap channel. We are going to describe the mean vector $\boldsymbol{\mu} \in \mathbb{C}^{MN}$ and covariance matrix $\boldsymbol{\Sigma} \in \mathbb{C}^{MN \times MN}$ based on antenna element locations $\boldsymbol{r}_m$ and pattern $G_m(\theta, \phi)$ for antenna element m in conjunction with the PASs $p_{l,n}(\theta, \phi)$[2], PDPs $S_{l,n}$ and Rician $\mathcal{K}$-factors $\mathcal{K}_{l,n}$ of the propagation environment. The index l describes a subarray which belongs to a local area where the statistics are stationary during tap n and the propagation environment is illuminated by a terminal with power P. An overview of all constituents of the model is given in Fig. 9.1. This model describes directly the observable channel coefficients and received powers at the BS elements and highlights the impact of BS array design on the effective channel gain.

---

[2] The term PAS is used here for both the PAS and the PDF of the PAS, because the PDP absorbs the power scaling.

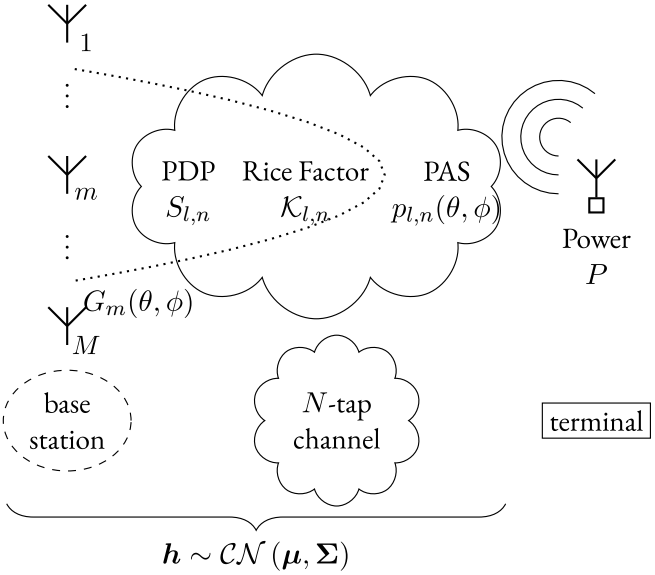

Figure 9.1: The complex normal random vector channel parameters $\boldsymbol{\mu} \in \mathbb{C}^{MN}$ and $\boldsymbol{\Sigma} \in \mathbb{C}^{MN \times MN}$ are determined by the M antenna elements (with individual antenna element pattern $G_m(\theta, \phi)$) and physical properties of delay taps n (power delay profile (PDP) $S_{l,n}$, Rice Factor $\mathcal{K}_{l,n}$ and power angular spectrum (PAS) $p_{l,n}(\theta, \phi)$) of the propagation environment for antennas in potentially different local areas l.

9.3.1 Propagation Environment

The antenna element m, local area l and delay tap n will be omitted for ease of notation in the following subsections unless they are necessary to distinguish between quantities.

The PDP coefficient S describes the user transmit power that is spread into a delay tap. The corresponding Rician factor $\mathcal{K}$ further defines the quotient between the deterministic component $\bar{h}$ and the diffuse component $\tilde{h}$ of that delay tap.

The PAS $p(\theta, \phi)$ is split into parts too, to represent the deterministic component with the incidence angles $\bar{\theta}$ and $\bar{\phi}$ as

$$\bar{p}(\theta, \phi) = \delta\left(\theta - \bar{\theta}\right) \delta\left(\phi - \bar{\phi}\right) \tag{9.1}$$

and $\tilde{p}(\theta, \phi)$ absorbing the diffuse component. Both, $\bar{p}(\theta, \phi)$ and $\tilde{p}(\theta, \phi)$ are a PDF. The PAS under consideration of the $\mathcal{K}$-factor can now be described by

$$p(\theta, \phi) = \frac{\mathcal{K}\bar{p}(\theta, \phi) + \tilde{p}(\theta, \phi)}{\mathcal{K} + 1}. \tag{9.2}$$

9.3.2 Channel Realisations

A Rician channel coefficent h can be composed by superposition of a plane wave for the deterministic component $\bar{h}$ and a large number of Z plane waves distributed according to the PAS to represent the diffuse component $\tilde{h}$:

$$h = \bar{h} + \tilde{h}. \tag{9.3}$$

The wavevector $\boldsymbol{k}$ of a wave with incidence angles θ and ϕ at wavelength λ is given by

$$\boldsymbol{k}(\theta, \phi) = \frac{2\pi}{\lambda} \begin{bmatrix} \cos\theta \sin\phi \\ \sin\theta \sin\phi \\ \cos\phi \end{bmatrix}. \tag{9.4}$$

This wave has phase φ at position $\boldsymbol{r}$:

$$\varphi(\theta,\phi) = \boldsymbol{k}(\theta,\phi)\cdot\boldsymbol{r}. \tag{9.5}$$

The deterministic component $\bar{h}$ is given by the PDP coefficient S, the Rician $\mathcal{K}$-factor $\mathcal{K}$, the antenna element pattern $G(\theta,\phi)$ and the phase term:

$$\bar{h} = \sqrt{S\frac{\mathcal{K}}{\mathcal{K}+1}G(\bar{\theta},\bar{\phi})}\exp\left(\mathrm{j}\bar{\varphi}(\bar{\theta},\bar{\phi})\right). \tag{9.6}$$

The diffuse component $\tilde{h}$ is composed with a sum over N plane waves:

$$\tilde{h} = \sqrt{\frac{S}{\mathcal{K}+1}}\sqrt{\frac{1}{N}}\sum_{z=1}^{Z}\sqrt{G(\tilde{\theta}_n,\tilde{\phi}_n)}a_z\exp\left(\mathrm{j}\tilde{\varphi}_z(\tilde{\theta}_n,\tilde{\phi}_n)\right) \tag{9.7}$$

with a_z being iid random magnitudes, drawn from a central standard complex normal distribution. The exponential term describes the additional phase of the incoming plane wave n due to antenna element position $\boldsymbol{r}$ for an incidence wave vector $\boldsymbol{k}_z$.

9.3.3 Mean and Auto-Covariance

The channel realisations for all M antennas and all N taps are conditioned on the propagation environment and antenna array properties as described for the individual coefficient in (9.6) and (9.7). To capture the mean and covariance of the correlated random vector, explicit mappings of indices i and j to antenna elements m_i, m_j and delay taps n_i and n_j are necessary. The mapping follows

$$i = m_i + (n_i - 1)M \tag{9.8}$$
$$j = m_j + (n_j - 1)M \tag{9.9}$$

to consecutively identify each antenna-tap pair uniquely. Antenna elements m_i and m_j belong to the local areas l_i and l_j, respectively.

The mean vector element $[\boldsymbol{\mu}]_i$ is simply the realisation in (9.6) because all variables are deterministic:

$$[\boldsymbol{\mu}]_i = \mathbb{E}\{h_{m_i,n_i}\} = \bar{h}_{m_i,n_i}. \tag{9.10}$$

The main diagonal of the covariance matrix $\boldsymbol{\Sigma}$ consists of auto-covariances of the realisations of the diffuse component in (9.7):

$$\begin{aligned}[\boldsymbol{\Sigma}]_{i,i} &= \mathbb{V}\{h_{m_i,n_i}\} = \mathbb{E}\left\{\tilde{h}_{m_i,n_i}\tilde{h}^*_{m_i,n_i}\right\} \\ &= \frac{S}{\mathcal{K}+1}\iint_{\Omega} |G(\theta,\phi)|\,\tilde{p}(\theta,\phi)d\Omega.\end{aligned} \tag{9.11}$$

The second line of the last equation is a consequence for $Z \rightarrow \infty$ and replacement of the sum by integration over the full sphere surface Ω to account for all directions of incident waves. Here, the pattern of antenna element m_i is weighting the PAS.

9.3.4 Cross-Covariances and Correlations

The remaining entries of the covariance matrix depend on the correlation coefficient $\rho_{i,j}$ between pairs of antennas and taps:

$$[\boldsymbol{\Sigma}]_{i,j} = \rho_{i,j}\sqrt{[\boldsymbol{\Sigma}]_{i,i}\,[\boldsymbol{\Sigma}]_{j,j}}. \tag{9.12}$$

The correlation coefficient $\rho_{i,j}$ is by definition:

$$\rho_{i,j} = \frac{\mathbb{E}\left\{\tilde{h}_{m_i,n_i}\tilde{h}^*_{m_j,n_j}\right\}}{\sqrt{\mathbb{E}\left\{\tilde{h}_{m_i,n_i}\tilde{h}^*_{m_i,n_i}\right\}\mathbb{E}\left\{\tilde{h}_{m_j,n_j}\tilde{h}^*_{m_j,n_j}\right\}}}, \tag{9.13}$$

where only diffuse components have an influence on the covariance matrix $\boldsymbol{\Sigma}$. In the following, we will restrict our focus to radio channels exhibiting *uncorrelated scattering* in the same local area ($l_i = l_j = l$)

$$\rho_{i,j} = \rho^t_{m_i,m_j}\delta(l_i - l_j)\delta(n_i - n_j), \tag{9.14}$$

because our interest is focused on the influence of antenna element correlations. The correlated scattering case is left for future investigation. It might arise from antenna elements being spaced so far from each other, that the same scatterer influeces different delay taps of those elements. The restriction here imposes a diagonal block structure on the covariance matrix $\mathbf{\Sigma}$, where each block $\mathbf{\Sigma}^t$ describes the correlation between antenna elements for tap t.

The antenna correlation coefficient $\rho^t_{m_i,m_j}$ is shown in (9.16) and is an extension of the 3D local scattering model [19, sec. 7.3.2] due to the consideration of antenna element pattern. The local scattering model has an impact on the handling of correlation between antennas in different local areas. We are assuming that the local areas are distant enough, such that the incoming plane waves are decorrelated. Each incident plane wave in local area l produces a direction dependent phase shift $\Delta\varphi_{m_i,m_j}$ between antenna elements at positions $\boldsymbol{r}_{m_i}$ and $\boldsymbol{r}_{m_j}$:

$$\Delta\varphi_{m_i,m_j}(\theta,\phi) = \boldsymbol{k}(\theta,\phi)\cdot\left(\boldsymbol{r}_{m_i} - \boldsymbol{r}_{m_j}\right). \tag{9.15}$$

The expectation over the sum of plane waves in (9.16) is replaced for $Z \to \infty$ by an integration over the full sphere Ω in (9.17). The diffuse PASs $\tilde{p}_{l,t}(\theta,\phi)$ conditions the incident plane waves and the integral incorporates antenna positions as well as antenna element pattern. This allows to determine the missing elements of the correlation matrix Σ required for a full characterisation of the $\mathcal{CN}$-RV $\boldsymbol{h}$.

9.3.5 Summary

The $\mathcal{CN}$-RV $\boldsymbol{h} \sim \mathcal{CN}(\boldsymbol{\mu},\mathbf{\Sigma})$ is fully characterised based on antenna positions, antenna pattern, PDPs, Rician $\mathcal{K}$-factors, PASs. The dependencies of elements of the mean vector and the covariance matrix are summarised in the following lines, where antenna elements, delay taps and local areas are explicitly designated in the

$$\rho^n_{m_i,m_j} = \frac{\mathbb{E}_{\tilde{\theta}_z,\tilde{\phi}_z}\left\{\sum_{z=1}^{Z} \sqrt{G_{m_i}(\tilde{\theta}_z,\tilde{\phi}_z)}\sqrt{G_{m_j}(\tilde{\theta}_z,\tilde{\phi}_z)}^{*} \exp\left(\mathrm{j}\left(\tilde{\varphi}_{z,m_i}(\tilde{\theta}_z,\tilde{\phi}_z) - \tilde{\varphi}_{z,m_j}(\tilde{\theta}_z,\tilde{\phi}_z)\right)\right)\right\}}{\sqrt{\mathbb{E}_{\tilde{\theta}_z,\tilde{\phi}_z}\left\{\sum_{z=1}^{Z} \left|G_{m_i}(\tilde{\theta}_z,\tilde{\phi}_z)\right|\right\} \mathbb{E}_{\tilde{\theta}_z,\tilde{\phi}_z}\left\{\sum_{z=1}^{Z} \left|G_{m_j}(\tilde{\theta}_z,\tilde{\phi}_z)\right|\right\}}} \tag{9.16}$$

$$\rho^n_{m_i,m_j} = \frac{\iint_{\Omega} \tilde{p}_{l,n}(\theta,\phi)\sqrt{G_{m_i}(\theta,\phi)}\sqrt{G_{m_j}(\theta,\phi)}^{*} \exp\left(\mathrm{j}\Delta\varphi_{m_i,m_j}(\theta,\phi)\right) d\Omega}{\sqrt{\iint_{\Omega} \tilde{p}_{l,n}(\theta,\phi)\left|G_{m_i}(\theta,\phi)\right| d\Omega \iint_{\Omega} \tilde{p}_{l,n}(\theta,\phi)\left|G_{m_j}(\theta,\phi)\right| d\Omega}} \tag{9.17}$$

subscripts of the variables:

$$[\boldsymbol{\mu}]_i \leftarrow S_{m_i,n_i}, \mathcal{K}_{m_i,n_i}, G_{m_i}(\theta,\phi), \bar{p}_{l_i,n_i}(\theta,\phi), \boldsymbol{r}_{m_i}, \lambda \tag{9.18}$$

$$[\boldsymbol{\Sigma}]_{i,i} \leftarrow S_{m_i,n_i}, \mathcal{K}_{m_i,n_i}, G_{m_i}(\theta,\phi), \tilde{p}_{l_i,n_i}(\theta,\phi) \tag{9.19}$$

$$\begin{aligned}\rho_{i,j} \leftarrow\ & G_{m_i}(\theta,\phi), G_{m_j}(\theta,\phi), \tilde{p}_{l_i,n_i}(\theta,\phi), \tilde{p}_{l_j,n_j}(\theta,\phi),\\ & \left(\boldsymbol{r}_{m_i} - \boldsymbol{r}_{m_j}\right), \lambda\end{aligned} \tag{9.20}$$

$$\begin{aligned}[\boldsymbol{\Sigma}]_{i,j} \leftarrow\ & S_{m_i,n_i}, S_{m_j,n_j}, \mathcal{K}_{m_i,n_i}, \mathcal{K}_{m_j,n_j}, G_{m_i}(\theta,\phi),\\ & G_{m_j}(\theta,\phi), \tilde{p}_{l_i,n_i}(\theta,\phi), \tilde{p}_{l_j,n_j}(\theta,\phi), \left(\boldsymbol{r}_{m_i} - \boldsymbol{r}_{m_j}\right),\\ & \lambda\end{aligned} \tag{9.21}$$

The channel vector can be reshaped into a $M \times N$ matrix and multiplication of a discrete Fourier transform matrix from the right allows a transformation into the frequency domain if needed. That common matrix form of the channel in both delay and frequency domain does not allow to keep the individual correlations between pairs of antennas and taps separate. The covariance matrix $\boldsymbol{\Sigma}$ of the $\mathcal{CN}$-RV has size $MN \times MN$ and the covariance matrix of the matrix channel of size $M \times M$ is combining the individual tap correlations describing the covariance between antennas over all taps.

9.4 Effective Channel Gain

This section will provide the PDF and CDF of the effective channel gain. This is the channel gain after combining all branches (antenna elements and taps) at the BS. We focus on the matched filter for the single user case, since it is the optimal result for that specific user. Any other combination scheme under consideration of multiple users will provide poorer performance to the intended user. To leave no user in a multi-user setting behind, interference should be suppressed by other means than interference suppressing combining. The effective channel $\mathcal{H}$ for MRC is:

$$\mathcal{H} = \boldsymbol{w}^{\mathrm{T}}\boldsymbol{h} = \frac{\boldsymbol{h}^{\mathrm{H}}\boldsymbol{h}}{\sqrt{\|\boldsymbol{h}\|_2^2}} = \sqrt{\boldsymbol{h}^{\mathrm{H}}\boldsymbol{h}}, \tag{9.22}$$

and the corresponding effective channel power gain $\mathcal{Q}$:

$$\mathcal{Q} = |\mathcal{H}|^2 = \boldsymbol{h}^{\mathrm{H}}\boldsymbol{h} \tag{9.23}$$

is a CGQF of the channel vector and a coherent summation of all vector channel elements.

Closed-form approximations of the PDF and CDF of CGQFs are derived in the following. The general idea is based on the principles of the approximation of real Gaussian quadratic forms [105], but using the moment-generating function of the confluent non-central CGQF [106]. We have reformulated the recursion in the approximation to reduce the growth rate of some auxiliary variables. This allows to increase the approximation order, improving the accuracy of the method, enabling the analysis of LSAS. Furthermore, the local diversity [C4] is approximated based on the PDF and CDF of the confluent CGQFs.

9.4.1 Approximations of Statistics of Gaussian Quadratic Forms

The vector $\boldsymbol{v} \sim \mathcal{CN}(\boldsymbol{\mu}, \boldsymbol{\Sigma})$ is an N-element random vector, with $\boldsymbol{\mu}$ and $\boldsymbol{\Sigma}$ characterising the mean vector and positive definite covariance matrix of a multivariate complex normal distribution, respectively. The vector has a quadratic form $\mathcal{Q}$ with positive semidefinite operator matrix $\mathbf{A}$ being:

$$\mathcal{Q} = \boldsymbol{v}^{\mathrm{H}}\mathbf{A}\boldsymbol{v}. \tag{9.24}$$

This quadratic form has the same structure as the effective channel in (9.22), where $\boldsymbol{v} = \boldsymbol{h}$ and $\mathbf{A} = \mathbf{I}$.

The vector $\boldsymbol{v}$ can be decomposed:

$$\boldsymbol{v} = \mathbf{L}\boldsymbol{x} + \boldsymbol{\mu} = \mathbf{L}\left(\boldsymbol{x} + \tilde{\boldsymbol{\mu}}\right). \tag{9.25}$$

such that $\boldsymbol{x} \sim \mathcal{CN}_N(0, \mathbf{I})$ is an iid standard $\mathcal{CN}$-RV. The matrix $\mathbf{L}$ provides a mixing of the iid variables to introduce the correlation given by $\boldsymbol{\Sigma}$ (e.g. by Cholesky decomposition $\boldsymbol{\Sigma} = \mathbf{L}\mathbf{L}^{\mathrm{H}}$) and a transformation of the mean vector $\tilde{\boldsymbol{\mu}} = \mathbf{L}^{-1}\boldsymbol{\mu}$.

Rewriting the quadratic form with the decomposed vector $\boldsymbol{v}$ results in:

$$\mathcal{Q} = (\boldsymbol{x} + \tilde{\boldsymbol{\mu}})^{\mathrm{H}} \mathbf{L}^{\mathrm{H}} \mathbf{A} \mathbf{L} (\boldsymbol{x} + \tilde{\boldsymbol{\mu}}) \tag{9.26}$$

which can be expressed in terms of eigenvalues λ_i of $\mathbf{L}^{\mathrm{H}}\mathbf{AL}$:

$$\mathcal{Q} = \sum_{i}^{N} \lambda_i (x_i + \tilde{\mu}_i)^* (x_i + \tilde{\mu}_i) = \sum_{i}^{N} \lambda_i \left| x_i + \tilde{\mu}_i \right|^2 . \tag{9.27}$$

This reveals the structure of a sum of λ_i weighted non-central χ^2 variables $(\left|x_i + \tilde{\mu}_i\right|^2 \sim \chi_2'^2\left(|\tilde{\mu}_i|^2\right))$. We observe that *the effective channel gain of any correlated $\mathcal{CN}$-RV can be rewritten as a sum of weighted independent non-central χ^2 variables*, where the weights are related to the covariance matrix.

A closed-form moment-generating function exists for this structure [106]:

$$M_{\mathcal{Q}}(s) = \prod_{i=1}^{n} \exp\left(\frac{\left|\tilde{\mu}_i\right|^2 \lambda_i s}{1 - \lambda_i s}\right) (1 - \lambda_i s)^{-1} , \tag{9.28}$$

but can not be used to derive closed-forms of the corresponding PDF and CDF. Nonetheless, using a slightly modified moment-generating function which converges for approximation order $m \to \infty$ to the intended CGQF [105] gives the following approximation for the PDF:

$$f_{\mathcal{Q}}(x) \approx M_{\mathcal{Q}}\left(\frac{1-m}{x}\right) \frac{(m-1)^m}{x^{m+1}(m-1)!} U_m\left(\frac{1-m}{x}\right) , \tag{9.29}$$

as well as CDF

$$F_{\mathcal{Q}}(x) \approx M_{\mathcal{Q}}\left(\frac{1-m}{x}\right) \sum_{k=0}^{m-1} \frac{(m-1)^k}{x^k k!} U_k\left(\frac{1-m}{x}\right) , \tag{9.30}$$

with auxiliary variables:

$$U_k(s) = \sum_{j=0}^{k-1} \binom{k-1}{j} V_{k-1-j}(s) U_j(s) \tag{9.31}$$

$$V_t(s) = t! \sum_{i=1}^{n} \lambda_i^{t+1} \frac{(t+1)\left|\tilde{\mu}_i\right|^2 - \lambda_i s + 1}{(1 - \lambda_i s)^{t+2}} . \tag{9.32}$$

The variable $U_k(s)$ can be calculated by recursion and builds on $g_t(s)$. Both auxiliary variables grow fast and overflow a floating point number, when the approximation order m grows large. Detection of the overflow allows to gracefully identify the maximum approximation order, where results are still valid.

To improve the numerical properties of the approximation, we reformulate the auxiliary variables in (9.31) and (9.32). The growth rate can be reduced by redistributing the fast growing faculty terms $k!$ and $t!$ as follows:

$$\tilde{U}_k(s) = (-s)^k \frac{U_k(s)}{k!} \tag{9.33}$$

$$\tilde{V}_t(s) = (-s)^t \frac{V_{t-1}(s)}{(t-1)!}. \tag{9.34}$$

This eliminates the binomial in (9.31) and gives the modified auxiliary variables:

$$\tilde{U}_k(s) = \frac{1}{k} \sum_{j=0}^{k-1} \tilde{V}_{k-j}(s) \tilde{U}_j(s), \tag{9.35}$$

$$\tilde{V}_t(s) = (-s)^t \sum_{i}^{n} \lambda_i^t \frac{t\,|\tilde{\mu}_i|^2 - \lambda_i s + 1}{(1-\lambda_i s)^{t+1}}. \tag{9.36}$$

Additionally, the approximations of the PDF and CDF are simplified to:

$$f_{\mathcal{Q}}(x) \approx \frac{m}{x} M_Q\left(\frac{1-m}{x}\right) \tilde{U}_m\left(\frac{1-m}{x}\right), \tag{9.37}$$

$$F_{\mathcal{Q}}(x) \approx M_Q\left(\frac{1-m}{x}\right) \sum_{k=0}^{m-1} \tilde{U}_k\left(\frac{1-m}{x}\right). \tag{9.38}$$

and the local diversity $\mathcal{D}$ [C4] of a quadratic form follows:

$$\mathcal{D}(x) = x\frac{f_{\mathcal{Q}}(x)}{F_{\mathcal{Q}}(x)} \approx m \frac{\tilde{U}_m(\frac{1-m}{x})}{\sum_{k=0}^{m-1} \tilde{U}_k(\frac{1-m}{x})}. \tag{9.39}$$

This form allows to calculate the local diversity as a byproduct of the PDF calculation.

9.5 Examples of Spatial Correlation

This section demonstrates the effect of different PAS, as well as antenna pattern, on the spatial correlation between antenna elements. We will show the differences to the classic case of isotropic antennas in Rayleigh fading.

The spatial correlation is completely described by the covariance matrix $\mathbf{\Sigma}$ and takes into account both, the PAS of the diffuse channel and the directivity of the antenna elements. Here, we only consider uncorrelated scattering for simplicity, but scenarios with correlation between multiple taps can be covered too. First, different PAS (see Fig. 9.2) for ULAs with omni-directional antenna elements are presented and their influence on the correlation coefficients is analysed. Then, antenna element patterns are added into the consideration.

9.5.1 Power Angular Spectra

Omni-directional Channels

The classic Rayleigh channel is omni-directional in two dimensions and has a uniform PAS in azimuth restricted to a single polar angle of $\phi = \pi/2$:

$$p(\theta,\phi) = \tilde{p}(\theta,\phi) = \frac{1}{2\pi}\delta(\phi - \frac{\pi}{2}). \tag{9.40}$$

However, a Rayleigh fading envelope does not necessarily require the diffuse component to be omni-directional. Evaluating the correlation coefficient for a uniformly spaced x-oriented ULA with Δd element spacing gives:

$$\begin{aligned} \rho_{i,j}^{\text{omni}} &= \frac{\delta(n_i - n_j)}{2\pi} \int_0^{2\pi} \exp\left(\mathrm{j}2\pi(m_i - m_j)\frac{\Delta d}{\lambda}\cos\theta\right) d\theta \qquad (9.41) \\ &= \delta(n_i - n_j) J_0\left(2\pi(m_i - m_j)\frac{\Delta d}{\lambda}\right), \qquad (9.42) \end{aligned}$$

where the δ-function ensures uncorrelated taps and $J_0(\cdot)$ is the zero-order Bessel function of the first kind.

The Rice channel needs to account for the $\mathcal{K}$-factor in addition, but the correlation properties stay the same and $\rho_{i,j}^{\text{omni}}$ provides the correlation coefficient. The corresponding PAS, where the available channel power has been normalised, has the following PDF [13, Sec. 6.4.4]:

$$p(\theta,\phi) = \frac{1}{2\pi(\mathcal{K}+1)}\left[1 + 2\pi\mathcal{K}\delta(\theta-\bar{\theta})\right]\delta(\phi-\frac{\pi}{2}), \tag{9.43}$$

where the angle $\bar{\theta}$ defines the direction of the incoming wave responsible for the deterministic part of the channel.

Sector Channel

It is more common in outdoor propagation scenarios with elevated BS, that the diffuse part is restricted to a sector with an opening angle ψ, We are continuing with two-dimensional propagation coming from the horizon and define the sector PAS as:

$$\tilde{p}(\theta,\phi) = \delta(\phi-\frac{\pi}{2})\begin{cases}\frac{1}{\psi} & \text{with } \tilde{\theta}_0-\frac{\psi}{2}\leq\theta\leq\tilde{\theta}_0+\frac{\psi}{2}\\ 0 & \text{otherwise}\end{cases} \tag{9.44}$$

where $\tilde{\theta}_0$ is the directional centre of the diffuse part.

The correlation coefficient resulting from propagation from a uniform diffuse sector impinging on a ULA is

$$\rho_{i,j}^{\text{uni}} = \frac{\delta(n_i-n_j)}{\psi}\int_{\tilde{\theta}-\frac{\psi}{2}}^{\tilde{\theta}+\frac{\psi}{2}}\exp\left(\mathrm{j}2\pi(m_i-m_j)\frac{\Delta d}{\lambda}\cos\theta\right)d\theta. \tag{9.45}$$

This integral can be solved numerically.

A tapered sector model can be achieved with a von Mises distribution[3], to avoid discontinuities in the PAS. The PDF for the diffuse channel PAS is:

$$\tilde{p}(\theta,\phi) = \delta(\phi)\frac{\exp\left(\kappa\cos\left(\theta-\tilde{\theta}_0\right)\right)}{2\pi I_0(\kappa)}, \tag{9.46}$$

---

[3] The circular equivalent to the real Gaussian distribution.

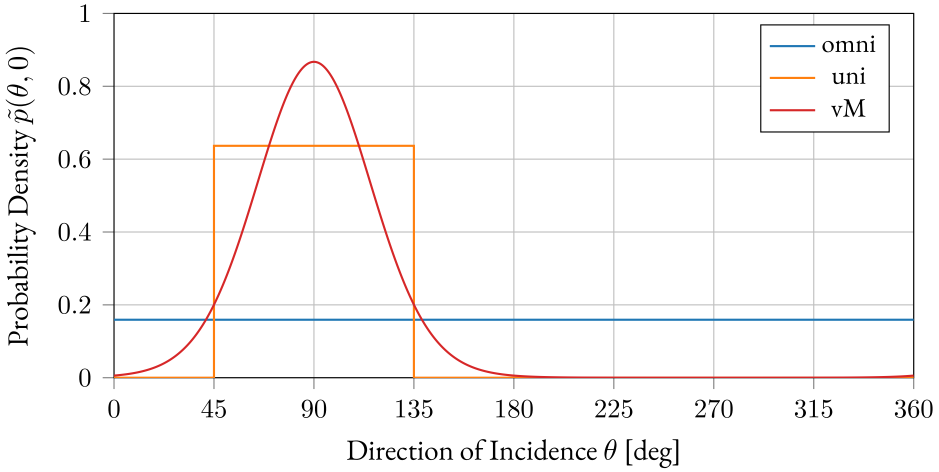

Figure 9.2: Power angular spectra for three different scenarios are shown, namely an omnidirectional channel (omni), an uniform sector channel (uni, $\alpha = 90°$, $\tilde{\theta}_0 = 90°$) and a von Mises channel (vM, $\kappa = 5$, $\tilde{\theta}_0 = 90°$).

where κ is a concentration measure. The correlation coefficient can be calculated by solving (9.17) numerically.

In Fig. 9.2 three different diffuse PAS are displayed. The corresponding correlation function for two omni-directional elements separated in x-direction are shown in Fig. 9.3. It is clear that the actual distribution of the PAS has a strong influence on the spatial correlation between antenna elements. The wider the sector of the diffuse component is, the slower is the decay of the correlation coefficient magnitude.

9.5.2 Antenna Element Pattern

The actually observable diffuse part of the channel depends not only on the direction of the incoming diffuse waves, but on the antenna element pattern in addition. For simplicity, we are continuing with the specialisation to two-dimensions.

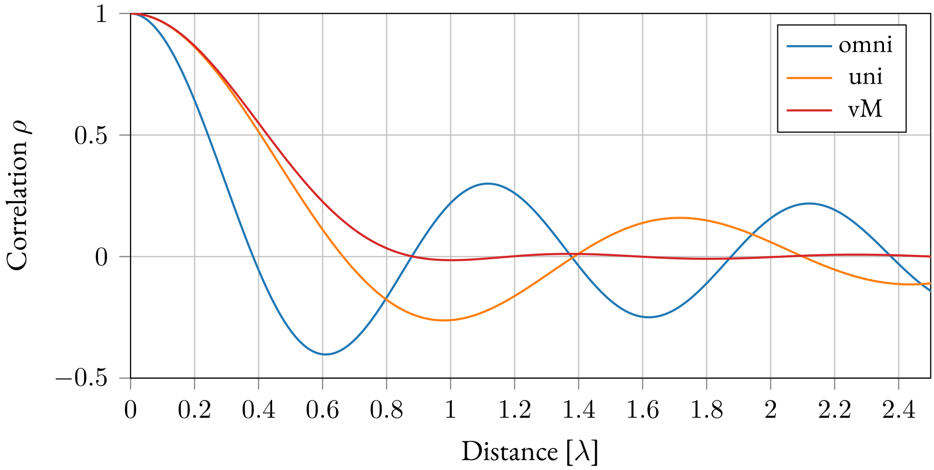

Figure 9.3: The correlation between two omni-directional antenna elements spaced at a distance in x-direction is shown for the three different PASs in Fig. 9.2.

The directivity D of each antenna element is described by the shape of the antenna pattern $F(\theta, \phi)$ and the maximum directivity D_0:

$$D(\theta, \phi) = D_0 F(\theta, \phi). \tag{9.47}$$

A generic uni-directional two-dimensional antenna pattern can be modeled as a cosine to the power of ζ [107], where θ_0 fixes the azimuth angle for D_0:

$$F(\theta, \phi) = \begin{cases} \cos^{\zeta}(\theta - \theta_0)\delta(\phi - \frac{\pi}{2}) & \theta_0 - \frac{\pi}{2} \le \theta \le \theta_0 + \frac{\pi}{2} \\ 0 & \text{elsewhere.} \end{cases} \tag{9.48}$$

The higher ζ is, the more directional the antenna pattern. The half power beam width can be derived by evaluating $F(\theta, \phi) = 1/2$:

$$\theta_{\text{HPBW}} = 2 \arccos\left(\sqrt[\zeta]{\frac{1}{2}}\right). \tag{9.49}$$

The maximum directivity with respect to an isotropic source can be evaluated

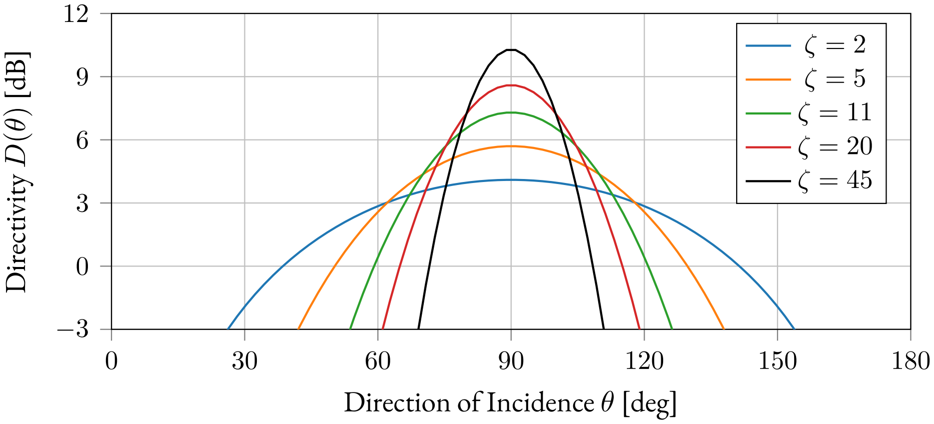

Figure 9.4: Directivity of the uni-directional generic $\cos^{\zeta}(\theta - \theta_0)$ antenna element for $\theta_0 = 90°$

by:

$$D_0 = \frac{4\pi}{\iint_{\Omega} F(\theta, \phi) d\Omega}. \tag{9.50}$$

The pattern for different ζ is shown in Fig. 9.4 and the maximum directivity and half power beam width are presented in Table 9.1.

The antenna gain in section 9.3 is connected to the directivity via the antenna efficiency ϵ:

$$G(\theta, \phi) = \eta D(\theta, \phi) \tag{9.51}$$

For the generic $cos^{\zeta}(\theta - \theta_0)$, the correlation coefficient in (9.17) can be simplified

Table 9.1: Properties of the generic uni-directional $\cos^{\zeta}(\theta - \theta_0)$ antenna element

ζ	0	2	5	11	20	45
D_0 [dB]	1.0	4.1	5.7	7.3	8.6	10.3
θ_{HPBW}	(180°)	90°	59°	40°	30°	20°

$$\rho^{t}_{m_i,m_j} = \frac{D_0}{4\pi}\int_{\max\left(\theta_{0_i}-\frac{\pi}{2},\theta_{0_j}-\frac{\pi}{2}\right)}^{\min\left(\theta_{0_i}+\frac{\pi}{2},\theta_{0_j}+\frac{\pi}{2}\right)} \sqrt{\cos^{\zeta}(\theta-\theta_{0_i})\cos^{\zeta}(\theta-\theta_{0_j})}\;\exp\left(\mathrm{j}\Delta\varphi_{m_i,m_j}(\theta,\frac{\pi}{2})\right)d\theta \qquad (9.52)$$

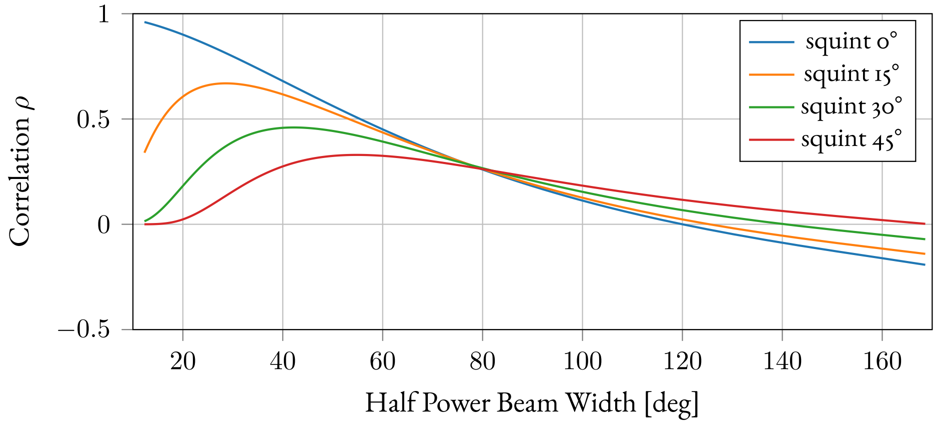

Figure 9.5: The correlation between two antenna elements spaced at a distance of 0.5 λ is shown for different squint angles.

as shown in (9.52). Fig. 9.5 depicts the influence of the directivity of the antenna elements on the correlation coefficient at an element spacing of $\lambda/2$. The more directive the antenna elements are, the higher the correlation coefficient for ULAs (squint angle 0°). If the elements are squinting into different directions (e.g. if they are distributed over an arc), then the behaviour changes and the correlation falls off once both beams stop to overlap.

9.6 Simulations

In the following section, simulation results are presented, to verify the approximations due to the confluent CGQF. To illustrate the versatility of the method, we

Table 9.2: Overview over simulated scenarios with power angular spectrum for uncorrelated (uc), omnidirectional (omni) and von Mises channels.

Scenario	Verification		Array Configurations
Array Layout	ULA		half circle & ULA
# of Antennas M	32		32
# of Taps N	1		1
Ant. Element ζ	0		2 & 5 & 20
PAS	uc & omni	von Mises	von Mises (aligned)
Rician Factor $\mathcal{K}$	0	4	0 & 4
Determ. Dir. $\bar{\theta}$		70°	30° & 60°
Concentration κ		5	5
Diffuse Dir. $\tilde{\theta}_0$		70° & 90°	30° & 60°

compare a ULA BS with a half-circle BS layout for antenna elements with varying directivity. This shall demonstrate how the introduced model allows a simple performance evaluation of correlated Rician radio channels under consideration of antenna element pattern, array layout and Rician fading channels. The different scenarios are summarised in Table 9.2.

9.6.1 Verification

To verify that the analytic approximations provide accurate results, a number of diffuse plane waves impinging on an ULA with isotropic antenna elements are simulated. The 32 antenna element ULA with $\lambda/2$ spacing in x-direction is situated in a single tap Rician fading environment with $\mathcal{K}$-factor 4 for four different PAS:

- uncorrelated
- omnidirectional diffuse scattering
- von Mises scattering aligned with deterministic component ($\kappa = 5, \bar{\theta} = \tilde{\theta}_0 = 70°$)

- von Mises scattering squinting with respect to the deterministic component $(\kappa = 5, \bar{\theta} = 70^\circ, \tilde{\theta}_0 = 90^\circ)$

The uncorrelated simulation adhering to (9.6) and (9.7) is generating independent plane waves for each antenna element, whilst the other three simulations have the same plane waves impinging on all elements. The empirical CDFs are based on 1×10^6 trials with 800 plane waves forming the diffuse channel according to the PAS.

These verification settings cover wide-band results up to a certain number of taps too, since both taps and antennas link to $\mathcal{CN}$-RV elements. The multi-antenna single-tap case allows for a fully populated correlation matrix in our uncorrelated scattering setting and is therefore more challenging than a single antenna 32 tap scenario.

The CDFs are shown in Fig. 9.6. Simulations and approximations give consistent results for all cases. It is important to note, that uncorrelated antenna elements do *not* in general provide the best results once the channel shows Rician fading. It depends on the superposition of the phases that the deterministic and diffuse component cause on the antenna elements. A certain correlation between close antenna elements improves the situation if the diffuse component is orthogonal to the deterministic component. This reduces the probability that the diffuse component acts destructively on the deterministic component, since they align over close antenna elements. This effect is visible both, in comparison with the uncorrelated and omni-directional PAS and for the aligned and squinting von Mises scattering. Nonetheless, for real scenarios it is highly probable the deterministic and the diffuse component are aligned (e.g. von Mises aligned case), leading to a loss of performance over the uncorrelated case.

The corresponding local diversity is presented in Fig. 9.7. The classic diversity would be 32 for a BS with 32 uncorrelated antenna elements. The local diversity at interesting outage probabilities is heavily depending on the PAS of the diffuse component. Additionally, it is not predictable from the number of array elements only [C4].

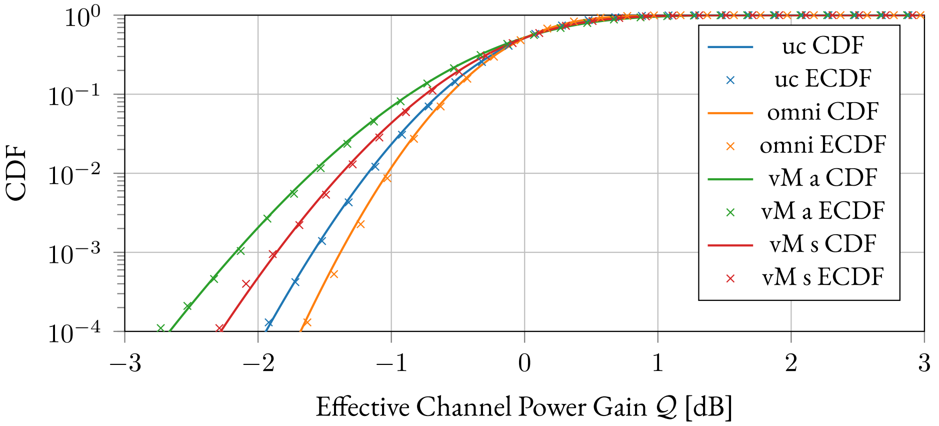

Figure 9.6: Verification of the cumulative distribution functions (CDFs) approximated by complex Gaussian quadratic forms for a 32 antenna element uniform linear array in a single tap fading environment with $\mathcal{K}$-factor 4. The empirical cumulative distribution functions (ECDF) are generated from simulation results. Four different power angular spectrum are evaluated: uncorrelated (uc), omni-directional (omni), von Mises aligned (vM a) and von Mises squinting (vM s). The approximations provide accurate results for the correlated and uncorrelated cases.

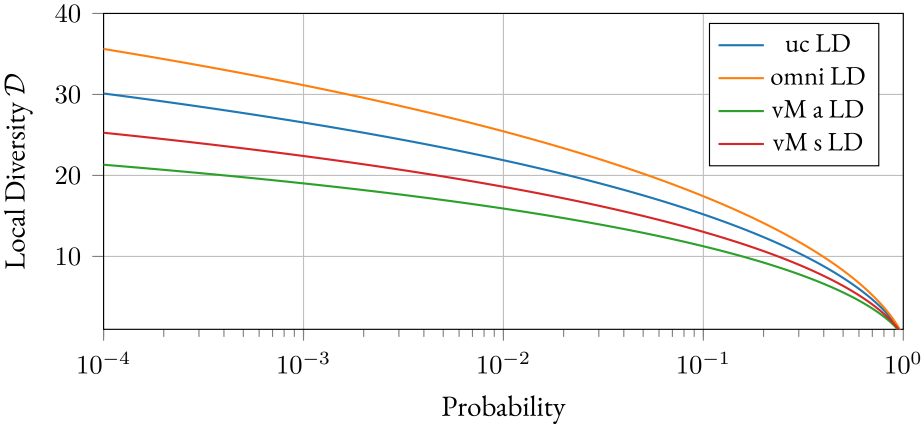

Figure 9.7: The local diversity approximated by complex Gaussian quadratic forms for a 32 antenna element uniform linear array in a single tap fading environment with isotropic antenna pattern is shown for the four verification scenarios in Fig. 9.6.

9.6.2 Array Configurations

Here, we want to analyse the implications of two different BS array configurations in aligned von Mises scattering from different angles with $\mathcal{K}$-factors zero and 4. An ULA is the reference configuration, since it is used abundantly for theoretical discussions due to its mathematical tractability. Equipped with directional antenna elements it could model a BS mounted to a building edge fairly well. As alternative, the elements will be distributed over a half circle to reduce the extent in one direction, whilst increasing it into the other. Hence, with the same directional elements, a wider sector will be illuminated more evenly, reducing the maximum gain into broadside direction. Both configurations are sketched in Fig. 9.8.

Fig. 9.9 shows results for different von Mises PASs. Solid lines and dashed lines indicate the ULA and half circle BS layout, respectively. In general, high directivity of the antenna elements is not giving advantages in the considered cases. The reason is that the main direction of the elements has to match the direction of the incoming waves, but it is not steerable. The penalty for higher gain elements

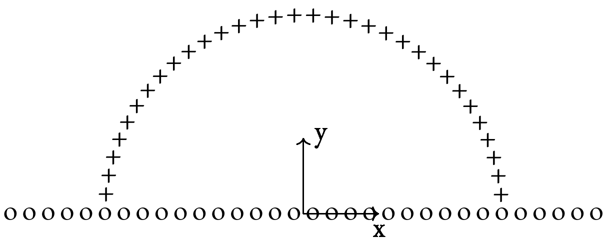

Figure 9.8: Array configuration of the ULA (o) and half circle array (+).

is lower in the half circle arrangement, since at least a few antennas are pointing towards a possible user.

For the low directivity elements, a deterministic channel component can be used efficiently, since the array factor allows coherent combination. In the high directivity case, at least one element needs to be aligned. The more a user is received towards the end-fire direction of the ULA, the better is the half circle configuration in comparison. Eventually, the half circle BS provides a more evenly distributed coverage and is less sensitive to the direction of the incoming waves. Furthermore, in multi-user applications, different users are more likely to have stronger contributions to different antenna element subsets of the half circle array.

Fig. 9.10 presents the local diversities for the two BS under different fading conditions. Only the low directivity case ($\zeta = 2$) has been taken into account, to allow for visual comparison of the influence of different PASs. Both, uncorrelated Rayleigh and Rician fading provide more local diversity than their counterparts with constricted PAS. The half circle BS has always less local diversity in comparison to the ULA BS. This is due to fewer antenna elements being illuminated by the diffuse component, that provides spatial diversity. A higher $\mathcal{K}$-factor provides a higher local diversity for all cases, since it becomes more unlikely that the diffuse component of the channel cancels the deterministic component out.

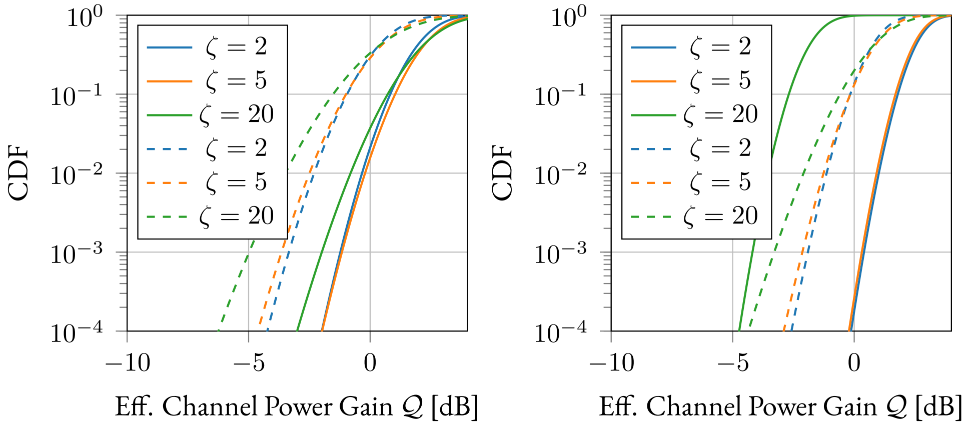

(a) $\mathcal{K} = 0, \tilde{\theta}_0 = 60°$ **(b)** $\mathcal{K} = 4, \bar{\theta} = \tilde{\theta}_0 = 60°$

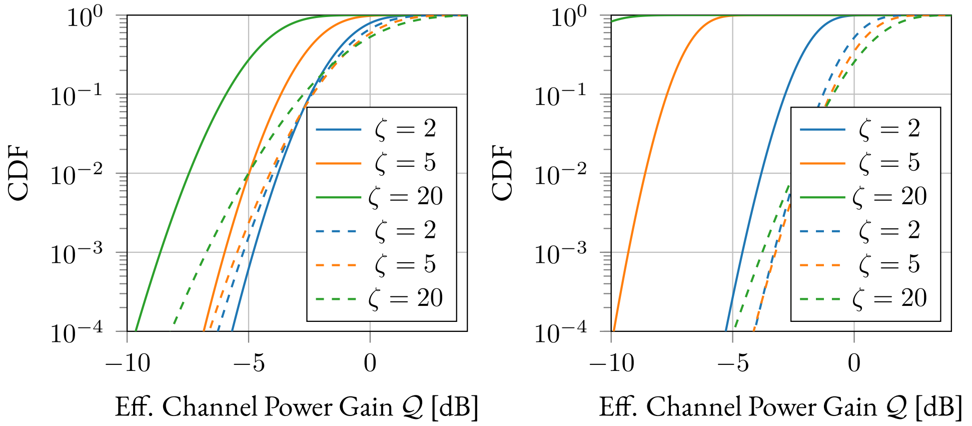

(c) $\mathcal{K} = 0, \tilde{\theta}_0 = 30°$ **(d)** $\mathcal{K} = 4, \bar{\theta} = \tilde{\theta}_0 = 30°$

Figure 9.9: The plots show the effective channel for different directivities (colours), power angular spectrums with concentration $\kappa = 5$ of a uniform linear array (ULA) (solid lines), and half circle array (dashed lines). The ULA performance is more dependent on broadside incidence of the waves, than the half circle array, especially for higher directivity elements. In all shown scenarios (parameters given below the subfigures) is lower directivity more beneficial and the half circle arrangement trades peak directivity towards broadside with increased directivity towards the end-fire direction of the ULA.

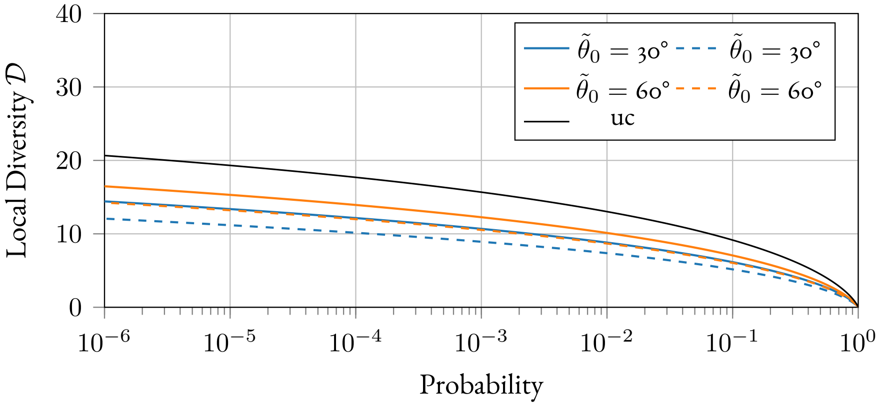

(a) $\mathcal{K} = 0$

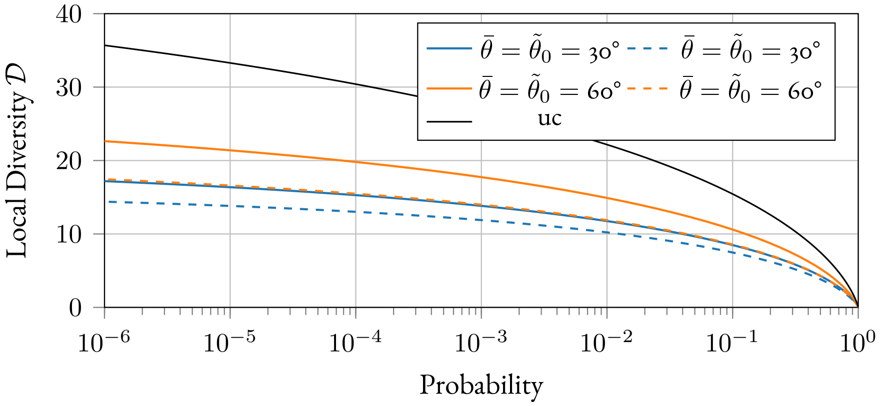

(b) $\mathcal{K} = 4$

Figure 9.10: Local diversities are shown for the uniform linear array (solid line) and half circle (dashed line) base station with low directivity elements ($\zeta = 2$). The different colours correspond to different von Mises power angular spectrum with parameters given in the legend for two different $\mathcal{K}$-factors. In general, the half circle BS has less local diversity at a certain outage probability. Moreover, a higher $\mathcal{K}$-factor gives higher local diversity. All constricted cases of diffuse scattering provide less local diversity than the uncorrelated (uc) Rayleigh (solid black) channel.

9.7 Discussion

The proposed correlated Rician model increases the realism and complexity of a massive MIMO BS propagation analysis over simpler uncorrelated models. Additionally, antenna array geometry, antenna element orientation and PASs have been accounted for to determine the covariance matrix of the $\mathcal{CN}$-RV, allowing for evaluation of different BS designs for a given scenario. The parameters of the $\mathcal{CN}$-RV can alternatively be based on the simplified 3rd Generation Partnership Project Urban Microcell model as described in [94] and our CGQFs approach still gives the PDF and CDF of the effective channel. Furthermore, the method can be generalised to handle e.g. power variation between antenna elements through the operator matrix.

Covariance is sometimes elusive and hard to measure properly in the field. However, by inspection of the quadratic form in (9.27), it is clear, that the properties of the eigenvalues of the covariance matrix are of central relevance to capture the effect of correlation on the effective channel. Moreover, considering *universality* in random matrix theory [58], the distribution of eigenvalues behaves asymptotically as if the matrix elements are Gaussian distributed. Therefore, the CGQF results are less sensitive to the actual individual correlation coefficients.

So far, we only demonstrated over-the-horizon propagation with the example PASs. Nonetheless, the described framework allows for three-dimensional considerations. The impact of incoming waves from different elevation angles depends obviously on the weighting imposed by antenna element pattern and array geometry. In general, additional local diversity is available, but the BS design needs to take this into account to benefit from it. The proposed model is flexible enough to allow BS performance comparisons for a combination of surface and aerial users.

9.8 Conclusion

A thorough way of handling correlated Rician fading for LSASs has been presented. The accurate approximations can be used to analyse the effective channel of massive MIMO BSs. The framework allows consideration of inter-tap correlation in addition to the outlined antenna correlations. Inter-tap correlation can occur, e.g. if distributed antenna arrays are spaced further apart than the distance related to the duration of a single tap.

The provided correlated $\mathcal{CN}$-RV channel model is general and the $\mathcal{K}$-factor parameterisation allows investigation of Rician and Rayleigh fading at each antenna and delay tap with arbitrary correlation coefficients. Correlation coefficients have been related to the PAS of the diffuse channel component and consider the antenna element pattern in addition. A plane wave model provides the foundation of the complex normal element statistics and the tractability of correlation coefficients. To capture near-field aspects that become more prominent for larger apertures, future research should investigate the differences that a spherical wave model would introduce.

Low-directivity antenna elements provide better overall system performance than high-directivity elements, once the BS grows to a reasonable size. This is mainly caused by being less prone to the direction of incoming waves, because the main gain is coming from the steerable array factor and not the static element factor. Arranging the elements in a half-circle illuminates a region more evenly than a ULA, but reduces the peak gain for broad-side radiation. Moreover, the local diversity is reduced for the half-circle BS and a directional diffuse part since fewer elements pick up significant energy, even though they are less correlated. A thorough analysis of the system performance would, in addition to the presented channel properties, need to include hardware imperfections like phase noise and timing jitter.

The complete statistic of the effective channel gain for correlated Rician fading channels is described through the provided PDF or CDF. This allows the investigation of instantaneous metrics of the single user performance beyond the mean and variance of the combined received signal.

Bibliography

[J1] G. Ghiaasi, J. Abraham, E. Eide, and T. Ekman, "Effective Channel Hardening in an Indoor Multiband Scenario", *International Journal of Wireless Information Networks*, vol. 26, no. 4, Jul. 2019. DOI: `10.1007/s10776-019-00438-7`.

[J2] J. Abraham, P. Ramírez-Espinosa, and T. Ekman, "Statistics of the Effective Massive MIMO Channel in Correlated Rician Fading", *IEEE Open Journal of Antennas and Propagation*, vol. 3, pp. 238–248, Jan. 2022. DOI: `10.1109/OJAP.2022.3147015`. arXiv: `2112.06692`.

[C1] J. Abraham and T. Ekman, "Power Inversion of the Massive MIMO Channel", in *Proceedings of the 2019 Symposium on Information Theory and Signal Processing in the Benelux (SITB2019)*, arXiv:1905.07555, Gent, Belgium: Werkgemeenschap Informatie- en Communicatietheorie (WIC) & IEEE Benelux Signal Processing Chapter, May 2019, pp. 3–7.

[C2] ——, "Achievable Synchronisation Gain In Uncalibrated Large Scale Antenna Systems", in *2020 14th European Conference on Antennas and Propagation (EuCAP)*, Mar. 2020, pp. 1–5. DOI: `10.23919/EuCAP48036.2020.9136063`.

[C3] ——, "Fading Margins for Large-Scale Antenna Systems", in *ICC 2021 - IEEE International Conference on Communications*, Montreal, QC, Canada: IEEE, Jun. 2021, pp. 1–5. DOI: `10.1109/ICC42927.2021.9500328`. arXiv: `2102.09903`.

[C4] ——, "Local Diversity and Ultra-Reliable Antenna Arrays", in *2021 55th Asilomar Conference on Signals, Systems and Computers*, Nov. 2021. arXiv: `2108.00712`, submitted and presented.

[R1] G. Ghiaasi, J. Abraham, E. Eide, and T. Ekman, "Measured Channel Hardening in an Indoor Multiband Scenario", in *2018 IEEE 29th Annual International Symposium on Personal, Indoor and Mobile Radio Communications (PIMRC)*, arXiv:1812.05463, Bologna, Italy, Sep. 2018, pp. 1–6. DOI: `10.1109/PIMRC.2018.8581026`.

[I1] ——, "Measured Channel Hardening in an Indoor Multiband Scenario", TD(18)07023, 7th technical IRACON meeting, Cartagena, Spain, May 2018.

[I2] J. Abraham, G. Ghiaasi, and T. Ekman, "Characterisation of Channel Hardening Using the Diversity Order of the Effective Channel", TD(19)09072, 9th technical IRACON meeting, Dublin, Ireland, Jan. 2019.

[I3] J. Abraham and T. Ekman, "Achievable Synchronisation Gain in Uncalibrated Large Scale Antenna Systems", TD(20)12011, 12th technical IRACON meeting, Louvain-la-Neuve, Belgium, Jan. 2020.

[A1] H. Bui Van, J. Abraham, Q. Gueuning, E. de Lera Acedo, and C. Craeye, “Further validation of fast simulation method at the element and array pattern levels for SKA”, in *2016 10th European Conference on Antennas and Propagation (EuCAP)*, Apr. 2016, pp. 1–4. DOI: `10.1109/EuCAP.2016.7481791`.

[A2] J. Abraham, E. Colin-Beltran, E. de Lera Acedo, and A. J. Faulkner, “A 16-element LPDA random sparse prototype array for the SKA AA-mid instrument”, in *2016 10th European Conference on Antennas and Propagation (EuCAP)*, Apr. 2016, pp. 1–4. DOI: `10.1109/EuCAP.2016.7481792`.

[A3] J. Abraham, H. B. Van, E. de Lera Acedo, and C. Craeye, “Numerical modelling of SKA AA-Mid tile configurations using HARP”, in *2017 11th European Conference on Antennas and Propagation (EUCAP)*, Mar. 2017, pp. 3837–3841. DOI: `10.23919/EuCAP.2017.7928253`.

[A4] H. Bui-Van, J. Abraham, M. Arts, Q. Gueuning, C. Raucy, D. González-Ovejero, E. de Lera Acedo, and C. Craeye, “Fast and Accurate Simulation Technique for Large Irregular Arrays”, *IEEE Transactions on Antennas and Propagation*, vol. 66, no. 4, pp. 1805–1817, Apr. 2018. DOI: `10.1109/TAP.2018.2806222`.

[A5] E. de Lera Acedo, H. Pienaar, N. R. Ghods, *et al.*, “SKA LFAA Station Design Report”, Tech. Rep., Mar. 2020, arXiv: 2003.12744.

[1] “802.11ax-2021 - IEEE Standard for Information Technology–Telecommunications and Information Exchange between Systems Local and Metropolitan Area Networks–Specific Requirements Part 11: Wireless LAN Medium Access Control (MAC) and Physical Layer (PHY) Specifications Amendment 1: Enhancements for High-Efficiency WLAN”, IEEE, Tech. Rep., May 19, 2021, ISBN: 9781504473897. DOI: `10.1109/IEEESTD.2021.9442429`.

[2] “3gpp TR 21.916 V16.0.1 - 3rd Generation Partnership Project; Technical Specification Group Services and System Aspects; Release 16 Description; Summary of Rel-16 Work Items (Release 16)”, 3GPP, Tech. Rep., Sep. 14, 2021.

[3] C. Shannon, “Communication In The Presence Of Noise”, *Proceedings of the IEEE*, vol. 86, no. 2, pp. 447–457, Feb. 1998. DOI: `10.1109/JPROC.1998.659497`.

[4] K. Luo, S. Dang, B. Shihada, and M.-S. Alouini, “PHY Research Is Sick But Curable: An Empirical Analysis”, Aug. 16, 2019. arXiv: `1908.06035`.

[5] “ITU-R M.2410-0 – Minimum requirements related to technical performance for IMT-2020 radio interface(s)”, ITU, Tech. Rep., Nov. 2017.

[6] A.-S. Bana, E. de Carvalho, B. Soret, T. Abrão, J. C. Marinello, E. G. Larsson, and P. Popovski, “Massive MIMO for Internet of Things (IoT) connectivity”, *Physical Communication*, vol. 37, p. 100 859, Dec. 2019, arXiv:1905.06205. DOI: `10.1016/j.phycom.2019.100859`.

[7] A. Chawla, A. S. Sarode, A. K. Jagannatham, and L. Hanzo, “Distributed Parameter Detection in Massive MIMO Wireless Sensor Networks Relying on Imperfect CSI”, *IEEE Transactions on Wireless Communications*, vol. 20, no. 1, pp. 506–519, Jan. 2021. doi: 10.1109/TWC.2020.3025877.

[8] L. Sanguinetti, E. Björnson, and J. Hoydis, “Toward Massive MIMO 2.0: Understanding Spatial Correlation, Interference Suppression, and Pilot Contamination”, *IEEE Trans. Commun.*, vol. 68, no. 1, pp. 232–257, Jan. 2020, arXiv: 1904.03406. doi: 10.1109/TCOMM.2019.2945792.

[9] L. R. Kahn, “Ratio Squarer”, *Proceedings of the IRE*, vol. 42, no. 11, p. 1704, 1954. doi: 10.1109/JRPROC.1954.274666.

[10] T. K. Y. Lo, “Maximum ratio transmission”, in *1999 IEEE International Conference on Communications*, vol. 2, Jun. 1999, 1310–1314 vol.2. doi: 10.1109/ICC.1999.765552.

[11] C. Oestges, A. D. Kim, G. Papanicolaou, and A. J. Paulraj, “Characterization of space-time focusing in time-reversed random fields”, *IEEE Transactions on Antennas and Propagation*, vol. 53, no. 1, pp. 283–293, Jan. 2005. doi: 10.1109/TAP.2004.836399.

[12] H. H. Andersen, M. Højbjerre, D. Sørensen, and P. S. Eriksen, “The Multivariate Complex Normal Distribution”, in *Linear and Graphical Models*, ser. Lecture Notes in Statistics, Springer, New York, NY, 1995, pp. 15–37. doi: 10.1007/978-1-4612-4240-6_2.

[13] G. D. Durgin, *Space-Time Wireless Channels*, ser. Prentice Hall communications engineering and emerging technologies series. Upper Saddle River, NJ: Prentice Hall PTR, 2003.

[14] A. Gil, J. Segura, and N. M. Temme, “Algorithm 939: Computation of the Marcum Q-Function”, *ACM Transactions on Mathematical Software*, vol. 40, no. 3, pp. 1–21, Apr. 2014. doi: 10.1145/2591004.

[15] H. Ruben, “Non-central chi-square and gamma revisited”, *Communications in Statistics*, vol. 3, no. 7, pp. 607–633, Jan. 1974. doi: 10.1080/03610927408827163.

[16] T. L. Marzetta, “Noncooperative Cellular Wireless with Unlimited Numbers of Base Station Antennas”, *IEEE Trans. Wireless Commun.*, vol. 9, no. 11, pp. 3590–3600, Nov. 2010. doi: 10.1109/TWC.2010.092810.091092.

[17] P. Harris, W. B. Hasan, S. Malkowsky, *et al.*, “Serving 22 Users in Real-Time with a 128-Antenna Massive MIMO Testbed”, in *2016 IEEE International Workshop on Signal Processing Systems (SiPS)*, IEEE, Oct. 2016, pp. 266–272. doi: 10.1109/SiPS.2016.54.

[18] E. Björnson, L. Sanguinetti, H. Wymeersch, J. Hoydis, and T. L. Marzetta, “Massive MIMO is a reality—What is next?”, *Digital Signal Processing*, vol. 94, pp. 3–20, Nov. 2019, arXiv: 1902.07678. doi: 10.1016/j.dsp.2019.06.007.

[19] E. Björnson, J. Hoydis, and L. Sanguinetti, *Massive MIMO Networks: Spectral, Energy, and Hardware Efficiency*, 3-4. 2017, vol. 11, pp. 154–655. DOI: `10.1561/2000000093`.

[20] K. Scharnhorst, "Angles in Complex Vector Spaces", *Acta Applicandae Mathematica*, vol. 69, no. 1, pp. 95–103, Oct. 2001. DOI: `10.1023/A:1012692601098`.

[21] N. O'Donoughue and J. M. F. Moura, "On the Product of Independent Complex Gaussians", *IEEE Transactions on Signal Processing*, vol. 60, no. 3, pp. 1050–1063, Mar. 2012. DOI: `10.1109/TSP.2011.2177264`.

[22] E. Larsson, O. Edfors, F. Tufvesson, and T. Marzetta, "Massive MIMO for next generation wireless systems", *IEEE Commun. Mag.*, vol. 52, no. 2, pp. 186–195, Feb. 2014. DOI: `10.1109/MCOM.2014.6736761`.

[23] T. L. Marzetta, "Massive MIMO: An Introduction", *Bell Labs Technical Journal*, vol. 20, pp. 11–22, Mar. 2015. DOI: `10.15325/BLTJ.2015.2407793`.

[24] T. L. Marzetta, E. G. Larsson, H. Yang, and H. Q. Ngo, *Fundamentals of Massive MIMO*. Cambridge, United Kingdom ; New York: Cambridge University Press, Nov. 2016.

[25] E. Björnson, E. G. Larsson, and T. L. Marzetta, "Massive MIMO: Ten myths and one critical question", *IEEE Commun. Mag.*, vol. 54, no. 2, pp. 114–123, Feb. 2016. DOI: `10.1109/MCOM.2016.7402270`.

[26] F. Rottenberg, T. Choi, P. Luo, C. J. Zhang, and A. F. Molisch, "Performance Analysis of Channel Extrapolation in FDD Massive MIMO Systems", *IEEE Transactions on Wireless Communications*, vol. 19, no. 4, pp. 2728–2741, Apr. 2020. DOI: `10.1109/TWC.2020.2967711`.

[27] L. Van der Perre, E. G. Larsson, F. Tufvesson, L. D. Strycker, E. Bjornson, and O. Edfors, "RadioWeaves for efficient connectivity: Analysis and impact of constraints in actual deployments", in *2019 53rd Asilomar Conference on Signals, Systems, and Computers*, Pacific Grove, CA, USA: IEEE, Nov. 2019, pp. 15–22. DOI: `10.1109/IEEECONF44664.2019.9048825`.

[28] H. Q. Ngo, A. Ashikhmin, H. Yang, E. G. Larsson, and T. L. Marzetta, "Cell-Free Massive MIMO Versus Small Cells", *IEEE Transactions on Wireless Communications*, vol. 16, no. 3, pp. 1834–1850, Mar. 2017. DOI: `10.1109/TWC.2017.2655515`.

[29] E. Björnson, Ö. T. Demir, and L. Sanguinetti, "A Primer on Near-Field Beamforming for Arrays and Reconfigurable Intelligent Surfaces", arXiv: 2110.06661, Oct. 2021.

[30] V. Tapio, I. Hemadeh, A. Mourad, A. Shojaeifard, and M. Juntti, "Survey on reconfigurable intelligent surfaces below 10 GHz", *EURASIP Journal on Wireless Communications and Networking*, vol. 2021, no. 1, p. 175, Dec. 2021. DOI: `10.1186/s13638-021-02048-5`.

[31] S. Buzzi, C. D'Andrea, and M. Lops, "Using Massive MIMO Arrays for Joint Communication and Sensing", in *2019 53rd Asilomar Conference on Signals, Systems, and Computers*, Pacific Grove, CA, USA: IEEE, Nov. 2019, pp. 5–9. DOI: `10.1109/IEEECONF44664.2019.9048857`.

[32] C. Studer, S. Medjkouh, E. Gonultas, T. Goldstein, and O. Tirkkonen, "Channel Charting: Locating Users Within the Radio Environment Using Channel State Information", *IEEE Access*, vol. 6, pp. 47 682–47 698, 2018. DOI: `10.1109/ACCESS.2018.2866979`.

[33] J. Deng, S. Medjkouh, N. Malm, O. Tirkkonen, and C. Studer, "Multipoint Channel Charting for Wireless Networks", in *2018 52nd Asilomar Conference on Signals, Systems, and Computers*, Pacific Grove, CA, USA: IEEE, Oct. 2018, pp. 286–290. DOI: `10.1109/ACSSC.2018.8645281`.

[34] N. Shlezinger, R. Fu, and Y. C. Eldar, "DeepSIC: Deep Soft Interference Cancellation for Multiuser MIMO Detection", *IEEE Transactions on Wireless Communications*, vol. 20, no. 2, pp. 1349–1362, Feb. 2021. DOI: `10.1109/TWC.2020.3032663`.

[35] S. O. Rice, "Statistical Properties of a Sine Wave Plus Random Noise", *Bell System Technical Journal*, vol. 27, no. 1, pp. 109–157, Jan. 1948. DOI: `10.1002/j.1538-7305.1948.tb01334.x`.

[36] L. Liu, C. Oestges, J. Poutanen, K. Haneda, P. Vainikainen, F. Quitin, F. Tufvesson, and P. Doncker, "The COST 2100 MIMO channel model", *IEEE Wireless Communications*, vol. 19, no. 6, pp. 92–99, Dec. 2012. DOI: `10.1109/MWC.2012.6393523`.

[37] X. Gao, F. Tufvesson, and O. Edfors, "Massive MIMO channels – Measurements and models", in *2013 Asilomar Conference on Signals, Systems and Computers*, Nov. 2013, pp. 280–284. DOI: `10.1109/ACSSC.2013.6810277`.

[38] X. Gao, O. Edfors, F. Rusek, and F. Tufvesson, "Massive MIMO Performance Evaluation Based on Measured Propagation Data", *IEEE Trans. Wireless Commun.*, vol. 14, no. 7, pp. 3899–3911, Jul. 2015. DOI: `10.1109/TWC.2015.2414413`.

[39] J. Flordelis, X. Li, O. Edfors, and F. Tufvesson, "Massive MIMO Extensions to the COST 2100 Channel Model: Modeling and Validation", *IEEE Transactions on Wireless Communications*, vol. 19, no. 1, pp. 380–394, Jan. 2020. DOI: `10.1109/TWC.2019.2945531`.

[40] S. Gunnarsson, J. Flordelis, L. Van Der Perre, and F. Tufvesson, "Channel Hardening in Massive MIMO: Model Parameters and Experimental Assessment", *IEEE Open Journal of the Communications Society*, vol. 1, pp. 501–512, 2020, arXiv:2004.06772. DOI: `10.1109/OJCOMS.2020.2987704`.

[41] S. Jaeckel, L. Raschkowski, K. Borner, and L. Thiele, "QuaDRiGa: A 3-D Multi-Cell Channel Model With Time Evolution for Enabling Virtual Field Trials", *IEEE Transactions on Antennas and Propagation*, vol. 62, no. 6, pp. 3242–3256, Jun. 2014. DOI: `10.1109/TAP.2014.2310220`.

[42] A. O. Martinez, P. Eggers, and E. De Carvalho, "Geometry-based stochastic channel models for 5G: Extending key features for massive MIMO", in *2016 IEEE 27th Annual International Symposium on Personal, Indoor, and Mobile Radio Communications (PIMRC)*, Valencia, Spain: IEEE, Sep. 2016, pp. 1–6. DOI: `10.1109/PIMRC.2016.7794648`.

[43] M. Z. Aslam, Y. Corre, E. Björnson, and E. G. Larsson, "Performance of a dense urban massive MIMO network from a simulated ray-based channel", *EURASIP Journal on Wireless Communications and Networking*, vol. 2019, no. 1, p. 106, Dec. 2019. DOI: `10.1186/s13638-019-1425-1`.

[44] C. Shepard, J. Ding, R. E. Guerra, and L. Zhong, "Understanding real many-antenna MU-MIMO channels", in *2016 50th Asilomar Conference on Signals, Systems and Computers*, Nov. 2016, pp. 461–467. DOI: `10.1109/ACSSC.2016.7869082`.

[45] C.-M. Chen, A. P. Guevara, and S. Pollin, "Scaling up distributed massive MIMO: Why and how", in *2017 51st Asilomar Conference on Signals, Systems, and Computers*, ISSN: 2576-2303, Oct. 2017, pp. 271–276. DOI: `10.1109/ACSSC.2017.8335182`.

[46] A. P. Guevara, C.-M. Chen, and S. Pollin, "Hardware and spectrum sharing for distributed massive MIMO", in *2018 52nd Asilomar Conference on Signals, Systems, and Computers*, Pacific Grove, CA, USA: IEEE, Oct. 2018, pp. 619–623. DOI: `10.1109/ACSSC.2018.8645516`.

[47] C.-M. Chen, Q. Wang, A. Gaber, A. P. Guevara, and S. Pollin, "Experimental study of user selection for dense indoor massive MIMO", in *IEEE INFOCOM 2019 - IEEE Conference on Computer Communications Workshops (INFOCOM WKSHPS)*, Paris, France: IEEE, Apr. 2019, pp. 602–607. DOI: `10.1109/INFCOMW.2019.8845117`.

[48] S. De Bast, A. P. Guevara, and S. Pollin, "CSI-based positioning in massive MIMO systems using convolutional neural networks", in *2020 IEEE 91st Vehicular Technology Conference (VTC2020-Spring)*, Antwerp, Belgium, May 2020, pp. 1–5. DOI: `10.1109/VTC2020-Spring48590.2020.9129126`. arXiv: `1911.11523`.

[49] A. P. Guevara, S. De Bast, and S. Pollin, "Weave and Conquer: A Measurement-based Analysis of Dense Antenna Deployments", in *ICC 2021 - IEEE International Conference on Communications*, Montreal, QC, Canada: IEEE, Jun. 2021, pp. 1–6. DOI: `10.1109/ICC42927.2021.9500612`.

[50] S. De Bast, *Ultra Dense Indoor MaMIMO CSI Dataset*, Type: dataset, Feb. 2021. DOI: `10.21227/NR6K-8R78`.

[51] G. Callebaut, S. Gunnarsson, A. P. Guevara, F. Tufvesson, S. Pollin, L. Van der Perre, and A. J. Johansson, "Massive MIMO goes Sub-GHz: Implementation and Experimental Exploration for LPWANs", in *2020 54th Asilomar Conference on Signals, Systems, and Computers*, Pacific Grove, CA, USA: IEEE, Nov. 2020, pp. 1101–1105. DOI: `10.1109/IEEECONF51394.2020.9443312`.

[52] E. Björnson, *A Closer Look at Massive MIMO From Ericsson*, Oct. 2021.

[53] H. A. David, *Order statistics*, 2d ed, ser. Wiley series in probability and mathematical statistics. New York: Wiley, 1981.

[54] H.-C. Yang and M.-S. Alouini, *Order Statistics in Wireless Communications: Diversity, Adaptation, and Scheduling in MIMO and OFDM systems*. Cambridge, UK ; New York: Cambridge University Press, Sep. 2011.

[55] C. Shepard, A. Javed, and L. Zhong, "Control Channel Design for Many-Antenna MU-MIMO", in *Proceedings of the 21st Annual International Conference on Mobile Computing and Networking*, ser. MobiCom '15, New York, NY, USA: ACM, 2015, pp. 578–591. DOI: `10.1145/2789168.2790120`.

[56] P. C. F. Eggers, M. Angjelichinoski, and P. Popovski, "Wireless Channel Modeling Perspectives for Ultra-Reliable Communications", *IEEE Transactions on Wireless Communications*, vol. 18, no. 4, pp. 2229–2243, Apr. 2019. DOI: `10.1109/TWC.2019.2901788`. arXiv: `1705.01725`.

[57] A. Edelman and Y. Wang, "Random matrix theory and its innovative applications", in *Advances in Applied Mathematics, Modeling, and Computational Science*, R. Melnik and I. S. Kotsireas, Eds. Boston, MA: Springer US, 2013, pp. 91–116. DOI: `10.1007/978-1-4614-5389-5_5`.

[58] A. Edelman, A. Guionnet, and S. Péché, "Beyond universality in random matrix theory", *The Annals of Applied Probability*, vol. 26, no. 3, Jun. 2016, arXiv: 1405.7590. DOI: `10.1214/15-AAP1129`.

[59] G. Livan, M. Novaes, and P. Vivo, *Introduction to Random Matrices*, ser. SpringerBriefs in Mathematical Physics. Cham: Springer International Publishing, 2018, vol. 26. DOI: `10.1007/978-3-319-70885-0`.

[60] F. Rusek, D. Persson, B. K. Lau, E. G. Larsson, T. L. Marzetta, and F. Tufvesson, "Scaling Up MIMO: Opportunities and Challenges with Very Large Arrays", *IEEE Signal Processing Magazine*, vol. 30, no. 1, pp. 40–60, Jan. 2013. DOI: `10.1109/MSP.2011.2178495`.

[61] P. Harris, S. Malkowsky, J. Vieira, *et al.*, "Performance Characterization of a Real-Time Massive MIMO System With LOS Mobile Channels", *IEEE J. Sel. Areas Commun.*, vol. 35, no. 6, pp. 1244–1253, Jun. 2017. DOI: `10.1109/JSAC.2017.2686678`.

[62] S. Malkowsky, J. Vieira, L. Liu, *et al.*, “The World’s First Real-Time Testbed for Massive MIMO: Design, Implementation, and Validation”, *IEEE Access*, vol. 5, pp. 9073–9088, 2017. DOI: `10.1109/ACCESS.2017.2705561`.

[63] P. Harris, S. Zhang, M. Beach, E. Mellios, A. Nix, S. Armour, A. Doufexi, K. Nieman, and N. Kundargi, “LOS Throughput Measurements in Real-Time with a 128-Antenna Massive MIMO Testbed”, in *2016 IEEE Global Communications Conference (GLOBECOM)*, IEEE, Dec. 2016, pp. 1–7. DOI: `10.1109/GLOCOM.2016.7841965`.

[64] B. M. Hochwald, T. L. Marzetta, and V. Tarokh, “Multiple-antenna channel hardening and its implications for rate feedback and scheduling”, *IEEE Transactions on Information Theory*, vol. 50, no. 9, pp. 1893–1909, Sep. 2004. DOI: `10.1109/TIT.2004.833345`.

[65] S. Gunnarsson, J. Flordelis, L. V. d. Perre, and F. Tufvesson, “Channel Hardening in Massive MIMO-A Measurement Based Analysis”, in *2018 IEEE 19th International Workshop on Signal Processing Advances in Wireless Communications (SPAWC)*, arXiv:1804.01690, Jun. 2018, pp. 1–5. DOI: `10.1109/SPAWC.2018.8445925`.

[66] A. O. Martinez, E. De Carvalho, and J. O. Nielsen, “Massive MIMO properties based on measured channels: Channel hardening, user decorrelation and channel sparsity”, in *2016 50th Asilomar Conference on Signals, Systems and Computers*, IEEE, Nov. 2016, pp. 1804–1808. DOI: `10.1109/ACSSC.2016.7869694`.

[67] H. El-Sallabi, P. Kyritsi, A. Paulraj, and G. Papanicolaou, “Experimental Investigation on Time Reversal Precoding for Space-Time Focusing in Wireless Communications”, *IEEE Trans. Instrum. Meas.*, vol. 59, no. 6, pp. 1537–1543, Jun. 2010. DOI: `10.1109/TIM.2009.2024339`.

[68] S. Payami and F. Tufvesson, “Delay spread properties in a measured massive MIMO system at 2.6 GHz”, in *2013 IEEE 24th Annual International Symposium on Personal, Indoor, and Mobile Radio Communications (PIMRC)*, IEEE, Sep. 2013, pp. 53–57. DOI: `10.1109/PIMRC.2013.6666103`.

[69] J.-C. Guey and L. Larsson, “Modeling and evaluation of MIMO systems exploiting channel reciprocity in TDD mode”, in *IEEE 60th Vehicular Technology Conference (VTC2004-Fall)*, IEEE, Sep. 2004, pp. 4265–4269. DOI: `10.1109/VETECF.2004.1404883`.

[70] *Introduction to the NI MIMO Prototyping System Hardware*, Dec. 2017.

[71] B. Fleury, “An uncertainty relation for WSS processes and its application to WSSUS systems”, *IEEE Trans. Commun.*, vol. 44, no. 12, pp. 1632–1634, Dec. 1996. DOI: `10.1109/26.545890`.

[72] M. P. Fitton, A. R. Nix, and M. A. Beach, "Evaluation of metrics for characterising the dispersion of the mobile channel", in *Vehicular Technology Conference - VTC*, IEEE, 1996, pp. 1418–1422.

[73] I. Reed, "On a moment theorem for complex Gaussian processes", *IRE Transactions on Information Theory*, vol. 8, no. 3, pp. 194–195, Apr. 1962. DOI: `10.1109/TIT.1962.1057719`.

[74] M. Joham, W. Utschick, and J. A. Nossek, "Linear transmit processing in MIMO communications systems", *IEEE Transactions on Signal Processing*, vol. 53, no. 8, pp. 2700–2712, Aug. 2005. DOI: `10.1109/TSP.2005.850331`.

[75] T. Haustein, C. v. Helmolt, E. Jorswieck, V. Jungnickel, and V. Pohl, "Performance of MIMO systems with channel inversion", in *Vehicular Technology Conference. IEEE 55th Vehicular Technology Conference. VTC Spring 2002*, vol. 1, May 2002, 35–39 vol.1. DOI: `10.1109/VTC.2002.1002659`.

[76] A. Papoulis, *Probability, random variables, and stochastic processes*, 3. ed, ser. McGraw-Hill Series in Electrical Engineering Communications and Signal Processing. New York: McGraw-Hill, 1991.

[77] A. M. Mathai, "Storage capacity of a dam with gamma type inputs", *Annals of the Institute of Statistical Mathematics*, vol. 34, no. 1, pp. 591–597, Dec. 1982. DOI: `10.1007/BF02481056`.

[78] E. W. Stacy, "A generalization of the gamma distribution", *The Annals of Mathematical Statistics*, vol. 33, no. 3, pp. 1187–1192, Sep. 1962. DOI: `10.1214/aoms/1177704481`.

[79] E. Björnson, E. d. Carvalho, E. G. Larsson, and P. Popovski, "Random access protocol for massive MIMO: Strongest-user collision resolution (SUCR)", May 2016, pp. 1–6. DOI: `10.1109/ICC.2016.7510793`.

[80] C.-M. Chen, V. Volskiy, A. Chiumento, L. Van der Perre, G. A. E. Vandenbosch, and S. Pollin, "Exploration of User Separation Capabilities by Distributed Large Antenna Arrays", in *2016 IEEE Globecom Workshops*, Dec. 2016, pp. 1–6. DOI: `10.1109/GLOCOMW.2016.7848903`.

[81] F. Ramirez-Mireles, "On the performance of ultra-wide-band signals in Gaussian noise and dense multipath", *IEEE Trans. Veh. Technol.*, vol. 50, no. 1, pp. 244–249, Jan. 2001. DOI: `10.1109/25.917932`.

[82] G. Llano, J. Reig, and L. Rubio, "Analytical Approach to Model the Fade Depth and the Fade Margin in UWB Channels", *IEEE Trans. Veh. Technol.*, vol. 59, no. 9, pp. 4214–4221, Nov. 2010. DOI: `10.1109/TVT.2010.2070815`.

[83] H. Ji, S. Park, J. Yeo, Y. Kim, J. Lee, and B. Shim, "Ultra-Reliable and Low-Latency Communications in 5G Downlink: Physical Layer Aspects", *IEEE Wireless Communications*, vol. 25, no. 3, pp. 124–130, Jun. 2018. DOI: `10.1109/MWC.2018.1700294`.

[84] A. Kosta, N. Pappas, and V. Angelakis, "Age of Information: A New Concept, Metric, and Tool", *Foundations and Trends® in Networking*, vol. 12, no. 3, pp. 162–259, 2017. DOI: `10.1561/1300000060`.

[85] H. Yan, A. Ashikhmin, and H. Yang, *Can Massive MIMO Support URLLC?*, to appear in the 2021 IEEE 93rd Vehicular Technology Conference (VTC2021-Spring), 2021. arXiv: `2102.09156`.

[86] M. Angjelichinoski, K. F. Trillingsgaard, and P. Popovski, "A Statistical Learning Approach to Ultra-Reliable Low Latency Communication", *IEEE Transactions on Communications*, vol. 67, no. 7, pp. 5153–5166, Jul. 2019. DOI: `10.1109/TCOMM.2019.2907241`.

[87] D. Tse and P. Viswanath, *Fundamentals of Wireless Communication*, 1st ed. Cambridge University Press, May 26, 2005. DOI: `10.1017/CBO9780511807213`.

[88] Hon Tat Hui, "The performance of the maximum ratio combining method in correlated rician-fading channels for antenna-diversity signal combining", *IEEE Transactions on Antennas and Propagation*, vol. 53, no. 3, pp. 958–964, Mar. 2005. DOI: `10.1109/TAP.2004.842649`.

[89] A. Dvoretzky, J. Kiefer, and J. Wolfowitz, "Asymptotic Minimax Character of the Sample Distribution Function and of the Classical Multinomial Estimator", *The Annals of Mathematical Statistics*, vol. 27, no. 3, pp. 642–669, Sep. 1956. DOI: `10.1214/aoms/1177728174`.

[90] P. Massart, "The Tight Constant in the Dvoretzky-Kiefer-Wolfowitz Inequality", *The Annals of Probability*, vol. 18, no. 3, pp. 1269–1283, Jul. 1990. DOI: `10.1214/aop/1176990746`.

[91] M. Yacoub, "The κ-μ distribution and the η-μ distribution", *IEEE Antennas and Propagation Magazine*, vol. 49, no. 1, pp. 68–81, Feb. 2007. DOI: `10.1109/MAP.2007.370983`.

[92] D. Ciuonzo, P. Salvo Rossi, and S. Dey, "Massive MIMO Channel-Aware Decision Fusion", *IEEE Transactions on Signal Processing*, vol. 63, no. 3, pp. 604–619, Feb. 2015. DOI: `10.1109/TSP.2014.2376886`.

[93] Ö. Özdogan, E. Björnson, and E. G. Larsson, "Massive MIMO with Spatially Correlated Rician Fading Channels", *IEEE Transactions on Communications*, vol. 67, no. 5, pp. 3234–3250, 2019. DOI: `10.1109/TCOMM.2019.2893221`.

[94] A. A. Polegre, F. Riera-Palou, G. Femenias, and A. G. Armada, "Channel Hardening in Cell-Free and User-Centric Massive MIMO Networks With Spatially Correlated Ricean Fading", *IEEE Access*, vol. 8, pp. 139 827–139 845, 2020. DOI: `10.1109/ACCESS.2020.3012736`.

[95] Z. Wang, J. Zhang, E. Björnson, and B. Ai, "Uplink Performance of Cell-Free Massive MIMO Over Spatially Correlated Rician Fading Channels", *IEEE Communications Letters*, vol. 25, no. 4, pp. 1348–1352, Apr. 2021. DOI: `10.1109/LCOMM.2020.3041899`.

[96] Y. Chen and C. Tellambura, "Distribution Functions of Selection Combiner Output in Equally Correlated Rayleigh, Rician, and Nakagami-m Fading Channels", *IEEE Transactions on Communications*, vol. 52, no. 11, pp. 1948–1956, Nov. 2004. DOI: `10.1109/TCOMM.2004.836596`.

[97] M. Chiani, M. Win, and A. Zanella, "On the Capacity of Spatially Correlated MIMO Rayleigh-Fading Channels", *IEEE Transactions on Information Theory*, vol. 49, no. 10, pp. 2363–2371, Oct. 2003. DOI: `10.1109/TIT.2003.817437`.

[98] R. Nabar, H. Bolcskei, and A. Paulraj, "Diversity and Outage Performance in Space-Time Block Coded Ricean MIMO Channels", *IEEE Transactions on Wireless Communications*, vol. 4, no. 5, pp. 2519–2532, Sep. 2005. DOI: `10.1109/TWC.2005.853835`.

[99] K. Hamdi, "Capacity of MRC on Correlated Rician Fading Channels", *IEEE Transactions on Communications*, vol. 56, no. 5, pp. 708–711, May 2008. DOI: `10.1109/TCOMM.2008.060381`.

[100] L. Sanguinetti, A. Kammoun, and M. Debbah, "Theoretical Performance Limits of Massive MIMO With Uncorrelated Rician Fading Channels", *IEEE Transactions on Communications*, vol. 67, no. 3, pp. 1939–1955, Mar. 2019. DOI: `10.1109/TCOMM.2018.2884003`.

[101] M. Matthaiou, H. Q. Ngo, P. J. Smith, H. Tataria, and S. Jin, "Massive MIMO with a Generalized Channel Model: Fundamental Aspects", in *2019 IEEE 20th International Workshop on Signal Processing Advances in Wireless Communications (SPAWC)*, Cannes, France: IEEE, Jul. 2019, pp. 1–5. DOI: `10.1109/SPAWC.2019.8815518`.

[102] S. Loyka and J. Mosig, "Channel Capacity of n-Antenna BLAST Architecture", *Electronics Letters*, vol. 36, no. 7, p. 660, 2000. DOI: `10.1049/el:20000499`.

[103] S. Loyka, "Channel Capacity of MIMO Architecture Using the Exponential Correlation Matrix", *IEEE Communications Letters*, vol. 5, no. 9, pp. 369–371, Sep. 2001. DOI: `10.1109/4234.951380`.

[104] W. A. Al-Hussaibi, "A Generalised Antenna Correlation Model for Accurate Performance Evaluation of 2D Massive MIMO Communication Systems", *Australian Journal of Electrical and Electronics Engineering*, vol. 17, no. 4, pp. 269–277, 2020. DOI: `10.1080/1448837X.2020.1844367`.

[105] P. Ramírez-Espinosa, D. Morales-Jimenez, J. A. Cortes, J. F. Paris, and E. Martos-Naya, "New Approximation to Distribution of Positive RVs Applied to Gaussian Quadratic Forms", *IEEE Signal Processing Letters*, vol. 26, no. 6, pp. 923–927, Jun. 2019. DOI: `10.1109/LSP.2019.2912295`.

[106] P. Ramírez-Espinosa, L. Moreno-Pozas, J. F. Paris, J. A. Cortes, and E. Martos-Naya, “A New Approach to the Statistical Analysis of Non-Central Complex Gaussian Quadratic Forms With Applications”, *IEEE Transactions on Vehicular Technology*, vol. 68, no. 7, pp. 6734–6746, Jul. 2019. DOI: `10.1109/TVT.2019.2916725`.

[107] C. A. Balanis, *Antenna Theory: Analysis and Design*, Fourth edition. Hoboken, NJ: Wiley, 2016.